2010

Integral equation analysis of electromagnetic wave propagation in periodic structure and error analysis of various basis functions in projection of plane waves

Fu-gang Hu
Iowa State University

Recommended Citation

Hu, Fu-gang, "Integral equation analysis of electromagnetic wave propagation in periodic structure and error analysis of various basis functions in projection of plane waves" (2010). *Graduate Theses and Dissertations*. 11425.
https://lib.dr.iastate.edu/etd/11425

Integral equation analysis of electromagnetic wave propagation in periodic structure and error analysis of various basis functions in projection of plane waves

by

Fu-Gang Hu

A dissertation submitted to the graduate faculty

in partial fulfillment of the requirements for the degree of

DOCTOR OF PHILOSOPHY

Major: Electrical Engineering

Program of Study Committee:
Jiming Song, Major Professor
John R. Bowler
Jaeyoun Kim
Mani Mina
Jue Yan

Iowa State University

Ames, Iowa

2010

TABLE OF CONTENTS

LIST OF TABLES

LIST OF FIGURES

ACKNOWLEDGEMENTS

I would like to take this opportunity to express my thanks to those who helped me with various aspects of conducting research and the writing of this thesis.

First, I would like to thank Dr. Jiming Song to give me an opportunity of pursuing Ph. D. degree at Iowa State University. As my advisor, he provided me with his guidance, helps, patience, and financial support throughout my research work.

Secondly, I would also like to thank my committee members for their time and committee service: Dr. John R. Bowler, Dr. Jaeyoun Kim, Dr. Mani Mina, and Dr. Jue Yan.

Finally, I would like to thank my family and friends for their concerns, supports, and helps.

ABSTRACT

In the first part of this dissertation, the integral equation approaches are developed to analyze the wave propagation in periodic structures. Firstly, an integral equation approach is developed to analyze the two-dimensional (2-D) scattering from multilayered periodic array. The proposed approach is capable of handling scattering from the array filled with different media in different layers. Combining the equivalence principle algorithm and connection scheme (EPACS), it can be avoided to find and evaluate the multilayered periodic Green's functions. For 2^N identical layers, the elimination of the unknowns between top and bottom surfaces can be accelerated using the logarithm algorithm. More importantly, based on EPACS, an approach is proposed to effectively handle the semi-infinitely layered case in which a unit consisting of several layers is repeated infinitely in one direction.

Secondly, the integral-equation (IE) method formulated in the spatial domain is employed to calculate the scattering from the doubly periodic array of three-dimensional (3-D) perfect electric conductor (PEC) objects. The special testing and basis functions are proposed to handle the problem with non-zero normal components of currents at the boundary of one period. Moreover, a relationship between the scattering from the PEC screen and its complementary structure is established. In order to efficiently compute the matrix elements from the IE approach, an acceleration technique with the exponential convergence rate is applied to evaluate the doubly periodic Green's function. The formulations in this technique are appropriately modified so that the new form facilitates numerical calculation for the general cases.

In the second part of this dissertation, the error analysis of various basis functions in projection of the plane wave was conducted, including pulse basis, triangular basis, the basis of their higher-order version, and the divergence-conforming basis on rectangular and triangular elements. The projection error is given analytical, asymptotically, and numerically. The application of the p-th order one-dimensional

(1D) basis can result in the projection error which is asymptotically proportional to $(p+1)$-th power of the density of unknowns. Based on the analytical projection errors in 1D case, it is found when the expansion basis is fixed, the application of different testing functions only affect the constant coefficient of the projection error rather than the order. Generally, the error of divergence-conforming basis in projection of curl-free vectors is less than that of divergence-free vectors.

CHAPTER 1 INTRODUCTION

The thesis is comprised of two parts of research work. Part I is on the electromagnetic modelling of the periodic structures. The integral equation approaches are developed to analyze the periodic structures. Part II is about the error analysis of various basis functions in projection of plane waves. The last chapter gives a conclusion to this thesis.

1.1 Introduction to Part I

1.1.1 Review on application of periodic structures

In the last several decades, periodic structures have gained intensive interests and attention of the researchers in the field of electromagnetics. They can find a variety of applications in the area of electromagnetics. First, the periodic structures was applied to inhabit the spontaneous emission in semiconductor laser [1]. Researchers found that the photonic crystal structures can have a full photonic bandgap, where the electromagnetic (EM) wave is forbidden to propagate in every direction [2]. Secondly, the periodic structure can be applied to create the artificial material [3]. Recently, researchers designed the metamaterial with negative permittivity and permeability [4]-[7]. The engineered metamaterial can provide the EM properties that is difficult to be found in the conventional and natural material. Thirdly, the periodic structure can apply to the design of waveguide filter [3].

Fourthly, the periodic structure has many application in the microwave engineering. For example, the frequency selective surface (FSS) [8], [9], which has the frequency filtering property, is a doubly periodic array of patches and apertures. FSS can be applied as antenna radomes for control of EM wave transmission and reflection. The FSS reflector can be employed to separate feeds of different frequency bands in reflector antenna systems. The other example is the electromagnetic bandgap (EBG) structures [10]-[13], which are periodic structures made by metallic, dielectric or metallodielectric elements. The

EBG structures has important application in the design of improved antennas: 1) they serve as artificial magnetic conductor ground planes to design low profile antennas; 2) they are used as substrates for microstrip patch antennas to suppress the surface wave; 3) they are used as superstrates over radiation sources to increase the radiation aperture of the original structure, and thus the directivity.

1.1.2 Review on theory about periodic structures

The EM problems about the periodic structures can be categorized into three types: eigenvalue, source driven and homogenization problems. For the eigenvalue problem, the objective is to find the the resonant frequencies for a given wave vector or wave vectors for a given resonant frequency. The resultant band structure, describing the relationship between the resonant frequencies and the wave vectors, forms the $k - \beta$ diagram ($\beta = \omega/c$). The EM fields are not excited by sources, but subject to the boundary conditions. In general, the eigenvalue problem is in regard to the one-dimensional (1-D) singly periodic, two-dimensional (2-D) doubly periodic and three-dimensional (3-D) triply periodic structures. *Singly*, *doubly*, and *triply periodic* indicate the structures are periodic in one, two, and three directions, respectively. *1-D*, *2-D*, and *3-D* indicate the EM quantities varies with one, two, and three independent spatial variables, respectively. The source driven problem is the scattering problem of periodic structures, which is usually to calculate the reflection and transmission coefficients of Flquet's modes which is excited by the incident EM wave. For this problem, the number of directions, along which the structure is periodic, is less than that of the dimensions of the problem. The homogenization of periodic structures is to find the effective permittivity and permeability of the composite material.

Several methods have been successfully developed to solve the eigenvalue problem, including the plane wave method [14], [15], order-N method [16], transfer matrix method (TMM) [17], [18], hybrid methods [19], [20], finite-difference method [21], etc. The plane wave method expands the EM quantities into plane waves. The wave equation reduces to a matrix eigensystem. The eigenvalues represent the resonant frequencies and the eigenvectors represent the Floquet's modes. The order-N method is essentially the finite-difference method in time domain. The computing time scales linearly with the size of the system. The TMM method is based on Maxwell equations on a lattice. The relationship between the fields on two planes can be described by the transfer matrices. At fixed frequency, if the fields on one side of a sample is given, we can transfer the fields throughout the whole sample. Unlike the plane wave method, the TMM method is applicable to the case of frequency-dispersion media. This is because that the TMM method seeks the wave vectors for a given resonant frequency, while the plane wave method finds the resonant frequencies for a given wave vector.

The electromagnetic scattering from periodic structures has been investigated by many methods, including the mode-matching method [22]-[24], finite element method (FEM) [25]-[26], boundary integral-modal (BI-modal) method [27], finite element-boundary integral (FE-BI) method [28]-[29], integral-equation (IE) method [9], [30]-[34], T-matrix method [35]-[36], etc.

The mode-matching method is suitable to the canonical geometry, such as rectangular or circular PEC patches or apertures perforated from PEC screens. The FEM, which is a full-wave approach, can deal with the arbitrary shape and inhomogeneous media. The FE-BI method takes advantage of BI on the top and/or bottom surfaces of one unit cell, instead of absorbing boundary condition (ABC) used in the FEM. The application of BI is more accurate than that of ABC at the cost of the partially full coefficient matrix.

The IE approaches for periodic structures can be formulated in spectral and spatial domains. The former [9], [30]-[31] is limited to planar periodic metallic structures. In addition, the expansion of electromagnetic (EM) quantities into Floquet's modes has slow convergence rate. The latter can treat the doubly periodic objects with arbitrary shape [32]-[34]. However, it calls for the efficient calculation of the periodic Green's function (PGF). Fortunately, some acceleration techniques have been proposed to achieve the fast convergence for the PGF [37]-[40].

Every material consists of a collection of objects. When the objects' sizes and spacing are much less than the wavelength, the material can be described by the effective permittivity and permeability which present the homogenous view of EM properties of the material [5], [7]. For the homogenization problem, some researchers retrieved the effective parameters by the calculation of the band structure [41]. This approach is not available in the frequency band gaps or when the materials are lossy. Another approach extracts the effective parameters from measured or simulated scattering parameters [42]. However, this approach may be unstable and inaccurate in some cases. Recently, a rigorous integral-equation approach was proposed to homogenize the arbitrary periodic dielectric and/or metallic metamaterials [43]. This approach takes account into both spatial and frequency dispersions and is available in the frequency band gaps.

1.1.3 Research work on periodic structure

In Chapter 2, several approaches for modeling of the wave propagation in 2-D structures are implemented. First, the IE approach for scattering from the singly periodic array of 2-D PEC conducting objects is described. Secondly, the hybrid IE-plane wave approach [19] is implemented to calculate the band structure of the metallic crystals. The in-house code will provide with some numerical results to validate the proposed approaches in Chapters 3 and 4.

In Chapter 3, an IE approach is developed to investigate the frequency response of a 2-D singly periodic array. By the application of the equivalence principle algorithm and connection scheme (EPACS), the case of the periodic array filled with different media in different layers can be treated [44]. The computational domain first is restricted to one period of the multilayered array. In one period, each layer can be treated as an individual cell. Then, the equivalence principle can be applied separately to each individual cell to obtain the integral equations for equivalent currents on the outside boundary of the cell and the perfect electric conductor (PEC) surface. In general, when the cells are not overlapping or connected with each other, it is necessary to build up the relationship between them by applying IE to their outside boundary [45], [46]. However, for the multilayered periodic structure, two neighboring cells are connected via the same interface. Thus, by combining the periodic boundary condition (PBC) with the connection scheme, the relationship can be established between the currents or fields on the topmost and bottommost surfaces. Finally, two integral equations on the topmost and bottommost surfaces, which involve the periodic Green's function, are required to establish the complete equation system. After seeking the solution of equivalent currents on the topmost and bottommost surfaces, the proper way is proposed to correctly calculate the current on the surface of PEC object.

Moreover, based on EPACS, an effective approach is proposed to handle the semi-infinitely layered case in which one unit consisting of several layers is repeated infinitely along one direction. Each unit can be regarded as a two-port network. For this semi-infinitely layered array, the impedance matrix representing the relationship between the equivalent magnetic and electric currents on the top surface of each unit should be identical because the network is infinitely extended when one looks into it from the top surface of any unit. Based on this fact, the equation for this impedance matrix can be established by EPACS and solved using a proper iterative method. After obtaining the impedance matrix, the integral equation on the topmost surface is required to construct the complete system of equations for solving the fields or currents on the top surfaces. Then the reflection coefficients of Floquet's harmonics can be found. It should be mentioned that the direct IE approach definitely cannot handle the case of semi-infinitely layered array since the number of unknowns for the direct IE approach will be infinite. Finally, numerical results are given to verify the proposed approaches.

In Chapter 4, the electric field integral equation (EFIE) formulation in the spatial domain is employed to calculate scattering from doubly periodic array of PEC objects. The following three issues about the IE approach are addressed.

Firstly, the special testing and basis functions are proposed to handle the problem with non-zero normal components of currents at the boundary of one period. As we know, the computational domain for periodic structures is restricted to one period. The objects with periodicity may be truncated by the four-side periodic boundaries (PB). In this case, the electric current flowing out the boundary of PEC surface may not be zero. If one adopts the Rao-Wilton-Glission (RWG) basis functions [47] to expand the current, and treat the boundary in the manner which is applied to single PEC plate, namely, does not assign unknowns on the boundary, the solution to the current will be probably inaccurate or even wrong. This is because this procedure enforces the condition of zero outgoing current on the truncated boundary of PEC. In our work, the special test and basis functions on the truncated boundary are proposed to handle this problem.

Secondly, the relationship is addressed between the scattering from the PEC screen with periodicity and its complementary structure. The Babinet's principle for this dual problem has been proved in several different ways [48]-[50]. This paper shows a simple way for proof of the Babinet's principle for periodic structures. In the proof, the IE formulation and periodic Green's function are involved. In addition, the relationship for the reflection and transmission coefficients between the PEC screen with periodicity and its complementary structure will be given. For periodic apertures perforated from the screen, one can apply integral equations about the electric current on PEC part of the screen. However, the unknown density near the aperture should be made large enough to achieve the accurate solution for the scattering. In contrast, it will be easier to achieve the convergence of solution if one solves the integral equation for the electric current on PEC patches in its dual problem. Then one may find the solution for scattering from the apertures using the relationship mentioned.

Finally, the acceleration technique in [40] is applied to evaluate the PGF. It is with exponential convergence rate and can be easily implemented. One can take advantage of the intrinsic function in Fortran to evaluate the error function involved in [40] since its argument can be real number. The formulations in this technique are appropriately modified so that the new form facilitates numerical calculation for the general cases. Therefore, there will exist no obstacles to effectively evaluate the matrix element of the IE approach.

1.2 Introduction to Part II

It is well-known that the method of moments (MoM) [48] is one of the most important methods in CEM because of its powerful ability in solving the integration equation of electromagnetic radiation and scattering [52]. Like the numerical dispersion error analysis in finite element method (FEM) [53]-[54] and finite difference in time domain (FDTD) [55], the MoM error analysis is an important topic in CEM [56]-[61]. The error analysis of the MoM was performed with the error measure of current, boundary condition, and scattering amplitude.

As mentioned by the researchers [56], the application of expansion and testing functions are one of the most important factors contributing to MoM error. In fact, the various basis functions play important roles in MoM. The application of the proper basis functions can facilitate the accurate and convenient modeling of the complex electromagnetic problems [47], [62]-[64]. It is interesting to investigate the error in projection of the equivalent current of plane wave using various basis functions [65]-[66]. The projection error can serve as the reference for the MoM error analysis [56]. The study of the projection error of the basis functions can indirectly demonstrate how the basis functions affect the accuracy of MoM.

In Chapter 5, the projection error of various basis functions is investigated in details. The equivalent current is expanded by various basis functions. Then application of the weighted residual method will yield the unknown coefficients of basis functions. After obtaining the coefficients, the projection error can be found. The root mean square (RMS) error of current is used as the error measure since the current is integrable. The numerical projection error of the triangular basis, the basis of their higher-order version, and the divergence-conforming basis on rectangular and triangular elements are shown. Furthermore, the closed forms of the projection error on the infinite meshes are derived. The basis functions involved are pulse basis, triangular basis, the second-order basis in 1D case, the divergence-conforming basis on rectangular element and the one-directional triangular element in 2D case. It is found that the projection error of p-th order 1D basis is asymptotically inversely proportional to $(p+1)$-th power of the density of unknowns. Based on the closed-form projection errors in 1D case, it is found when the expansion basis is fixed, the application of different testing functions only affect the coefficient of the projection error rather than the order. In addition, the error of divergence-conforming basis in projection of curl-free vectors is generally less than that of divergence-free vectors. This is expected since both the divergence-conforming basis and the expanded vector are with the same property, namely, curl-free.

CHAPTER 2 ANALYSIS OF WAVE PROPAGATION IN 2-D PERIODIC ARRAY OF CONDUCTING OBJECTS IN FREE SPACE

The scattering and eignvalue problems for the periodic array of 2-D conducting objects have been investigated by some researchers [19], [35]-[36], [67]-[68]. In this chapter, several approaches for modeling of TMz wave propagation in 2-D structures are described. The implementation of the approaches facilitates the provision of some numerical results to validate the proposed approaches in Chapters 3 and 4.

2.1 EM scattering from 2-D singly periodic array of PEC objects

2.1.1 Formulation

We assume the periodic PEC objects are infinitely long along z-axis. Figure 2.1 shows the infinite periodic PEC cylinder array, whose period is P_L along x-direction. The primitive lattice vector is $\mathbf{a}_1 = \hat{x}P_L$. This array is located in free space. It is filled with the same media as the free space. One unit can include multiple PEC objects, whose cross sections can be different. The incident plane wave $\mathbf{E}^{inc} = \mathbf{E_0}e^{-j\mathbf{k}\cdot\boldsymbol{\rho}}$ impinges on the array from free space. Its wave vector is given by $\mathbf{k} = \hat{x}k_x + \hat{y}k_y$, where $k_x = -\beta_0 \cos\phi_i$, $k_y = -\beta_0 \sin\phi_i$, $\beta_0 = \omega\sqrt{\mu_0\epsilon_0}$, and ϕ_i are the incident angles. The case of E-wave (TMz) is considered in this chapter.

According to the Floquet's theorem, the current J_z satisfies

$$J_z(x + mP_L, y) = J_z(x, y)e^{-jmk_xP_L}. \tag{2.1}$$

$J_z(x, y)$ can be written as

$$J_z(x, y) = w(x, y)e^{-jk_xx} \tag{2.2}$$

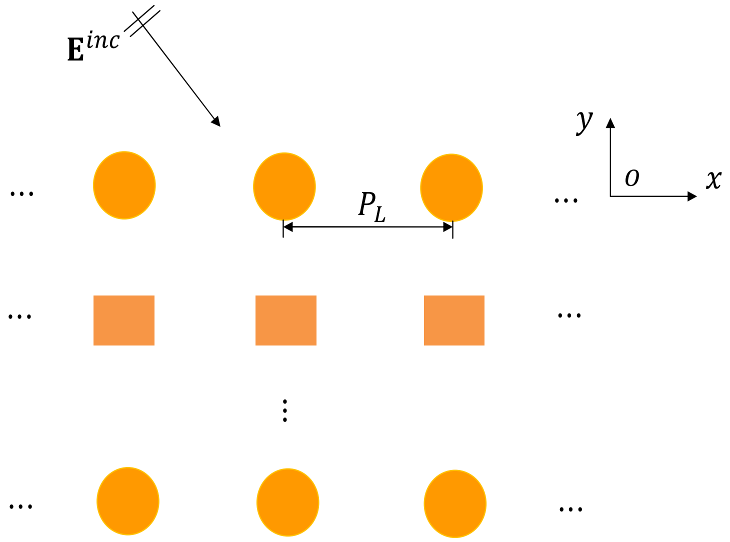

Figure 2.1 Periodic PEC array with a period of P_L along x-direction.

where $w(x, y)$ is a periodic function of x and k_x is the x-component of wave vector $\mathbf{k} = \hat{x}k_x + \hat{y}k_y$. The Bloch condition points out $J_z(x + P_L, y) = J_z(x, y)e^{-jk_xP_L}$.

In view of the structure's periodicity, the computational domain is restricted to one period of the array. The electric field integral equation (EFIE) is given by [67]-[68]

$$j\beta\eta \int_l J_z(\boldsymbol{\rho}')G_p dl' = E_0\, e^{-j\mathbf{k}\cdot\boldsymbol{\rho}} \tag{2.3}$$

where

$$G_p = \frac{1}{4j} \sum_{m=-\infty}^{\infty} \mathrm{H}_0^{(2)} \left(\beta\sqrt{(x - x' - mP_L)^2 + (y - y')^2}\right) e^{-jmk_xP_L} \tag{2.4}$$

β is the wave number and $\mathrm{H}_0^{(2)}$ is the zeroth order Hankel function of the second kind. It is easy to see that when $\boldsymbol{\rho} - \boldsymbol{\rho}' = \hat{x}mP_L$, there exists the singularity in this spatial-domain form. When $(k_x \pm \beta)P_L = 2n\pi$, one can apply the asymptotic form of Hankel function for the large argument to find G_p is still singular. Here m and n are integers. In addition to the form in the spatial domain, G_p can be represented in the spectral form [68]

$$G_p = \frac{1}{2P_L} \sum_{m=-\infty}^{\infty} \frac{1}{\gamma_m} e^{-\gamma_m|y-y'|-jk_{xm}(x-x')} \tag{2.5}$$

where

$$k_{xm} = k_x + \frac{2m\pi}{P_L},\ \gamma_m = \sqrt{k_{xm}^2 - \beta^2} \tag{2.6}$$

From the spectral form, one can also note that when $\boldsymbol{\rho} - \boldsymbol{\rho}' = \hat{x} n P_L$ or $(k_x \pm \beta) P_L = 2m\pi$, there exists the singularity. The space-domain form of G_p has very slow convergence. The spectral-domain form of G_p has exponential convergence rate. Let $u_y = y - y'$. When $|u_y|$ is large, it converges fast. However, when $|u_y|$ is small, its convergence is still very slow. For this case, Veysoglu's transformation can be applied to speed up the convergence of G_p [68]. Using Veysoglu's transformation gives

$$G_p(x, y; x', y') = \sum_{\pm} G_{p\pm} + \frac{1}{4j} \mathrm{H}_0^{(2)}(\beta \sqrt{(x - x')^2 + (y - y')^2}) \tag{2.7}$$

where

$$\begin{aligned}
G_{p\pm}(x, y; x', y') &= \frac{1}{\pi} e^{-j(\pm k_x + \beta) P_L \pm j\beta(x - x')} \int_0^\infty f(\pm k_x, \pm(x - x'), y - y', u) du \\
f(k_x, t_1, t_2, u) &= \frac{f_n(t_1, t_2, u)}{f_d(k_x, t_1, u)} \\
f_n(t_1, t_2, u) &= e^{-u^2} \cos\left(t_2 u \sqrt{u^2 + 2j\beta(P_L - t_1)} / (P_L - t_1)\right) \\
f_d(k_x, t_1, u) &= \left[1 - e^{-u^2/(1 - t_1/P_L) - j(k_x + \beta) P_L}\right] \sqrt{u^2 + 2j\beta(P_L - t_1)}
\end{aligned}$$

The PEC boundary is discretized into linear elements. Using the pulse basis as the expansion function and the point function as the testing function, one may obtain a set of equations about the coefficients of the basis functions.

$$\mathbf{Z}\mathbf{x} = \mathbf{b} \tag{2.8}$$

where

$$\begin{aligned}
Z_{mn} &= j\beta\eta \int_{l_n} G_p(x_m, y_m; x', y') dl' \\
b_m &= E_0 \, e^{-j\mathbf{k} \cdot \boldsymbol{\rho}_m}
\end{aligned} \tag{2.9}$$

$\boldsymbol{\rho}_m$ indicates the coordinate of the central point of the mth linear element. The integral in Z_{mn} can be approximated by

$$\int_{l_n} G_p(x_m, y_m; x', y') dl' = \begin{cases} \frac{1}{4j} \left\{1 - j\frac{2}{\pi}[\ln \frac{\gamma\beta l_n}{4} - 1]\right\} l_n & \\ + \sum_{\pm} G_{p\pm}(x_m, y_m; x_n, y_n) l_n, & m = n \\ & \\ G_p(x_m, y_m; x_n, y_n) l_n, & m \neq n \end{cases} \tag{2.10}$$

where $\gamma \approx 1.781072$.

The scattered field E_z^s can be expressed as a superposition of the Floquet's harmonics

$$E_z^s = \sum_{m=-\infty}^{\infty} e_m e^{-jk_{xm}x} e^{-\gamma_m y} \tag{2.11}$$

The Floquet's harmonics are orthogonal with each other over one period in x. Assume the reference plane is located at $y = y_0$. Thus,

$$\int_{x=0}^{P_L} E_z^s(x, y_0) e^{jk_{xm}x} dx = e_m P_L e^{-\gamma_m y_0} \tag{2.12}$$

On the other hand, we can calculate the E_z^s after obtaining the current on the PEC

$$E_z^s = -j\beta\eta \int_l J_z(\boldsymbol{\rho}') G_p dl' \tag{2.13}$$

From (2.12) and (2.13), one obtains

$$e_m = \frac{-j\beta\eta e^{\gamma_m y_0}}{P_L} \int_{x=0}^{P_L} \int_l J_z(\boldsymbol{\rho}') G_p|_{y=y_0} dl' e^{jk_{xm}x} dx \tag{2.14}$$

The reflection coefficient of the $0\mathrm{th}$ harmonic is obtained by

$$R_0 = \frac{e_0}{E_0} e^{-j2\sqrt{\beta^2 - k_x^2} y_0} \tag{2.15}$$

2.1.2 Numerical results

To validate the implementation of the IE approach, several periodic structures are simulated. The numerical results are compared with exact solution and those from the other approaches.

In the first example, the infinite PEC plate is simulated. The period of one cell is set to be $P_L = 0.3$ m. The PEC plate is located at $y = 0$. The computational domain is confined to a straight line with length $L = 0.3$ m along the x direction. The plane wave is obliquely incident on the PEC plate. $\theta_i = 90^\mathrm{o}$ and $\phi_i = 30^\mathrm{o}$. The electric field is along the z direction. The straight line is discretized into 41 linear elements. Figure 2.2 shows the current distribution on the PEC plate at $f = 0.3$ GHz. The current is normalized by E_0. Figure 2.3 shows the reflection coefficients R_0 as a function of the electric size of one period P_L. From these two figures, good agreements can be observed between the numerical results and exact solution.

The second example is to simulate the PEC gratings. The period of one cell is set to be $P_L = 0.3$ m. The straight line is with length $L = 0.15$ m along the x direction. The plane wave is normally

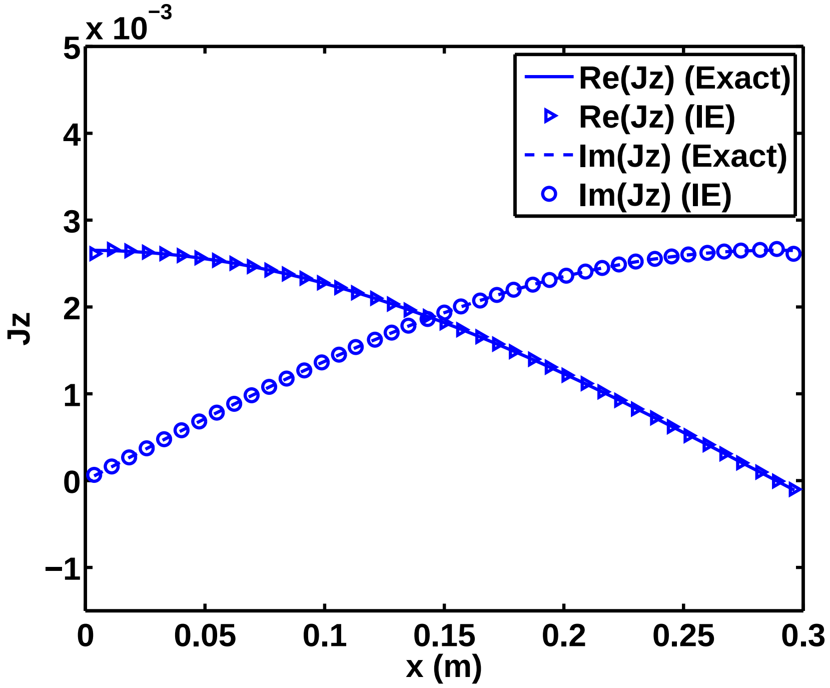

Figure 2.2 Current distribution on the infinite PEC plate at $f = 0.3$ GHz. $L = P_L = 0.3$ m. $\theta_i = 90^o$ and $\phi_i = 30^o$.

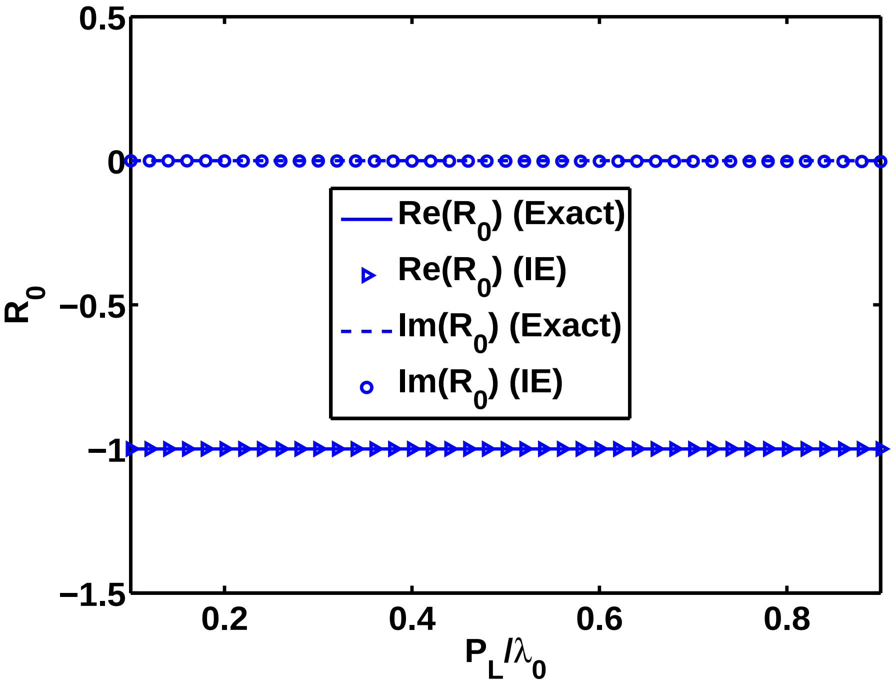

Figure 2.3 Reflection coefficient R_0 of the infinite PEC plate. $L = P_L = 0.3$ m. $\theta_i = 90^o$ and $\phi_i = 30^o$.

incident on the PEC plate, i.e., $\theta_i = 90^{\circ}$ and $\phi_i = 90^{\circ}$. Figure 2.4 shows the reflection coefficient of the gratings.

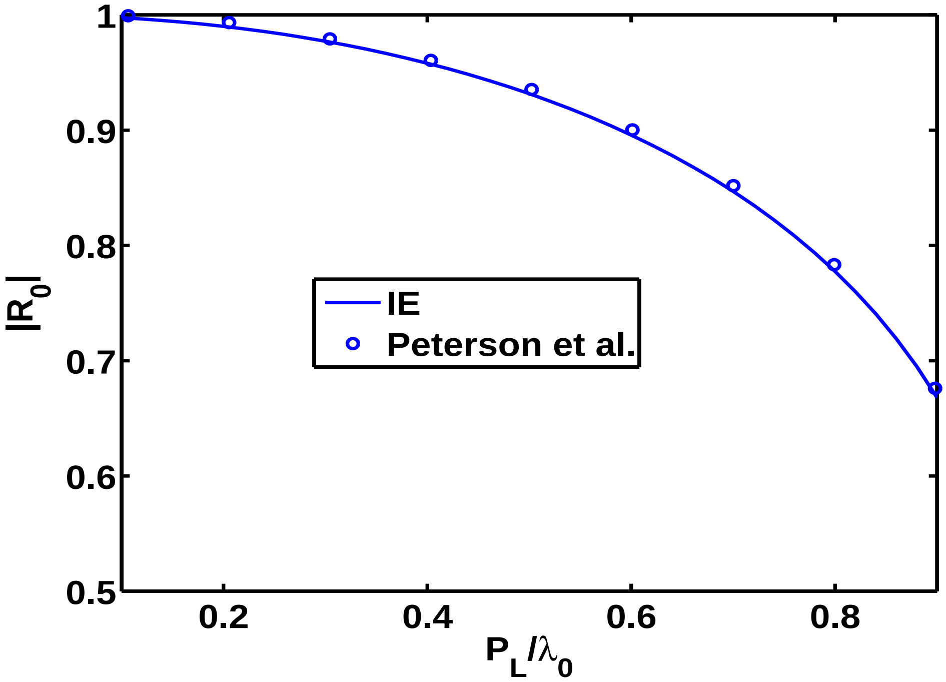

Figure 2.4 Reflection coefficient R_0 of the gratings. $L = 0.15$ m and $P_L = 0.3$ m. $\theta_i = 90^{\circ}$ and $\phi_i = 90^{\circ}$. The circle indicates the results taken from [67].

The third example is to simulate the periodic array of PEC circular cylinders. The radius of the circle is $R = 0.06$ m and $P_L = 0.4$ m. The plane wave is normally incident on the cylinders. Figure 2.5 shows the reflection coefficient of the periodic array of PEC circular cylinders.

2.2 Eigenvalue problem of doubly-periodic PEC structure

2.2.1 Formulation

Assume $\mathbf{a}_1$ and $\mathbf{a}_2$ are the primitive lattice vectors for the doubly-periodic structure. The reciprocal primitive lattice vectors $\mathbf{b}_1$ and $\mathbf{b}_2$ can be obtained by

$$\begin{aligned} \mathbf{b}_1 &= \frac{2\pi}{\Omega}\mathbf{a}_2 \times \hat{z} \\ \mathbf{b}_2 &= \frac{2\pi}{\Omega}\hat{z} \times \mathbf{a}_1 \end{aligned} \tag{2.16}$$

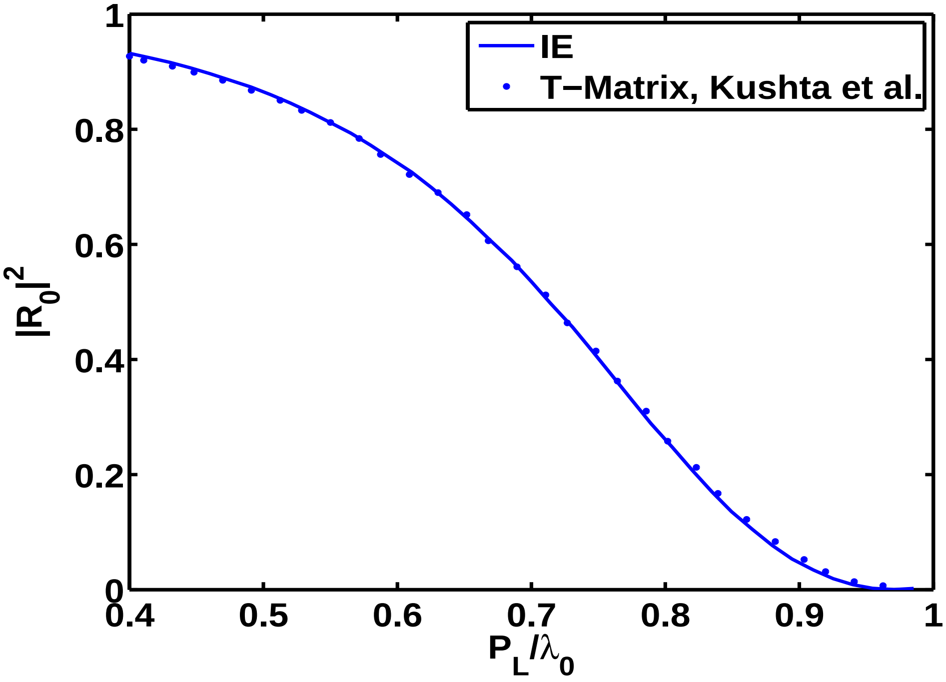

Figure 2.5 Reflection coefficient R_0 of the array of PEC circular cylinders. $R = 0.06$ m and $P_L = 0.4$ m. $\theta_i = 90^o$ and $\phi_i = 90^o$. The dot indicates the results taken from [35].

where $\Omega = |\mathbf{a}_1 \times \mathbf{a}_2|$.

The relations between primitive and reciprocal lattice vectors are

$$\mathbf{a}_m \cdot \mathbf{b}_n = 2\pi\delta_{mn} \tag{2.17}$$

where δ_{mn} is the Kronecker delta function.

The pseudo-periodic Green's function Φ_p for the doubly-periodic structure satisfies

$$\nabla^2\Phi_p + \beta^2\Phi_p = -\sum_{\mathbf{I}} \delta(\mathbf{u} - \boldsymbol{\rho}_{\mathbf{I}})e^{-j\mathbf{k}\cdot\boldsymbol{\rho}_{\mathbf{I}}} \tag{2.18}$$

where $\mathbf{u} = \boldsymbol{\rho} - \boldsymbol{\rho}'$, $\boldsymbol{\rho}_{\mathbf{I}} = I_1\mathbf{a}1 + I_2\mathbf{a}_2$, and $\mathbf{I} = (I_1, I_2)$.

The Poisson's summation formula is

$$\sum_{\mathbf{I}} f(\mathbf{u} - \boldsymbol{\rho}_{\mathbf{I}})e^{-j\mathbf{k}\cdot\boldsymbol{\rho}_{\mathbf{I}}} = \sum_{\mathbf{J}} \frac{1}{\Omega} F(\mathbf{k} + \boldsymbol{\kappa}_{\mathbf{J}})e^{-j(\mathbf{k}+\boldsymbol{\kappa}_{\mathbf{J}})\cdot\mathbf{u}} \tag{2.19}$$

where $\boldsymbol{\kappa}_{\mathbf{J}} = J_1\mathbf{b}_1 + J_2\mathbf{b}_2$, $\mathbf{J} = (J_1, J_2)$, and $F(\mathbf{k})$ is the 2-D Fourier transform of $f(\boldsymbol{\rho})$. Applying the

Poisson's summation formula, the right-hand side of (2.18) can be transformed into

$$-\sum_{\mathbf{I}} \delta(\mathbf{u}-\boldsymbol{\rho}_{\mathbf{I}}) e^{-j\mathbf{k}\cdot\boldsymbol{\rho}_{\mathbf{I}}} = -\sum_{\mathbf{J}} \frac{1}{\Omega} e^{-j(\mathbf{k}+\boldsymbol{\kappa}_{\mathbf{J}})\cdot\mathbf{u}} \tag{2.20}$$

In terms of the Floquet's theorem, the pseudo-periodic Green's function can be expanded into the Floquet's modes

$$\Phi_p(\mathbf{u}) = \sum_{\mathbf{J}} C_{\mathbf{J}} e^{-j(\mathbf{k}+\boldsymbol{\kappa}_{\mathbf{J}})\cdot\mathbf{u}} \tag{2.21}$$

Substitution of (2.21) and (2.20) into (2.18) yields

$$C_{\mathbf{J}} = \frac{1}{\Omega(|\mathbf{k}+\boldsymbol{\kappa}_{\mathbf{J}}|^2-\beta^2)} \tag{2.22}$$

Thus, $\Phi_p(\mathbf{u})$ is represented by

$$\Phi_p(\mathbf{u}) = \frac{1}{\Omega} \sum_{\mathbf{J}} \frac{e^{-j(\mathbf{k}+\boldsymbol{\kappa}_{\mathbf{J}})\cdot\mathbf{u}}}{|\mathbf{k}+\boldsymbol{\kappa}_{\mathbf{J}}|^2-\beta^2} \tag{2.23}$$

In addition to (2.23), Φ_p has the other two forms, namely, the form in the spatial domain

$$\Phi_p(\mathbf{u}) = \frac{1}{4j} \sum_{\mathbf{I}} \mathrm{H}_0^{(2)}(\beta|\mathbf{u}-\boldsymbol{\rho}_{\mathbf{I}}|) e^{-j\mathbf{k}\cdot\boldsymbol{\rho}_{\mathbf{I}}} \tag{2.24}$$

and the form in the spectral domain [19]

$$\Phi_p(\mathbf{u}) = \Phi_H + \Gamma_\Phi \tag{2.25}$$

where

$$\begin{aligned} \Phi_H &= \frac{1}{2|\mathbf{a}_1|} \sum_n \frac{e^{-j\mathbf{k}_{n,\|}\cdot\mathbf{u}}}{\gamma_n} \cdot e^{-\gamma_n|u_\perp|} \\ \Gamma_\Phi &= \frac{1}{2|\mathbf{a}_1|} \sum_n \frac{e^{-j\mathbf{k}_{n,\|}\cdot\mathbf{u}}}{\gamma_n} \cdot \sum_{\pm} \frac{e^{-\gamma_n(|a_{2\perp}|\mp u_\perp)}}{e^{|a_{2\perp}|\pm jk_{n,\perp}} - e^{-|a_{2\perp}|\gamma_n}} \end{aligned} \tag{2.26}$$

$\gamma_n = \sqrt{|\mathbf{k}_{n,\|}|^2-\beta^2}$, $\mathbf{k}_n = \mathbf{k}+n\mathbf{b}_1$, $\mathbf{k}_{n,\|}$ is the projection of $\mathbf{k}_n$ onto $\mathbf{a}_1$ direction. $k_{n,\perp}$, $a_{2,\perp}$, and $u_\perp$ are the projections of $\mathbf{k}_n$, $\mathbf{a}_2$, and $\mathbf{u}$ onto a unit vector normal to $\mathbf{a}_1$, respectively.

The form in the spatial domain converges very slowly. The form in the spectral domain has fast convergence when $|u_\perp|$ is large. When $|u_\perp|$ is small, Φ_H converges slowly. The acceleration technique for G_p can be applied to speed up the convergence of Φ_H.

In [19], the following auxiliary differential-integral system are proposed, which has the same band structure as the 2-D metallic crystal.

$$\nabla^2\phi + \beta^2(\phi + \int_C w\Phi_p ds') = 0 \tag{2.27}$$

$$\phi(\boldsymbol{\rho}) + \int_C w(\boldsymbol{\rho}')\Phi_p(\boldsymbol{\rho},\boldsymbol{\rho}')dl' = 0, \quad \boldsymbol{\rho} \in C \tag{2.28}$$

where C is the boundary of the PEC object. It has been proved in [19] that he auxiliary function ϕ has the continuous derivatives up to the second order in the unit cell. This is why the plane-wave expansion of ϕ converges fast. E_z is related to the auxiliary function ϕ by

$$E_z(\boldsymbol{\rho}) = \phi(\boldsymbol{\rho}) + \int_C w(\boldsymbol{\rho}')\Phi_p(\boldsymbol{\rho},\boldsymbol{\rho}')dl' \tag{2.29}$$

Φ_p is the pseudo-periodic function at $\beta = 0$, and ϕ can be expanded into the Floquet's modes

$$\phi(\boldsymbol{\rho}) = \sum_{\mathbf{J}} c_{\mathbf{J}} g_{\mathbf{J}}(\boldsymbol{\rho}) \tag{2.30}$$

where

$$g_{\mathbf{J}}(\boldsymbol{\rho}) = \frac{1}{\sqrt{\Omega}} e^{-j(\mathbf{k}+\boldsymbol{\kappa}_{\mathbf{J}})\cdot\boldsymbol{\rho}} \tag{2.31}$$

$g_{\mathbf{J}}$ is with the orthogonality over the unit cell Ω

$$\int_\Omega g_{\mathbf{J_1}}(\boldsymbol{\rho}) g^*_{\mathbf{J_2}}(\boldsymbol{\rho}) ds = \delta_{\mathbf{J_1}\mathbf{J_2}} \tag{2.32}$$

Substituting (2.30) into (2.27), multiplying $g_{\mathbf{J}}$ on both sides of (2.27), and integrating over Ω, one obtains

$$(\beta^2 - |\mathbf{k}+\boldsymbol{\kappa}_{\mathbf{J}}|^2)c_{\mathbf{J}} + \frac{\beta^2}{|\mathbf{k}+\boldsymbol{\kappa}_{\mathbf{J}}|^2}\int_C w(\boldsymbol{\rho}')g^*_{\mathbf{J}}(\boldsymbol{\rho}')dl' = 0 \tag{2.33}$$

Thus,

$$\frac{1}{|\mathbf{k}+\boldsymbol{\kappa}_{\mathbf{J}}|^2}c_{\mathbf{J}} + \frac{1}{|\mathbf{k}+\boldsymbol{\kappa}_{\mathbf{J}}|^4}\int_C w(\boldsymbol{\rho}')g^*_{\mathbf{J}}(\boldsymbol{\rho}')dl' = \frac{1}{\beta^2}c_{\mathbf{J}} \tag{2.34}$$

Substituting (2.30) into (2.28) and using the point-matching method, one can obtain

$$\mathbf{w} = -\mathbf{A}_3^{-1}\mathbf{A}_4\mathbf{c} \tag{2.35}$$

where

$$\mathbf{c} = \begin{bmatrix} c_1 & \ldots & c_s & \ldots & c_S \end{bmatrix}^T \tag{2.36}$$

$$\mathbf{w} = \begin{bmatrix} w_1 & \dots & w_r & \dots & w_R \end{bmatrix}^T \tag{2.37}$$

$$\mathbf{A}_4 = \begin{bmatrix} g_1(\boldsymbol{\rho}_1) & \cdots & g_S(\boldsymbol{\rho}_1) \\ \vdots & \ddots & \vdots \\ g_1(\boldsymbol{\rho}_R) & \cdots & g_S(\boldsymbol{\rho}_R) \end{bmatrix}_{R\times S} \tag{2.38}$$

$$\mathbf{A}_3 = \begin{bmatrix} \int_{l_1} \Phi_p(\boldsymbol{\rho}_1, \boldsymbol{\rho}')dl' & \cdots & \int_{l_R} \Phi_p(\boldsymbol{\rho}_1, \boldsymbol{\rho}')dl' \\ \vdots & \ddots & \vdots \\ \int_{l_1} \Phi_p(\boldsymbol{\rho}_R, \boldsymbol{\rho}')dl' & \cdots & \int_{l_R} \Phi_p(\boldsymbol{\rho}_R, \boldsymbol{\rho}')dl' \end{bmatrix}_{R\times R} \tag{2.39}$$

The index r in w_r and $\boldsymbol{\rho}_r$ corresponds to the rth point function, and s in c_s and g_s corresponds to the sth Floquet's mode. R and S are the number of the pulse basis functions and Floquet's modes, respectively. Discretizing (2.34) and applying (2.35) yields

$$(\mathbf{A}_1 - \mathbf{A}_2\mathbf{A}_3^{-1}\mathbf{A}_4)\mathbf{c} = \frac{1}{\beta^2}\mathbf{c} \tag{2.40}$$

where

$$\mathbf{A}_1 = \begin{bmatrix} \frac{1}{|\mathbf{k}+\boldsymbol{\kappa}_1|^2} & & \\ & \ddots & \\ & & \frac{1}{|\mathbf{k}+\boldsymbol{\kappa}_S|^2} \end{bmatrix}_{S\times S} \tag{2.41}$$

$$\mathbf{A}_2 = \begin{bmatrix} \frac{1}{|\mathbf{k}+\boldsymbol{\kappa}_1|^4} \int_{l_1} g_1^*(\boldsymbol{\rho}_1)dl & \cdots & \frac{1}{|\mathbf{k}+\boldsymbol{\kappa}_1|^4} \int_{l_R} g_1^*(\boldsymbol{\rho}_1)dl \\ \vdots & \ddots & \vdots \\ \frac{1}{|\mathbf{k}+\boldsymbol{\kappa}_S|^4} \int_{l_1} g_S^*(\boldsymbol{\rho}_1)dl & \cdots & \frac{1}{|\mathbf{k}+\boldsymbol{\kappa}_S|^4} \int_{l_R} g_S^*(\boldsymbol{\rho}_1)dl \end{bmatrix}_{S\times R} \tag{2.42}$$

(2.40) is a standard eigensystem with the eigenvalues of $\frac{1}{\beta^2}$. The subroutines from Netlib are employed for solving this eigenvalue problem. The *LZ* algorithm is applied in the subroutines.

2.2.2 Numerical results

In this example, the circular PEC cylinder in the square unit cell is simulated. Their geometrical centers coincide with each other. $\mathbf{a_1} = \hat{x}a$ and $\mathbf{a_2} = \hat{y}a$. The radius of the cylinder is $R = 0.26a$. Figure 2.6 shows the band structure, i.e., $k - \beta$ diagram.

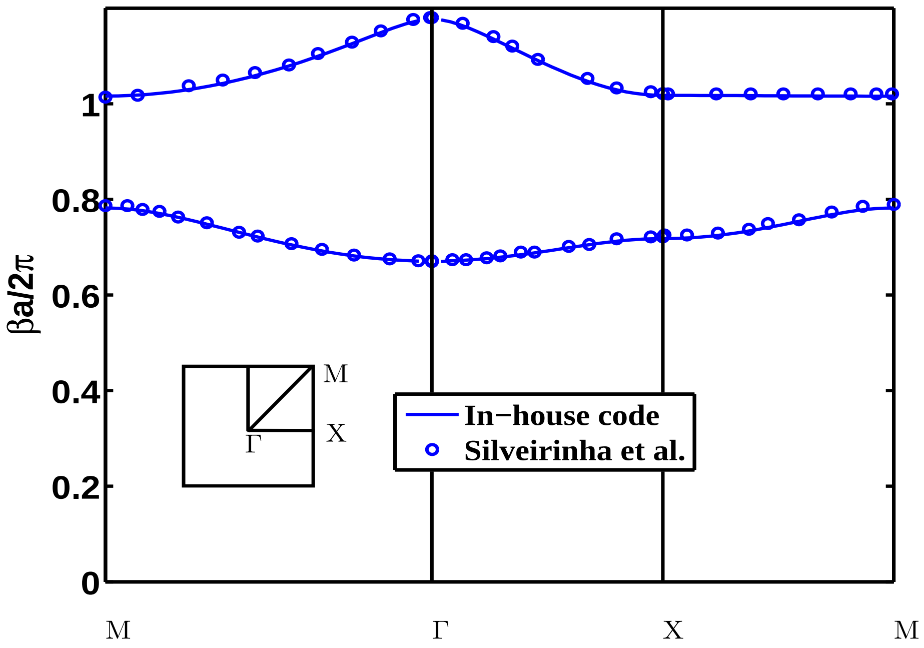

Figure 2.6 Band structure of a doubly periodic array of PEC circular cylinders. $R = 0.26a$. The circle indicates the results taken from [19].

CHAPTER 3 INTEGRAL EQUATION ANALYSIS OF SCATTERING FROM MULTILAYERED PERIODIC ARRAY USING EQUIVALENCE PRINCIPLE AND CONNECTION SCHEME

Recently, the domain decomposition method (DDM) has attracted much attention from the society of computational electromagnetics because of its potential capability and advantages in solving electrically large problems with complex structures. It is natural to apply the DDM to differential equation methods, such as the finite element (FE) [69]-[71] and finite-difference (FD) methods [72]. In addition, DDM also can be employed via the integral equation (IE) method with the aid of the equivalence principle [45]-[46], [73]-[75]. Specially, the integral equation method using periodic boundary condition and a connection scheme is used for modeling of multilayered lossy periodic structures in [44]. This approach can handle the case of the metallic patches at the interface between layers or on the periodic boundary.

In this chapter, an IE approach is developed to investigate the frequency response of a singly-periodic array. By the application of the equivalence principle algorithm and connection scheme (EPACS), the case of the periodic array filled with different media in different layers can be treated [44]. The computational domain first is restricted to one period of the multilayered array. In one period, each layer can be treated as an individual cell. Then, the equivalence principle can be applied separately to each individual cell to obtain the integral equations for equivalent currents on the outside boundary of the cell and the perfect electric conductor (PEC) surface. In general, when the cells are not overlapping or connected with each other, it is necessary to build up the relationship between them by applying IE to their outside boundary [46]. However, for the multilayered periodic structure, two neighboring cells are connected via the same interface. Thus, by combining the periodic boundary condition (PBC) with the connection scheme, the relationship can be established between the currents or fields on the topmost and bottommost surfaces. Finally, two integral equations on the topmost and bottommost surfaces, which involve the periodic Green's function, are required to establish the complete equation system. After seeking the solution of equivalent currents on the topmost and bottommost surfaces, the proper way is proposed to correctly calculate the current on the surface of PEC object.

Moreover, based on EPACS, an effective approach is proposed to handle the semi-infinitely layered case in which one unit consisting of several layers is repeated infinitely along one direction. Each unit can be regarded as a two-port network. For this semi-infinitely layered array, the impedance matrix representing the relationship between the equivalent magnetic and electric currents on the top surface of each unit should be identical because the network is infinitely extended when one looks into it from the top surface of any unit. Based on this fact, the equation for this impedance matrix can be established by EPACS and solved using a proper iterative method. After obtaining the impedance matrix, the integral equation on the topmost surface is required to construct the complete system of equations for solving the fields or currents on the top surfaces. Then the reflection coefficients of Floquet's harmonics can be found. It should be mentioned that the direct IE approach definitely cannot handle the case of semi-infinitely layered array since the number of unknowns for the direct IE approach will be infinite. Finally, numerical results are given to verify the proposed approaches.

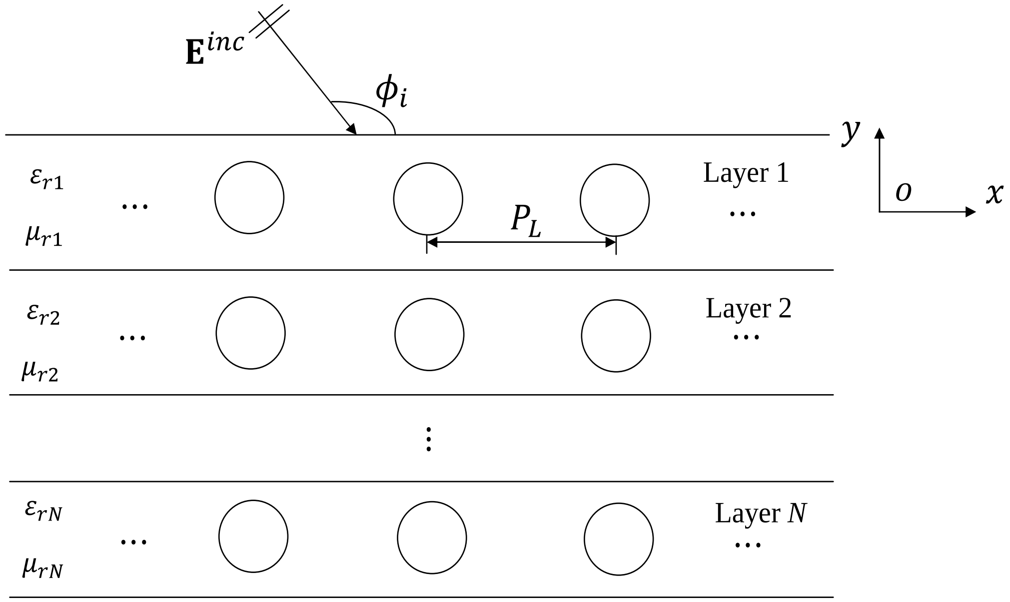

Figure 3.1 Multilayered infinitely periodic PEC array with a period of P_L along x-direction.

3.1 Formulation

In this chapter, a 2-D scattering problem is considered. The scatterers are assumed to be infinitely long along z-direction. Figure 3.1 shows the N-layer infinite periodic PEC cylinder array, whose period is P_L along x-direction. This array is located in free space. It is filled with different media with relative permittivity ϵ_{ri} and permeability μ_{ri} in different layers ($i = 1, 2, \cdots, N$). ϵ_{ri} and μ_{ri} can be complex numbers. The PEC objects are buried inside the media and their cross section may vary from layer to layer. The incident plane wave $\mathbf{E}^{inc} = \mathbf{E_0}e^{-j\mathbf{k}\cdot\boldsymbol{\rho}}$ impinges on the array from free space. Its wave vector is given by $\mathbf{k} = \hat{x}k_x + \hat{y}k_y$, where $k_x = -\beta_0 \cos\phi_i$, $k_y = -\beta_0 \sin\phi_i$, $\beta_0 = \omega\sqrt{\mu_0\epsilon_0}$, and ϕ_i are the incident angles.

3.1.1 Multilayered array of PEC

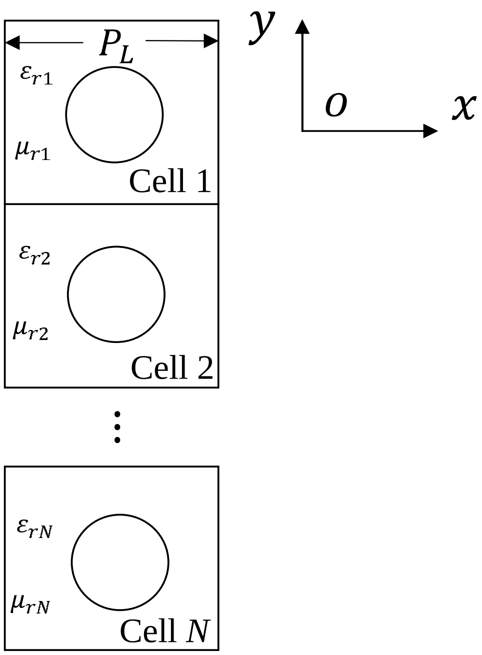

Figure 3.2 Cells in each layer.

Because the array is infinitely periodic along x-direction, one may consider just one cell in each layer shown in Figure 3.2. In this work, the TMz case is considered. Without loss of generality, the integral equation is applied to Cell 1 shown in Figure 3.3. Assume E_{o1} and J_{o1} are the electric field and current on the interior side of outer surface C_o, respectively. E_{o1} includes E_{l1}, E_{r1}, E_{t1}, and E_{b1}. J_{o1} includes J_{l1}, J_{r1}, J_{t1} and J_{b1} . J_{i1} is the electric current on the inner surface C_i (i.e. PEC surface), as shown in Figure 3.3. A problem equivalent to the original problem internal to C_o can be set up as follows. Let the original field exists internal to C_o with the original medium, and null field exists external to C_o with the same medium as the original one internal to C_o. To support this field, the equivalent magnetic and electric currents ($\mathbf{M} = \hat{\tau} E_z$, $\mathbf{J} = \hat{z} J_z$) must exist on C_o. Hence, the electric field integral equations (EFIE) can be found

$$\begin{aligned} -\frac{1}{2}E_{o1} + j\beta_1\eta_1(A_{zo} - A_{zi}) + \fint_{C_o} E_{o1}\frac{\partial G_1}{\partial n'}dl' = 0, \quad &\text{on } C_o \\ j\beta_1\eta_1(A_{zo} - A_{zi}) + \int_{C_o} E_{o1}\frac{\partial G_1}{\partial n'}dl' = 0, \quad &\text{on } C_i \end{aligned} \tag{3.1}$$

where

$$A_{zo} = \int_{C_o} J_{o1}(l')G_1(\boldsymbol{\rho}, \boldsymbol{\rho}')dl'$$

$$A_{zi} = \int_{C_i} J_{i1}(l')G_1(\boldsymbol{\rho}, \boldsymbol{\rho}')dl'$$

$$\frac{\partial G_1}{\partial n'} = (\hat{t} \times \hat{z}) \cdot \nabla G_1$$

$$G_1(\boldsymbol{\rho}, \boldsymbol{\rho'}) = \frac{\mathrm{H}_0^{(2)}(\beta_1 R)}{4j}$$

$$R = |\boldsymbol{\rho} - \boldsymbol{\rho'}|, \quad \beta_1 = \beta_0\sqrt{\mu_{r1}\epsilon_{r1}}.$$

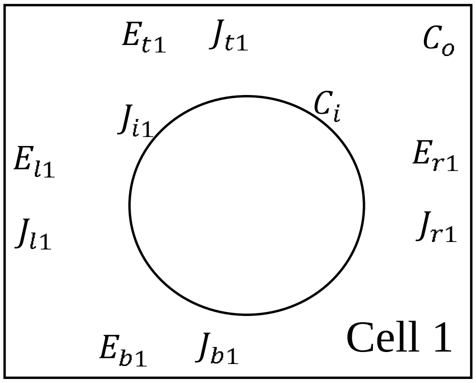

Figure 3.3 Unknown field and current on the interior side of the outer surface C_o and inner surface C_i of Cell 1.

Because the relative permittivity and permeability in the Green's function can be complex numbers, the present approach can handle the case where the media in each layer are lossy. Then, discretization of the integral equations yields

$$0 = A_{E_oE_o}E_{o1} + A_{E_oJ_o}J_{o1} - A_{E_oJ_i}J_{i1} \tag{3.2}$$

on C_o and

$$0 = A_{J_iE_o}E_{o1} + A_{J_iJ_o}J_{o1} - A_{J_iJ_i}J_{i1} \tag{3.3}$$

on C_i. Assume the dimension of E_{o1}, J_{o1}, and J_{i1} to be $N_1 \times 1$, $N_1 \times 1$, and $N_2 \times 1$, respectively. $A_{E_oE_o}$, $A_{E_oJ_o}$, $A_{E_oJ_i}$, $A_{J_iE_o}$, $A_{J_iJ_o}$, and $A_{J_iJ_i}$ are matrices with the dimensions $N_1 \times N_1$, $N_1 \times N_1$, $N_1 \times N_2$, $N_2 \times N_1$, $N_2 \times N_1$, and $N_2 \times N_2$, respectively. Then, the unknowns J_{i1} on C_i can be eliminated and the information on C_i can be transferred to the outer surface C_o. From (3.3), one can get

$$J_{i1} = A^{-1}_{J_iJ_i}(A_{J_iE_o}E_{o1} + A_{J_iJ_o}J_{o1}) \tag{3.4}$$

Substituting (3.4) into (3.2) yields,

$$TE_{o1} = SJ_{o1} \tag{3.5}$$

where

$$\begin{aligned} T &= -A_{E_oJ_i}A^{-1}_{J_iJ_i}A_{J_iE_o} + A_{E_oE_o} \\ S &= A_{E_oJ_i}A^{-1}_{J_iJ_i}A_{J_iJ_o} - A_{E_oJ_o} \end{aligned}$$

In order to obtain the relationship between the top and bottom surfaces, the unknowns on the left and right sides of the cell have to be eliminated by applying the periodic boundary condition

$$\begin{aligned} E_{r1} &= E_{l1}e^{-jk_xP_L} \\ J_{r1} &= -J_{l1}e^{-jk_xP_L} \end{aligned} \tag{3.6}$$

Through the matrix manipulation, one can obtain

$$\begin{bmatrix} E_{t1} \\ E_{b1} \end{bmatrix} = R^{(1)} \begin{bmatrix} J_{t1} \\ J_{b1} \end{bmatrix} \tag{3.7}$$

where $R^{(1)}$ can be rewritten as

$$R^{(1)} = \begin{bmatrix} R_{11}^{(1)} & R_{12}^{(1)} \\ R_{21}^{(1)} & R_{22}^{(1)} \end{bmatrix} \tag{3.8}$$

The details for derivation of $R^{(1)}$ are given in Appendix A. In a similar manner, for layer $i+1$, one can obtain

$$\begin{bmatrix} E_{t(i+1)} \\ E_{b(i+1)} \end{bmatrix} = R^{(i+1)} \begin{bmatrix} J_{t(i+1)} \\ J_{b(i+1)} \end{bmatrix} \tag{3.9}$$

where $R^{(i+1)}$ is found by replacing ϵ_{r1} and μ_{r1} with $\epsilon_{r(i+1)}$ and $\mu_{r(i+1)}$. If each layer is identical, it holds that $R^{(i+1)} = R^{(1)}$ ($i = 1, \cdots, N-1$), which indicates that one can save CPU time for creating $R^{(i+1)}$.

In the next step, the connection scheme will be applied to eliminate the unknowns between Layer 1 and Layer N. From (3.7), one gets the initial relationship

$$\begin{bmatrix} E_{t1} \\ E_{b1} \end{bmatrix} = A^{(1)} \begin{bmatrix} J_{t1} \\ J_{b1} \end{bmatrix} \tag{3.10}$$

where

$$A^{(1)} = R^{(1)}$$

Assume the following relationship has been found between Layer 1 and Layer i ($1 \leq i \leq N-1$)

$$\begin{bmatrix} E_{t1} \\ E_{bi} \end{bmatrix} = A^{(i)} \begin{bmatrix} J_{t1} \\ J_{bi} \end{bmatrix} \tag{3.11}$$

where

$$A^{(i)} = \begin{bmatrix} A_{11}^{(i)} & A_{12}^{(i)} \\ A_{21}^{(i)} & A_{22}^{(i)} \end{bmatrix}$$

Combining (3.9) and (3.11) and using the boundary condition of continuity of the tangential field

$$\begin{bmatrix} E_{bi} \\ J_{bi} \end{bmatrix} = \begin{bmatrix} E_{t(i+1)} \\ -J_{t(i+1)} \end{bmatrix} \tag{3.12}$$

one can get the relationship between Layer 1 and Layer $i+1$

$$\begin{bmatrix} E_{t1} \\ E_{b(i+1)} \end{bmatrix} = A^{(i+1)} \begin{bmatrix} J_{t1} \\ J_{b(i+1)} \end{bmatrix} \tag{3.13}$$

where

$$A^{(i+1)} = \begin{bmatrix} A_{11}^{(i)} - A_{12}^{(i)}(A_{22}^{(i)} + R_{11}^{(i+1)})^{-1}A_{21}^{(i)} & A_{12}^{(i)}(A_{22}^{(i)} + R_{11}^{(i+1)})^{-1}R_{12}^{(i+1)} \\ R_{21}^{(i+1)}(A_{22}^{(i)} + R_{11}^{(i+1)})^{-1}A_{21}^{(i)} & R_{22}^{(i+1)} - R_{21}^{(i+1)}(A_{22}^{(i)} + R_{11}^{(i+1)})^{-1}R_{12}^{(i+1)} \end{bmatrix} \tag{3.14}$$

Thus, one can recursively find the relationship between Layer 1 and Layer N by using (3.14)

$$\begin{bmatrix} E_{t1} \\ E_{bN} \end{bmatrix} = A^{(N)} \begin{bmatrix} J_{t1} \\ J_{bN} \end{bmatrix} \tag{3.15}$$

It should be noted that if each layer is identical, the logarithm algorithm can be applied to speed up the procedure for finding $A^{(N)}$. For $N = 2^{L_0}$, the N-time process of applying the connection scheme can be reduced to that of L_0 times by replacing $R^{(i+1)}$ with $A^{(i)}$ in (3.14).

In addition to (3.15), two more conditions are required to solve the scattering problem. On the top surface of Layer 1, the following equation holds

$$E_z^{inc} = \frac{1}{2}E_z + j\beta_0\eta_0 \int J_z(l')G_p dl' \tag{3.16}$$

where

$$G_p = \sum_M \frac{H_0^{(2)}(\beta_0|\boldsymbol{\rho} - \boldsymbol{\rho}' - \hat{x}MP_L|)}{4j} e^{-jk_x MP_L}$$

since $\frac{\partial G_p}{\partial n} = 0$ for the flat surface, $\int E_z(l')\frac{\partial G_p}{\partial n}dl'$ is dropped. G_p is the periodic Green's function in free space, and can be efficiently and accurately calculated by using Veysoglu's transformation or the other transformations [67], [68]. Discretization of (3.16) yields

$$E^{inc} = A_{E_{t1}E_{t1}}E_{t1} + A_{E_{t1}J_{t1}}J_{t1} \tag{3.17}$$

And on the bottom surface of Layer N,

$$0 = \frac{1}{2}E_z + j\beta_0\eta_0 \int J_z(l')G_p dl' \tag{3.18}$$

Discretization of (3.18) yields

$$0 = A_{E_{bN}E_{bN}}E_{bN} + A_{E_{bN}J_{bN}}J_{bN} \tag{3.19}$$

Actually, (3.16) and (3.18) are obtained by setting up the problems equivalent to the original problem above the topmost surface and below the bottommost surface, respectively. Because there is no source exciting the incident field in the region below the bottom surface of Layer N, no incident field contributes to the total field in (3.18).

Combining (3.15), (3.17), and (3.19) yields

$$C\left[\begin{array}{cccc} E_{t1} & E_{bN} & J_{t1} & J_{bN}\end{array}\right]^T = \left[\begin{array}{cccc} E^{inc} & 0 & 0 & 0\end{array}\right]^T \tag{3.20}$$

where

$$C = \left[\begin{array}{cccc} A_{E_{t1}E_{t1}} & 0 & A_{E_{t1}J_{t1}} & 0 \\ 0 & A_{E_{bN}E_{bN}} & 0 & A_{E_{bN}J_{bN}} \\ I & 0 & -A_{11}^{(N)} & -A_{12}^{(N)} \\ 0 & I & -A_{21}^{(N)} & -A_{22}^{(N)} \end{array}\right]$$

Moreover, the formulations are applicable to the case in which there is no PEC object inside the cell through just replacing T and S in (3.5) by

$$\begin{aligned} T &= A_{E_oE_o} \\ S &= -A_{E_oJ_o} \end{aligned} \tag{3.21}$$

After solving (3.20), the other fields and currents of all the cells can be calculated. There are two ways to attempt this. The first one is to get E_{b1} and J_{b1} by using (3.7) since E_{t1} and J_{t1} have been found. Similarly one can obtain E_{bi} and J_{bi} $(1 < i < N)$ layer by layer from the top to bottom with the aid of (3.12) and (3.9). Unfortunately, the condition number of $R_{12}^{(1)}$ is extremely large so that one cannot accurately calculate the inverse of $R_{12}^{(1)}$ which is required to solve (3.7) for E_{b1} and J_{b1}. Thus, one should abandon the first way and consider the other way. In fact, during the procedure of achieving (3.13), one can find

$$\left[\begin{array}{c} E_{bi} \\ J_{bi} \end{array}\right] = B^{(i)} \left[\begin{array}{c} J_{t1} \\ J_{b(i+1)} \end{array}\right] \tag{3.22}$$

where

$$B^{(i)} = \left[\begin{array}{cc} \left(I - A_{22}^{(i)}(A_{22}^{(i)} + R_{11}^{(i+1)})^{-1}\right) A_{21}^{(i)} & A_{22}^{(i)}(A_{22}^{(i)} + R_{11}^{(i+1)})^{-1}R_{12}^{(i+1)} \\ -(A_{22}^{(i)} + R_{11}^{(i+1)})^{-1}A_{21}^{(i)} & (A_{22}^{(i)} + R_{11}^{(i+1)})^{-1}R_{12}^{(i+1)} \end{array}\right] \tag{3.23}$$

Because J_{t1} and J_{bN} are known from (3.20), one can obtain recursively E_{bi} and J_{bi} from the bottom to top by using (3.22). For Cell 1, E_{l1}, E_{r1}, J_{l1}, and J_{r1} are obtained through (A.4) (in Appendix A) and

(3.6). Then one can find the current J_{i1} on the PEC by using (3.4). In the same manner, the current on the PEC of the other cells can be found. Numerical results will be shown to verify the second way.

3.1.2 Semi-infinitely layered array of PEC

Assume a unit consisting of N_0 ($N_0 \geq 1$) layers is repeated infinitely along $-\hat{y}$ direction. Each unit must be identical to the other units. However, it is unnecessary for each layer to be the same in one unit. Each unit can be regarded as a two-port network and the semi-infinitely layered array is equivalent to the connection of infinite number of two-port networks. For this semi-infinitely layered array, the impedance matrix representing the relationship between the equivalent magnetic and electric currents on the top surface of each unit should be identical because the network is infinitely extended when one looks into it from the top surface of any unit. Let P_0 denote each of these impedance matrices. Thus, by using the tangential continuity condition one obtains

$$\begin{aligned} E_{t1} &= P_0 J_{t1} \\ E_{bN_0} &= -P_0 J_{bN_0} \end{aligned} \tag{3.24}$$

On the other hand, as discussed in the above subsection, by using EPACS one gets

$$\begin{bmatrix} E_{t1} \\ E_{bN_0} \end{bmatrix} = \begin{bmatrix} A_{11}^{(N_0)} & A_{12}^{(N_0)} \\ A_{21}^{(N_0)} & A_{22}^{(N_0)} \end{bmatrix} \begin{bmatrix} J_{t1} \\ J_{bN_0} \end{bmatrix} \tag{3.25}$$

where $A^{(N_0)}$ can be obtained by making use of (3.14) or (3.10). Using the second set of equations from both (3.25) and (3.24), one can get

$$J_{bN_0} = -(P_0 + A_{22}^{(N_0)})^{-1} A_{21}^{(N_0)} J_{t1} \tag{3.26}$$

Substitution of (3.26) into the first set of (3.25) gives

$$E_{t1} = [A_{11}^{(N_0)} - A_{12}^{(N_0)} (P_0 + A_{22}^{(N_0)})^{-1} A_{21}^{(N_0)}] J_{t1} \tag{3.27}$$

Comparing (3.27) with the first set of (3.24), one can achieve

$$P_0 = A_{11}^{(N_0)} - A_{12}^{(N_0)} (P_0 + A_{22}^{(N_0)})^{-1} A_{21}^{(N_0)} \tag{3.28}$$

(3.28) is an equation for unknown matrix P_0. It is impossible to find the explicit solution for P_0. However, it can be solved by using the iterative procedure

$$X_{n+1} = X_n + \alpha[X_n - f(X_n)] \tag{3.29}$$

where α is a relaxation factor, and X is a matrix to be determined, which satisfies $X = f(X)$. Combining (3.17) and the first set of (3.24) gives the complete system of equations

$$\begin{bmatrix} A_{E_{t1}E_{t1}} & A_{E_{t1}J_{t1}} \\ I & -P_0 \end{bmatrix} \begin{bmatrix} E_{t1} \\ J_{t1} \end{bmatrix} = \begin{bmatrix} E^{inc} \\ 0 \end{bmatrix} \tag{3.30}$$

After obtaining E_{t1} and J_{t1}, one can find E_{b1} and J_{b1} by using (3.24) and (3.26). Following the procedure similar to that for multilayered array, E_{l1}, E_{r1}, J_{l1}, and J_{r1} are obtained and then J_{i1} can be found. In the same manner, one can find the current on PEC surface of the other cells starting from top and going downwards.

Similarly, this approach is applicable to the semi-infinitely layered array without PEC objects inside each layer by means of (3.21).

3.1.3 Floquet's harmonics of scattered fields

The reflection coefficient of Floquet's harmonics can be found after seeking the solution to the integral equation. In this subsection, the expression for the reflection coefficient will be given.

The scattered field E_z^s can be expressed as a superposition of Floquet's harmonics [4]

$$E_z^s = \sum_{m=-\infty}^{\infty} e_m e^{-jk_{xm}x} e^{-\sqrt{k_{xm}^2 - \beta_0^2}\,y}, \quad y > y_0 \tag{3.31}$$

where $k_{xm} = k_x + 2m\pi/P_L$. Here y_0 is the y-coordinate of the top surface of Cell 1. The Floquet's harmonics are orthogonal to each other over one period along the x direction. Assume the reference plane is located at $y = y_0$. Thus,

$$\int_{x=0}^{P_L} E_z^s(x, y_0) e^{jk_{xm}x} dx = e_m P_L e^{-\sqrt{k_{xm}^2 - \beta_0^2}\,y_0} \tag{3.32}$$

On the other hand, E_z^s is given in terms of E_z and J_z on the top surface of Cell 1

$$E_z^s = \frac{1}{2} E_z - j\beta_0\eta_0 \int_l J_z(\boldsymbol{\rho}')G_p dl' \tag{3.33}$$

From (3.32) and (3.33), one gets

$$e_m = \frac{e^{\sqrt{k_{xm}^2-\beta_0^2}y_0}}{P_L}\int_{x=0}^{P_L}\left[-j\beta_0\eta_0\int_l J_z(\boldsymbol{\rho}')G_p|_{y=y_0}dl' + \frac{1}{2}E_z\right]e^{jk_{xm}x}dx \tag{3.34}$$

In terms of the definition of scattering matrix in [4], the reflection coefficient of the zeroth propagating harmonic can be expressed by

$$R_0 = \frac{e_0}{E_0}e^{-j2\sqrt{\beta_0^2-k_x^2}y_0} \tag{3.35}$$

When there are no PEC objects inside each layer, the scattering problem reduces to that of reflection of incident wave from multilayered media. For this case, only zeroth harmonics exists, and R_0 is the reflection coefficient of the incident wave from the planar boundary of infinitely extended media. E_z and J_z in (3.34) have been found through (3.20) and (3.30) for cases of multilayered and semi-infinitely layered array, respectively.

3.2 Numerical results

3.2.1 Multilayered periodic array

In the following examples, each cell is assumed to be square. In the first example, we consider a PEC object that is a circular cylinder with the radius $R = 0.15P_L$. All layers are identical with medium of free space. Here the point matching and pulse basis function are applied to obtain the numerical results. The TM wave is incident normally. The numerical results can be found alternatively by directly solving the EFIE applied on the PEC surface [4], which does not involve the equivalence principle and connection scheme. The direct IE approach employs the periodic Green's function instead of the free-space Green's function. The number of elements are 80 and 40 for outside boundary and the PEC surface, respectively. In the direct IE approach, 40 elements are applied to each PEC object surface.

Figures 3.4 and 3.5 show the power reflection coefficient of the zeroth Floquet's harmonic for the one-layer and four-layer cases, respectively. The Fortran program, which is used to calculate the power reflection coefficient, is run on a PC with a 3.2 GHz processor. The CPU time is about 1.5 seconds for each frequency point. There is a good agreement between results from the present approach, and the direct IE and the T-matrix approaches for the one-layer case. Also, the good agreement can be observed between results from the present approach and the direct IE approach for the four-layer case.

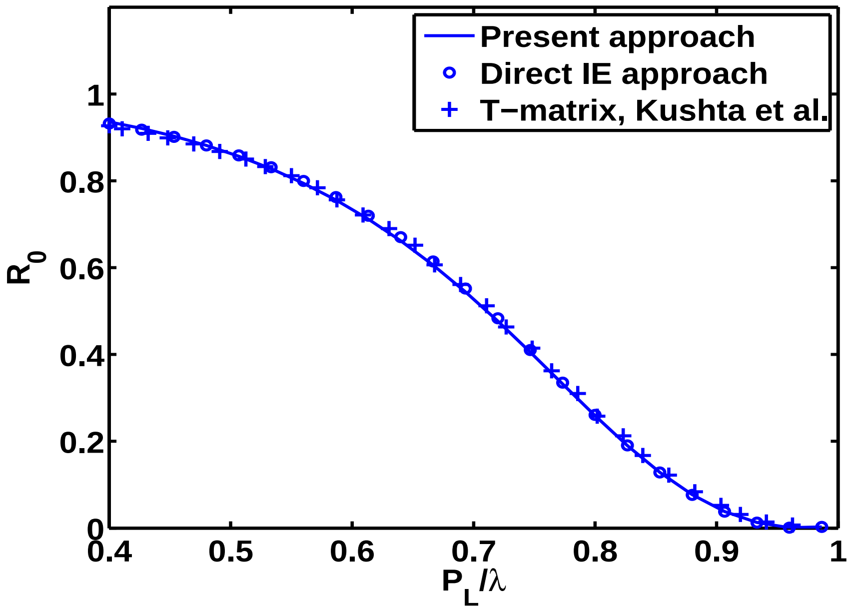

Figure 3.4 Power reflection coefficient of the zeroth Floquet's harmonic of 1-layer array of circular PEC cylinder. $R = 0.15P_L$, $\epsilon_{r1} = 1$, and $\mu_{r1} = 1$. The results of the T-matrix method are taken from [35].

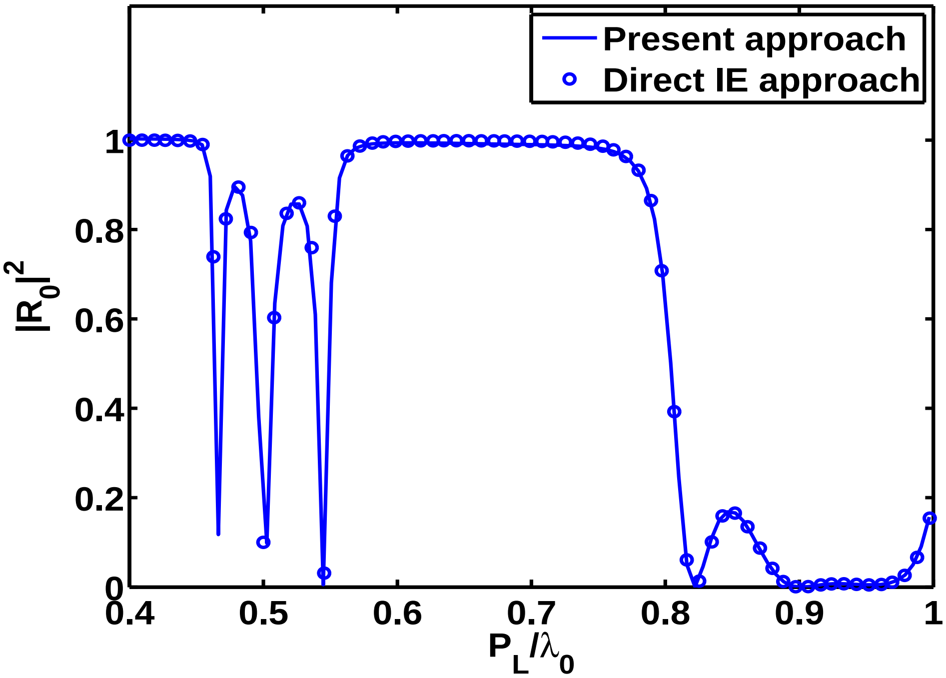

Figure 3.5 Power reflection coefficient of the zeroth Floquet's harmonic of 4-layer array. $R = 0.15P_L$, $\epsilon_{ri} = 1$, and $\mu_{ri} = 1$ $(i = 1, \cdots, 4)$.

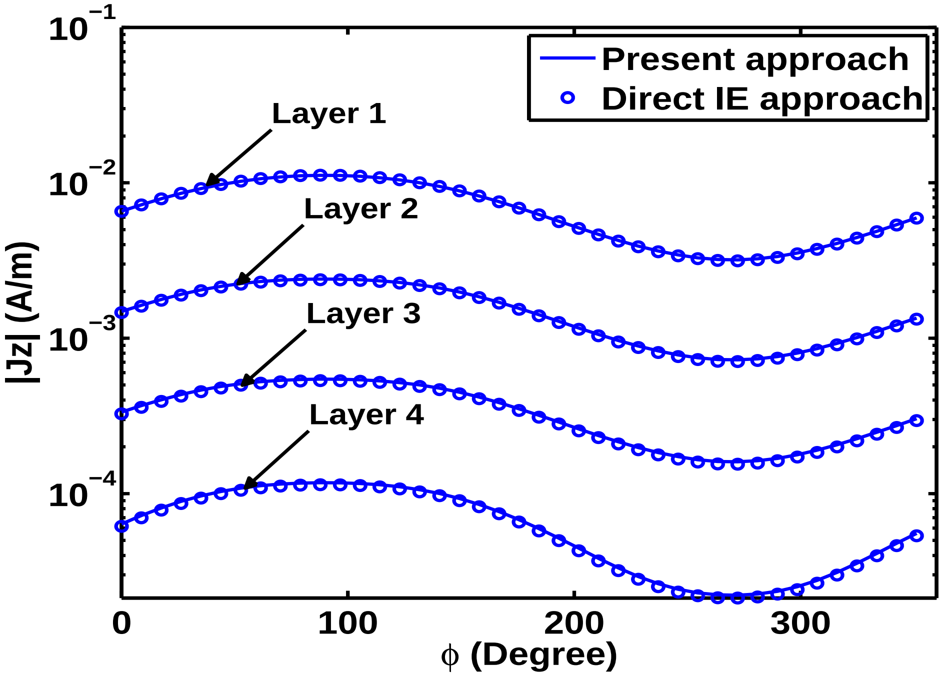

Figure 3.6 Current distribution on circular PEC cylinders of a four-layer array. $R = 0.15P_L$ and $P_L = 0.4\lambda_0$. $\epsilon_{ri} = 1$, and $\mu_{ri} = 1$ $(i = 1, \cdots, 4)$.

Figures 3.6 and 3.7 show the current distribution on PEC surface of the four-layer array at $P_L = 0.4\lambda_0$ and $0.9\lambda_0$, respectively. ϕ is the polar angle about the respective circle center. The results agree well with that of direct IE approach. As shown in Figure 3.5, most of energy is reflected at $P_L = 0.4\lambda_0$, and thus wave can hardly pass through the array. Therefore, the induced current on PEC decreases as the layer index increases. By contrast, the current does not decrease as the layer index increasing at $P_L = 0.9\lambda_0$ since this frequency point is within the passband.

The second example is the three-layer array filled with a lossy medium but without PEC objects inside the cell. Figure 3.8 shows the reflection coefficient of the zeroth Floquet's harmonic R_0 for the three-layer array without PEC object inside. The medium in each layer is lossy. $\epsilon_{r1} = 1 - j0.2$, $\epsilon_{r2} = 2 - j0.2$, $\epsilon_{r3} = 4 - j0.2$, $\mu_{r1} = 1$, $\mu_{r2} = 2$, and $\mu_{r3} = 1$. The CPU time is about 2.0 seconds for each frequency point. There is a good agreement between results from the proposed approach and the analytical solutions. Figure 3.9 shows $|R_0|^2$ for the same array with and without the circular PEC object of $R = 0.15P_L$. Compared with the array without PEC, the array with PEC has the larger reflection at lower frequencies. The PEC objects inside the array play important roles in changing the reflection at

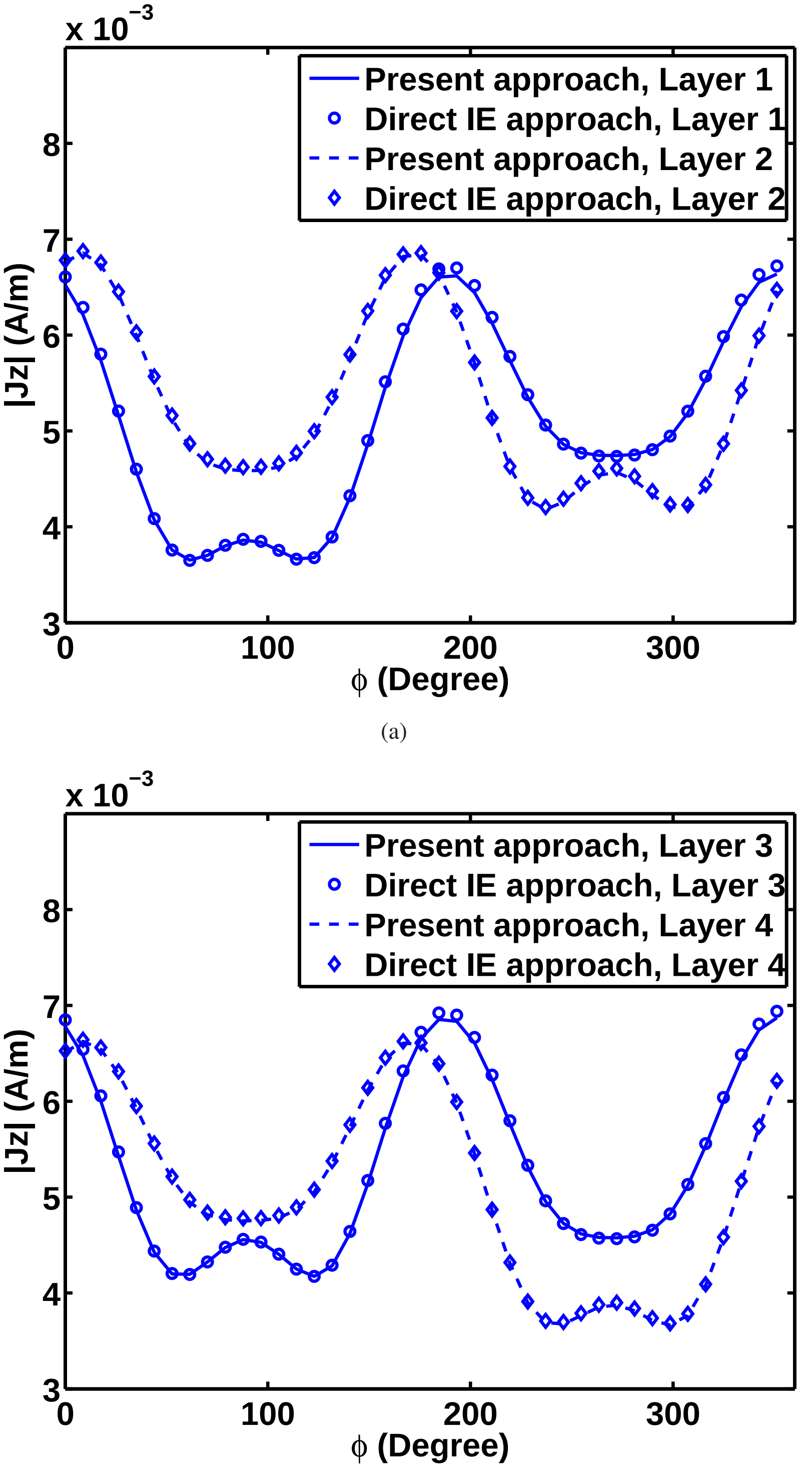

(a)

(b)

Figure 3.7 Current distribution on circular PEC cylinders of a four-layer array. $R = 0.15P_L$ and $P_L = 0.9\lambda_0$. $\epsilon_{ri} = 1$, and $\mu_{ri} = 1$ ($i = 1, \cdots, 4$).

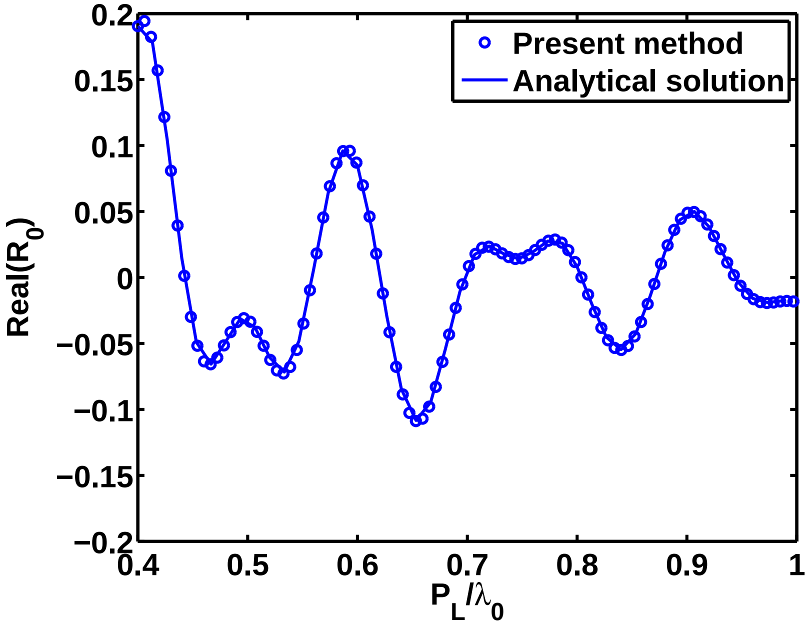

(a) Real part

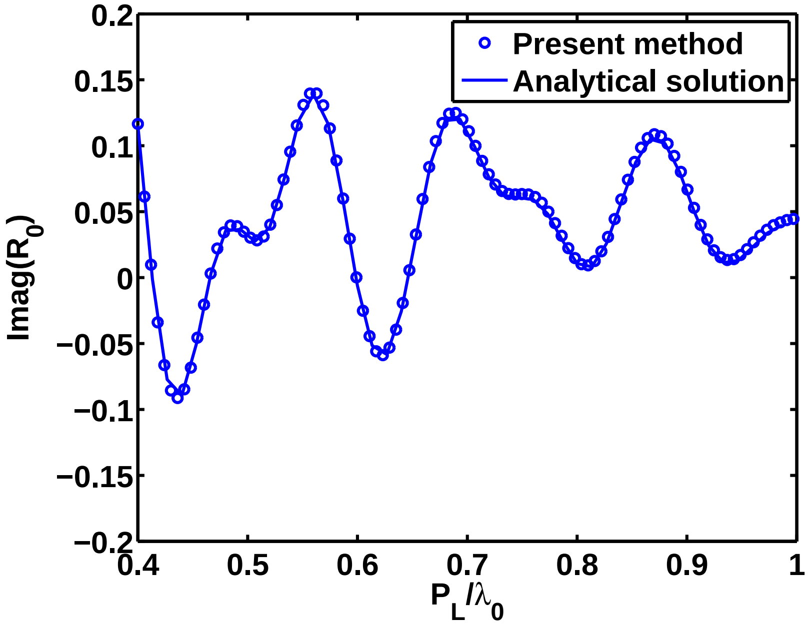

(b) Imaginary part

Figure 3.8 Reflection coefficient R_0 of three-layer media. $\epsilon_{r1} = 1 - j0.2$, $\epsilon_{r2} = 2 - j0.2$, $\epsilon_{r3} = 4 - j0.2$, $\mu_{r1} = 1$, $\mu_{r2} = 2$, and $\mu_{r3} = 1$.

lower frequencies.

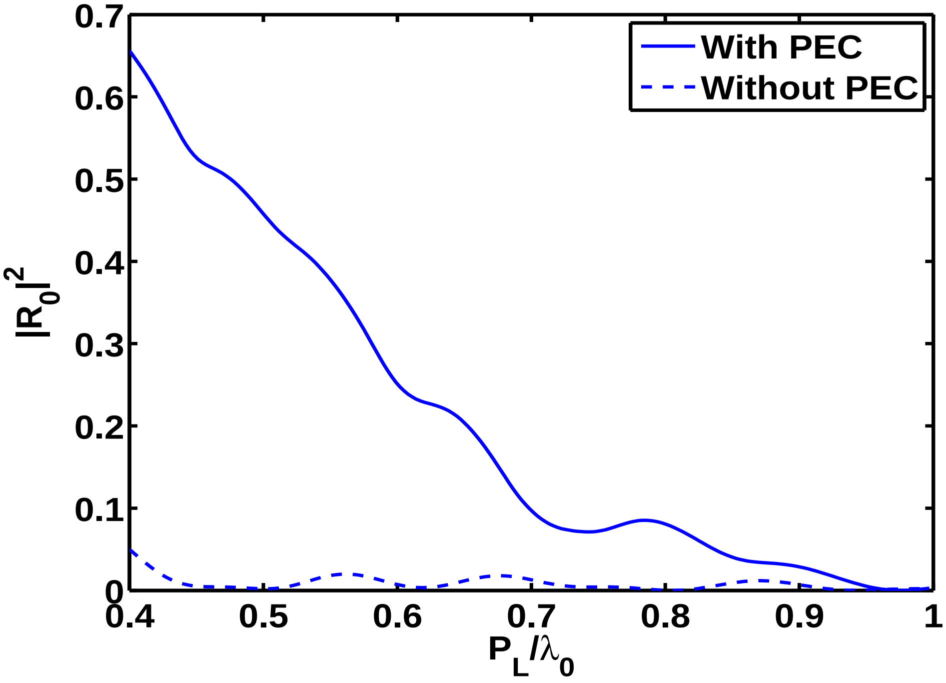

Figure 3.9 Power reflection coefficient $|R_0|^2$ of three-layer media and periodic circular PEC array. $R = 0.15P_L$, $\epsilon_{r1} = 1 - j0.2$, $\epsilon_{r2} = 2 - j0.2$, $\epsilon_{r3} = 4 - j0.2$, $\mu_{r1} = 1$, $\mu_{r2} = 2$, and $\mu_{r3} = 1$.

Figure 3.10 shows the reflection coefficient of a PEC array with 64 identical layers. Each layer has $\epsilon_r = 2 - j0.2$ and $\mu_r = 2$. As shown in this figure, using logarithm algorithm leads to little change in R_0 compared to the scheme without the logarithm algorithm. Thus, it is stable to use the logarithm algorithm for the solution of R_0. Figure 3.11 gives a whole picture for the average CPU time per frequency point versus the number of layers. The CPU time for each connection is short because the number of unknowns for each cell is small. Hence, CPU time does not change too much as the number of layers increases for both schemes with and without the logarithm algorithm. However, for the three-dimensional (3-D) case, the number of unknowns for each cell will increase significantly. In this situation, the logarithm algorithm is expected to play an important role in reducing the CPU time when the number of layers is large.

The integral equation is locally applied to each cell. When N is large, the total CPU time is mainly for constructing $R^{(i)}$ (i is from 1 to N) since the part of CPU time for connection of matrix is negligible.

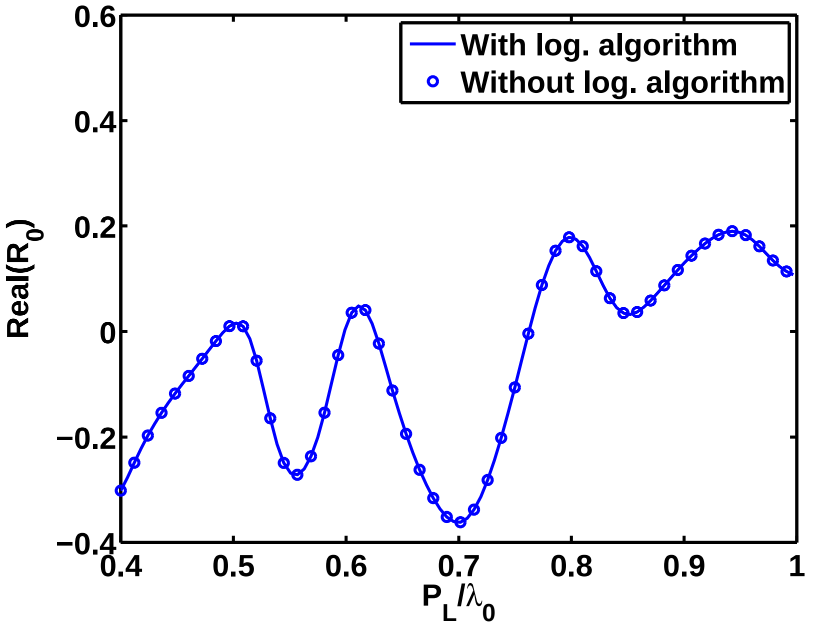

(a) Real part

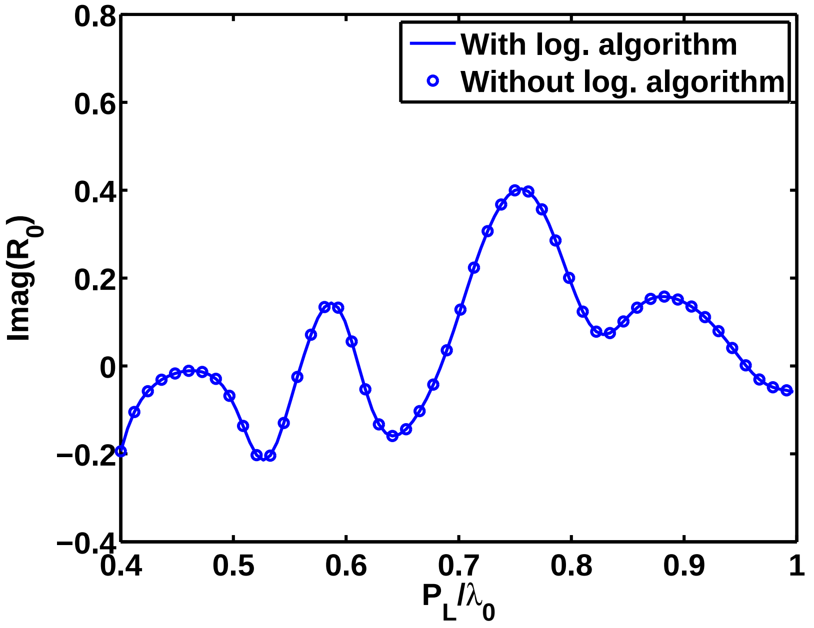

(b) Imaginary part

Figure 3.10 Reflection coefficient R_0 of PEC array with 64 identical layers. $R = 0.15P_L$, $\epsilon_r = 2 - j0.2$ and $\mu_r = 2$.

Thus, the CPU time increases linearly with the number of layers. If each layer is identical (indicating $R^{(i)} = R^{(1)}$), the CPU time is just for constructing $R^{(1)}$ and so independent of N. Thus, one can significantly save the CPU time. Furthermore, the times of connection will be reduced from $N-1$ to $\log_2 N$. However, if the integral equation is applied directly to N PEC objects, the computational complexity is O(N^3) without application of the fast algorithm. Thus, the present approach has computational advantages over the direct IE approach when N is large. In addition, when N is large, the memory requirement for the present approach is also much smaller than that for direct IE approach.

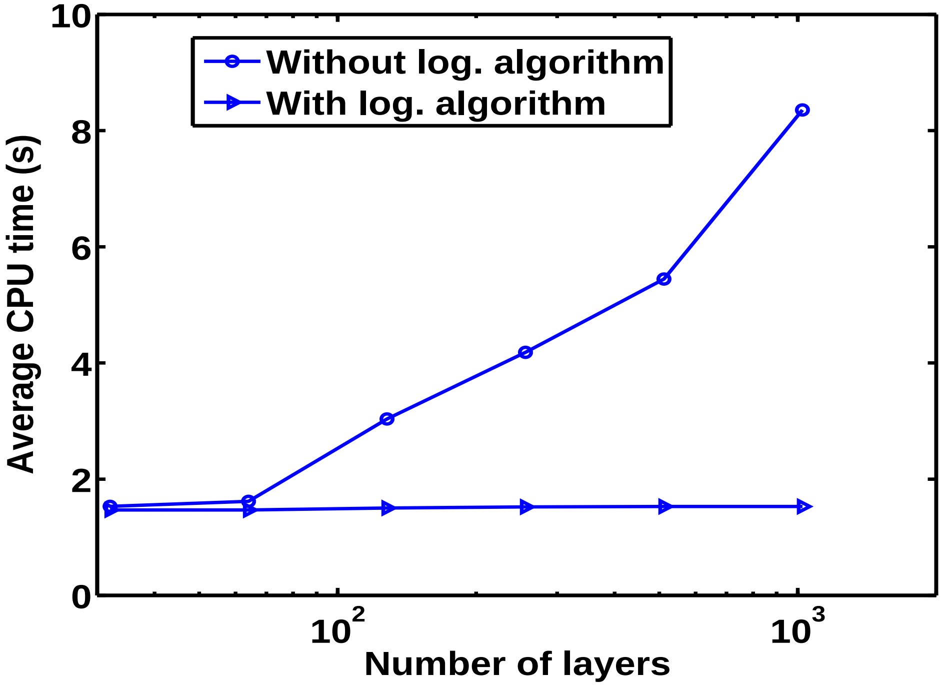

Figure 3.11 Average CPU time per frequency point versus number of layers. $R = 0.15P_L$, $\epsilon_r = 2 - j0.2$ and $\mu_r = 2$.

3.2.2 Semi-infinitely layered periodical array

Before a solution of reflection coefficient of semi-infinitely layered array can be found, it is interesting and necessary to investigate the convergence of P_0. In the following example, the unit being repeated infinitely consists of one layer, namely, $N_0 = 1$. The cell corresponding to each layer is square. The PEC object with radius $0.15P_L$ is located at the center of the cell. The media inside each

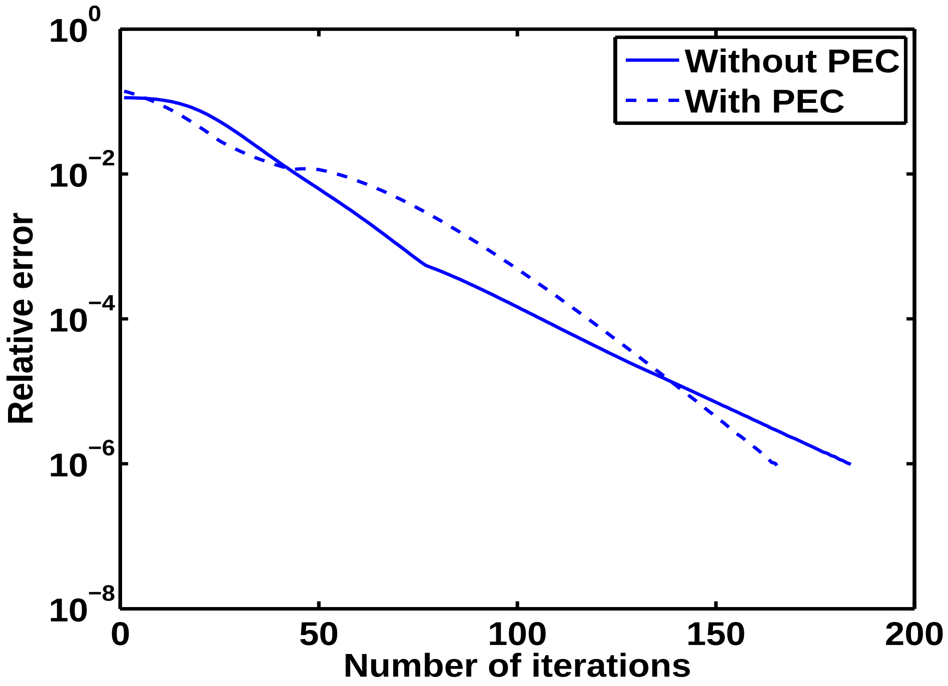

Figure 3.12 Convergence of P_0 with and without circular PEC cylinder. $\epsilon_r = 4 - j0.2$ and $\mu_r = 2$.

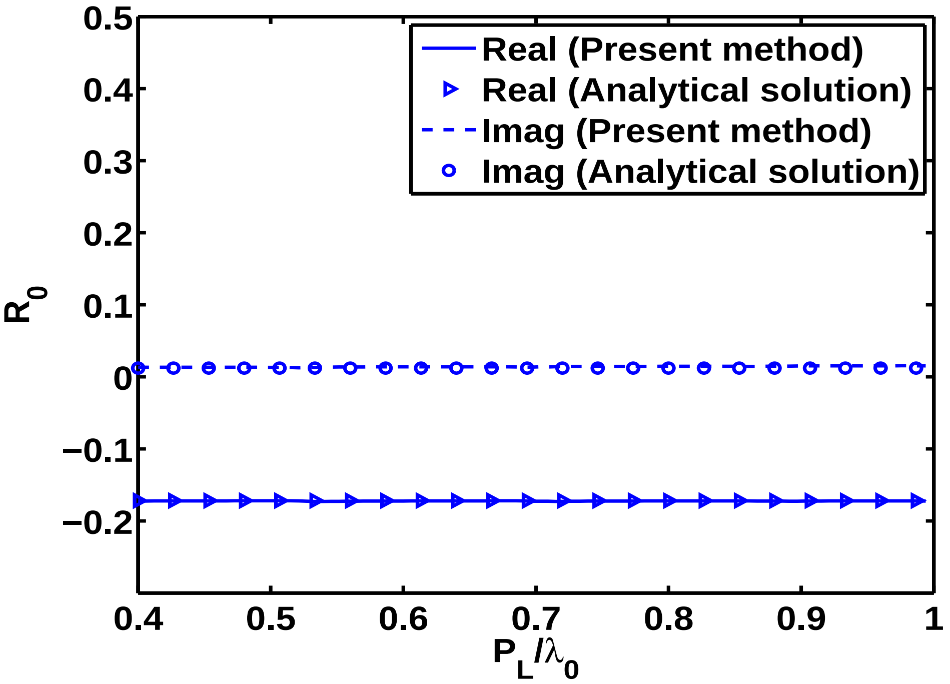

Figure 3.13 Reflection coefficient R_0 of semi-infinitely layered array without PEC object. $\epsilon_r = 4 - j0.2$ and $\mu_r = 2$.

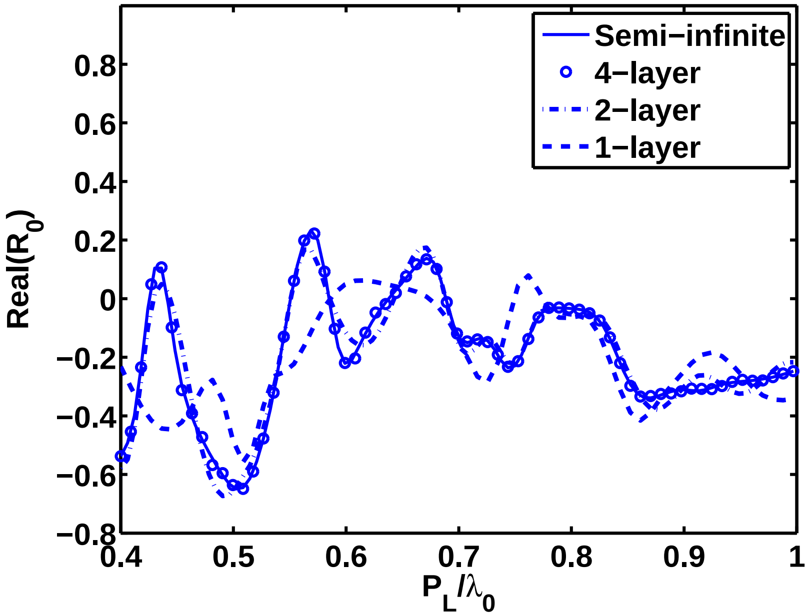

(a) Real part

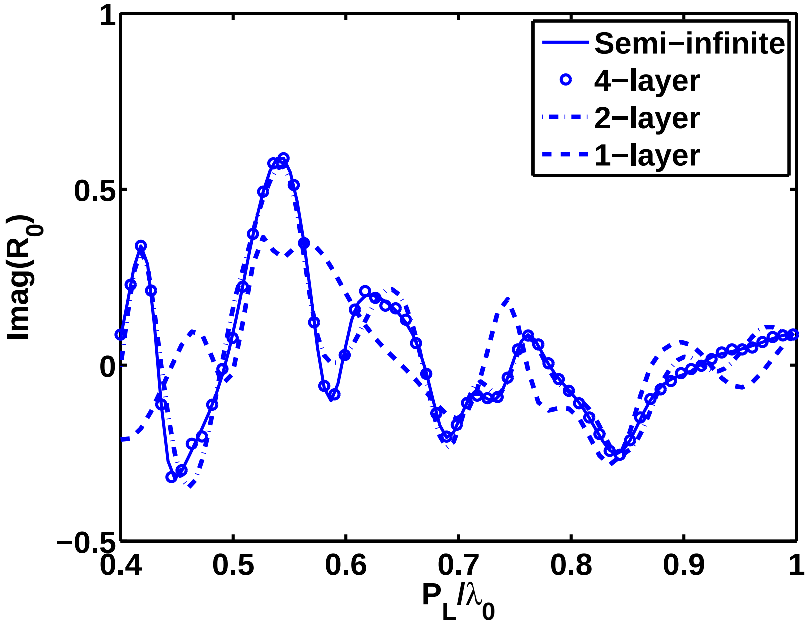

(b) Imaginary part

Figure 3.14 Reflection coefficient R_0 of semi-infinitely layered and multilayered array of circular PEC cylinder. $R = 0.15P_L$, $\epsilon_r = 4 - j0.2$, and $\mu_r = 2$.

cell has $\epsilon_r = 4 - j0.2$ and $\mu_r = 2$. The initial value of elements in P_0 is set to 1.0, and the relaxation factor is set to $\alpha = -0.1$. Figure 3.12 shows a good convergence of P_0 for $P_L = 0.4\lambda_0$. The relative error is defined as

$$\text{Error} = \frac{\max\limits_{i,j}(|P_{0(i,j)}^{n+1} - P_{0(i,j)}^{n}|)}{\max\limits_{i,j}(|P_{0(i,j)}^{n+1}|)} \tag{3.36}$$

It is worth pointing out that the convergence of P_0 may suffer from the resonance problem of integral equation if the media filled in the cells are lossless. The promising remedy is the application of combined field integral equation (CFIE) [76], which will be investigated in our future work.

In addition, Figure 3.13 shows the reflection coefficient of semi-infinitely layered array without PEC objects. There is a good agreement between the results from the proposed methods and the analytical solution. Finally, the reflection coefficient for the semi-infinitely layered array with PEC objects is calculated and compared with that for one-layer, two-layer, and four-layer circular PEC cylinder array. The average CPU time for each frequency point is about 2.2 and 2.4 seconds for the cases with and without PEC objects, respectively. The memory requirement is about 6 MB. Because the media are lossy, when the number of layer increases, the solution should converge to that of the semi-infinitely layered array. Figure 3.14 shows the convergence of the reflection coefficient. When the array has four layers, the results are very close to that of the semi-infinitely layered array.

CHAPTER 4 INTEGRAL-EQUATION ANALYSIS OF SCATTERING FROM DOUBLY PERIODIC ARRAY OF 3-D CONDUCTING OBJECTS

In this chapter, the electric field integral equation (EFIE) formulation in the spatial domain is employed to calculate scattering from the doubly periodic array of PEC objects. The following three issues about the IE approach are addressed [83].

First, the special testing and basis functions are proposed to handle the problem with non-zero normal components of currents at the boundary of one period. As we know, the computational domain for periodic structures is restricted to one period. The objects with periodicity may be truncated by the four-side periodic boundaries (PB). In this case, the electric current flowing out of the boundary of the PEC surface may not be zero. If one adopts the Rao-Wilton-Glission (RWG) basis functions [47] to expand the current, and treat the boundary in the manner which is applied to single PEC plate, namely, does not assign unknowns on the boundary, the solution to the current will be probably inaccurate or even wrong. This is because this procedure enforces the condition of zero outgoing current on the truncated boundary of PEC. In our work, the special test and basis functions on the truncated boundary are proposed to handle this problem.

Second, the relationship is addressed between the scattering from the PEC screen with periodicity and its complementary structure. The Babinet's principle for this dual problem has been proved in several different ways [48]-[50]. This chapter shows a simple way for proof of the Babinet's principle for periodic structures. The proof involves the IE formulation and periodic Green's function. In addition, the relationship for the reflection and transmission coefficients between the PEC screen with periodicity and its complementary structure will be derived using the IE approach. It should be mentioned that this relationship also can be obtained from Babinet's principle [51]. For periodic apertures perforated from the screen, one can apply integral equations about the electric current on the PEC part of the screen.

However, the unknown density near the aperture should be made large enough to achieve the accurate solution for the scattering. In contrast, it will be easier to achieve the convergence of solution if one solves the integral equation for the electric current on PEC patches in its dual problem. Then one may find the solution for scattering from the apertures using the relationship mentioned.

Finally, the acceleration technique in [40] is applied to evaluate the PGF. It has exponential convergence rate and can be implemented easily. One can take advantage of the intrinsic function in Fortran to evaluate the error function involved in [40] since its argument can be real number. The formulations in this technique are appropriately modified so that the new form facilitates numerical calculation for the general cases. Therefore, there will exist no obstacles to effectively evaluate the matrix element of the IE approach.

4.1 Formulation

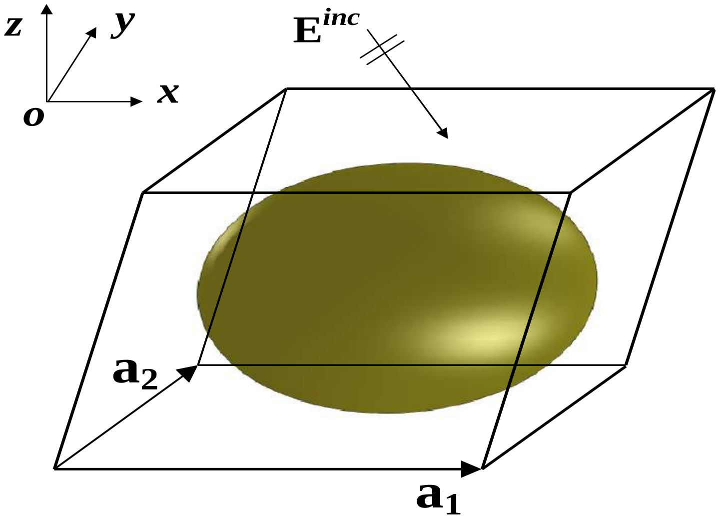

Figure 4.1 Unit cell including the 3-D PEC object in a skew 2-D lattice.

Figure 4.1 shows the unit cell including the 3-D PEC object in a skew 2-D lattice. $\mathbf{a_1}$ and $\mathbf{a_2}$ are the primitive lattice vectors in the xy-plane. Without loss of generality, let $(\mathbf{a}_1 \times \mathbf{a}_2) \cdot \hat{z} > 0$. $\mathbf{E}^{inc} = (\hat{\theta}\cos\alpha + \hat{\phi}\sin\alpha)E_0\text{exp}(-j\beta\hat{k}\cdot\mathbf{r})$ is the incident electric field. α is the polarization angle. $\hat{k} = -(\hat{x}\sin\theta^i\cos\phi^i + \hat{y}\sin\theta^i\sin\phi^i + \hat{z}\cos\theta^i)$ and $\beta = \omega\sqrt{\mu\epsilon}$. The incident plane wave of θ-polarization ($\alpha = 0^{\text{o}}$) and ϕ-polarization ($\alpha = 90^{\text{o}}$) are the **0**th-order TMz and TEz Floquet's modes, respectively. Here, TMz (TEz) indicates the magnetic (electric) field transverse to z-direction.

4.1.1 Basis and testing functions and EFIE matrix equation

The EFIE is based on the boundary condition that the total tangential electric field on the PEC objects is zero. It is expressed as [77]-[78]

$$j\omega\mu\left[\int[\mathbf{J_s}(\mathbf{r}')+\frac{1}{\beta^2}\nabla'\cdot\mathbf{J_s}(\mathbf{r}')\nabla]G_p(\mathbf{r},\mathbf{r}')ds'\right]_t=\mathbf{E}_t^{inc} \tag{4.1}$$

where G_p is a doubly periodic Green's function. The basis functions on triangular elements are employed to discretize the electric current. After using the method of moments (MoM), one can obtain the current on the PEC object in one unit cell. Then, the current in the other unit cells can be found by using the Floquet's theorem. The PEC surface is discretized into triangular elements. As shown in Fig. 4.2, there are three types of edges on triangular elements: (1). inside the domain enclosed by the periodic boundary; (2). on periodic boundary C_1 and C_2; (3). on periodic boundary C_3 and C_4. For the first type of edges, the RWG basis functions [47] are adopted to be both basis functions and testing functions

$$\mathbf{B}_{(1)}=\begin{cases}\boldsymbol{\rho}_1^+\frac{l_1}{2A_1^+}, & \mathbf{r}\in E_1^+\\ \boldsymbol{\rho}_1^-\frac{l_1}{2A_1^-}, & \mathbf{r}\in E_1^-\end{cases}, \quad \mathbf{T}_{(1)}=\mathbf{B}_{(1)} \tag{4.2}$$

where $\boldsymbol{\rho}_1^+=\mathbf{r}-\mathbf{r}_1^+$ and $\boldsymbol{\rho}_1^-=\mathbf{r}_1^--\mathbf{r}$. $\mathbf{r}_1^\pm$ indicate the coordinate of the vertices of the triangles $E_1^\pm$, which are opposite to the common edge. $A_1^\pm$ are the area of the triangles $E_1^\pm$ and l_1 is the length of the common edge. For the first type of edges, the testing function is applied to be the same as the basis function.

For the other two types, it is assumed the edges exist in dual pair. As shown in Fig. 4.2, the edges on C_2 are translated with the displacement $\mathbf{a_1}$ to get its counterpart on C_1. One dual pair of edges are associated with one unknown. The corresponding basis function $\mathbf{B}_{(2)}$ and testing function $\mathbf{T}_{(2)}$ are given by

$$\mathbf{B}_{(2)}=\begin{cases}\boldsymbol{\rho}_2^+\frac{l_2}{2A_2^+}e^{-j\mathbf{k}\cdot\mathbf{a_1}}, & \mathbf{r}\in E_2^+\\ \boldsymbol{\rho}_2^-\frac{l_2}{2A_2^-}, & \mathbf{r}\in E_2^-\end{cases} \tag{4.3}$$

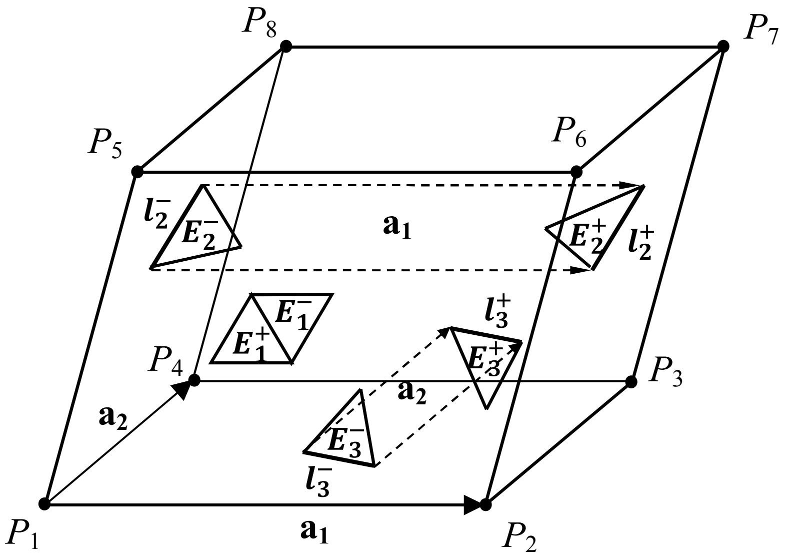

Figure 4.2 Three types of edges on triangular elements. The periodic boundary (PB) C_1 is comprised of P_2, P_3, P_6, and P_7. The PB C_2 is comprised of P_1, P_4, P_5, and P_8. The PB C_3 is comprised of P_3, P_4, P_7, and P_8. The PB C_4 is comprised of P_1, P_2, P_5, and P_6.

$$\mathbf{T}_{(2)} = \begin{cases} \boldsymbol{\rho}_2^+ \frac{l_2}{2A_2^+} e^{j\mathbf{k}\cdot\mathbf{a_1}}, & \mathbf{r} \in E_2^+ \\ \boldsymbol{\rho}_2^- \frac{l_2}{2A_2^-}, & \mathbf{r} \in E_2^- \end{cases} \tag{4.4}$$

Similarly, the edges on C_4 are translated with the displacement $\mathbf{a_2}$ to get its counterpart on C_3. The corresponding basis functions $\mathbf{B}_{(3)}$ and testing basis functions $\mathbf{T}_{(3)}$ are given by

$$\mathbf{B}_{(3)} = \begin{cases} \boldsymbol{\rho}_3^+ \frac{l_3}{2A_3^+} e^{-j\mathbf{k}\cdot\mathbf{a_2}}, & \mathbf{r} \in E_3^+ \\ \boldsymbol{\rho}_3^- \frac{l_3}{2A_3^-}, & \mathbf{r} \in E_3^- \end{cases} \tag{4.5}$$

$$\mathbf{T}_{(3)} = \begin{cases} \boldsymbol{\rho}_3^+ \frac{l_3}{2A_3^+} e^{j\mathbf{k}\cdot\mathbf{a_2}}, & \mathbf{r} \in E_3^+ \\ \boldsymbol{\rho}_3^- \frac{l_3}{2A_3^-}, & \mathbf{r} \in E_3^- \end{cases} \tag{4.6}$$

The definition of $\boldsymbol{\rho}_{2,3}^{\pm}$, $\mathbf{r}_{2,3}^{\pm}$, and $A_{2,3}^{\pm}$ are the same as in (4.2). $l_{2,3}$ is the length of edges $l_{2,3}^{\pm}$.

The special basis functions for the edges on the periodic boundary can guarantee that the outgoing electric current $\mathbf{J}_{sn}$ satisfies the periodic boundary condition $\mathbf{J}_{sn}(\mathbf{r}+\mathbf{r_I}) = \mathbf{J}_{sn}(\mathbf{r})e^{-j\mathbf{k}\cdot\mathbf{r_I}}$. Because the basis function is applied to the edges on the periodic boundary, the condition of zero outgoing current is not enforced on the truncated boundary of PEC any more.

After applying weighted residue method, one obtains the matrix equation

$$[Z_{mn}][I_n] = [V_m] \tag{4.7}$$

where

$$V_m = -\frac{\beta}{j\eta}\int \mathbf{T}_m \cdot \mathbf{E}^{inc} ds, \tag{4.8}$$

$$Z_{mn} = \int_s \int_{s'} [\nabla \cdot \mathbf{T}_m \nabla' \cdot \mathbf{B}_n - \beta^2 \mathbf{T}_m \cdot \mathbf{B}_n] G_p ds' ds \tag{4.9}$$

The derivation of (4.9) is given in Appendix B. It is worth noting that the phase factor of the testing function $\mathbf{T}_{(2)}$ (or $\mathbf{T}_{(3)}$) has a different sign from the basis function $\mathbf{B}_{(2)}$ (or $\mathbf{B}_{(3)}$). Therefore, as given in Appendix B, the line-surface integral is cancelled and the matrix element Z_{mn} involves only the double surface integral. Furthermore, the difference of sign can cancel the phase shift of the testing and basis functions. Thus, the diagonal elements are dominant in the resultant coefficient matrix.

Actually, there are two ways to generate the matrix equation from EFIE for the periodic array. The first way is to apply the RWG basis functions as the basis and testing functions to the whole array. Then, with the help of Floquet's theory or periodic boundary condition (PBC), the resultant infinite matrix equations can be rearranged and reduced to finite matrix equations about the unknowns on one unit cell. In this way, the computational domain should first be defined as more than one unit cell.

The second way, which is proposed in this chapter, is to first restrict the computational domain to be one unit cell. Then, the three types of basis and testing functions are applied to the computational domain in one unit cell. Among them, two types of basis and testing functions are designed for the edges on the periodic boundary. The dimension of the resultant matrix equation is naturally finite. It is worth noting that the PBC is not applied by this approach, rather than guaranteed by the designed basis function.

These two ways may result in the same matrix equation. The difference is that the second way starts from the viewpoint of basis function for the edges on the periodic boundary.

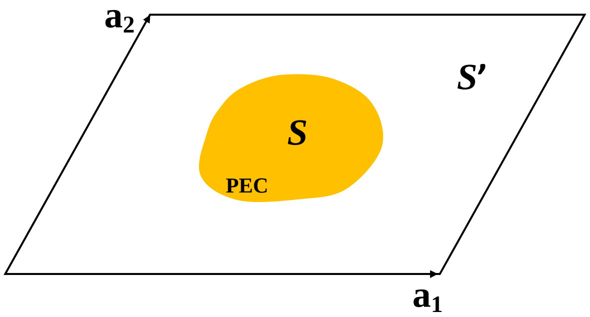

(a) Structure I: one unit cell of the PEC screen

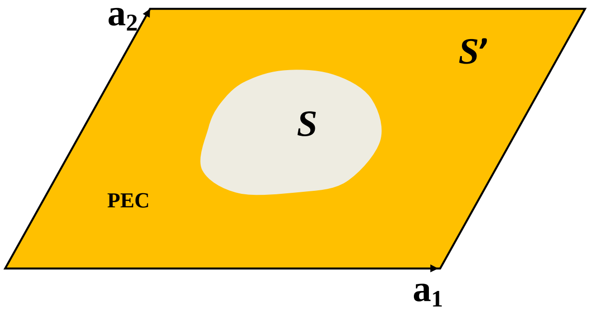

(b) Structure II: complementary structure of (a)

Figure 4.3 One unit cell of the PEC screen and its complementary structure.

4.1.2 Relationship of scattering from the PEC screen with periodicity and its complementary structure

Figure 4.3 shows two planar structures: the one unit cell of the PEC screen and its complementary structure. Here, assume the screens are located at $z = 0$. In Structure I, the PEC parts of the screen are denoted by S, and the apertures in the screen by S'. In Structure II, the apertures are denoted by S, and the PEC parts by S'. Babinet's principle [50] describes the basic relationship of the scattering fields from the PEC screen and its complementary structures. In Appendix B, the proof of this principle is given in a simple way. It involves the integral equations.

For any one of these two structures, there are two ways to calculate the reflection and transmission coefficients. One way is to apply the magnetic field integral equation (MFIE) on the aperture part of the screen. Let S_r denote a unit surface in $z = z_r$ plane at which the reflection coefficient is computed. S_t denotes a unit surface in $z = z_t$ ($z_t \leq z_r$) plane at which the transmission coefficient is calculated.

Assume the incident wave is the $\mathbf{J_0}$th-order Floquet's mode. Its transverse component is given by

$$\mathbf{E}_t^i = b_{\mathbf{J_0}}^i e^{\gamma_{\mathbf{J_0}} z} \sqrt{Z_{\mathbf{J_0}}}\, \mathbf{e}_{t\mathbf{J_0}} \tag{4.10}$$

The details about the Floquet's modes are given in Appendix B.

For the $\mathbf{J}$th-order Floquet's mode, the reflection and transmission coefficients are given by

$$\Gamma_a = -\delta_{\mathbf{J_0 J}} - \frac{1}{2\sqrt{Z_{\mathbf{J}}}\, b_{\mathbf{J_0}}^i} \int_{S_a} e^{\gamma_{\mathbf{J}} z'} \mathbf{h}_{\mathbf{J}}^*(\boldsymbol{\rho}') \cdot \mathbf{M}(\mathbf{r}') ds' \tag{4.11}$$

$$T_a = -\frac{1}{2\sqrt{Z_{\mathbf{J}}}\, b_{\mathbf{J_0}}^i} \int_{S_a} e^{-\gamma_{\mathbf{J}} z'} \mathbf{h}_{\mathbf{J}}^*(\boldsymbol{\rho}') \cdot \mathbf{M}(\mathbf{r}') ds' \tag{4.12}$$

where $\mathbf{M} = 2\mathbf{E} \times \hat{z}$ and S_a denotes the aperture surface in the unit cell. $\delta_{\mathbf{J_0 J}}$ is the Kronecker delta function.

The other way is to apply the EFIE on PEC part of the screen to obtain

$$\Gamma_p = -\frac{\sqrt{Z_{\mathbf{J}}}}{2 b_{\mathbf{J_0}}^i} \int_{S_p} e^{\gamma_{\mathbf{J}} z'} \mathbf{e}_{\mathbf{J}}^*(\boldsymbol{\rho}') \cdot \mathbf{J}(\mathbf{r}') ds' \tag{4.13}$$

$$T_p = \delta_{\mathbf{J_0 J}} - \frac{\sqrt{Z_{\mathbf{J}}}}{2 b_{\mathbf{J_0}}^i} \int_{S_p} e^{-\gamma_{\mathbf{J}} z'} \mathbf{e}_{\mathbf{J}}^*(\boldsymbol{\rho}') \cdot \mathbf{J}(\mathbf{r}') ds' \tag{4.14}$$

Here, S_p denotes the PEC surface in the unit cell. Derivation of (4.11)-(4.14) are given in Appendix B.

If these two approaches are applied to the same periodic structure with the same incident wave, in principle, it should hold that

$$\Gamma_a = \Gamma_p, \quad T_a = T_p \tag{4.15}$$

Now these two approaches are applied to the dual periodic structures. Assume MFIE is applied to Structure I (II) with the TEz incident wave, and EFIE is applied to Structure II (I) with the TMz incident wave. Using the IE approach in Appendix B, it is easy to find

$$\mathbf{M}_{\text{TE}} = \eta \mathbf{J}_{\text{TM}} \tag{4.16}$$

In addition, the following conditions are satisfied

$$\begin{aligned} &\mathbf{h}_{\mathbf{J},\text{TE}} = \mathbf{e}_{\mathbf{J},\text{TM}}, \quad b_{\mathbf{0},\text{TE}}^i = -b_{\mathbf{0},\text{TM}}^i, \\ &Z_{\mathbf{J},\text{TE}} \cdot Z_{\mathbf{J},\text{TM}} = \eta^2 \end{aligned} \tag{4.17}$$

As a result, the following relationship can be found

$$\Gamma_a^{\mathrm{TE}} = -\delta_{\mathbf{J_0 J}} - \Gamma_p^{\mathrm{TM}} \tag{4.18}$$

$$T_a^{\mathrm{TE}} = \delta_{\mathbf{J_0 J}} - T_p^{\mathrm{TM}} \tag{4.19}$$

Assume MFIE is applied to Structure I (II) with the TMz incident wave, and EFIE is applied to Structure II (I) with the TEz incident wave. In a similar manner, one can find

$$\Gamma_a^{\mathrm{TM}} = -\delta_{\mathbf{J_0 J}} - \Gamma_p^{\mathrm{TE}} \tag{4.20}$$

$$T_a^{\mathrm{TM}} = \delta_{\mathbf{J_0 J}} - T_p^{\mathrm{TE}} \tag{4.21}$$

because the following conditions are satisfied

$$\begin{gathered} \mathbf{M}_{\mathrm{TM}} = -\eta \mathbf{J}_{\mathrm{TE}}, \\ \mathbf{h}_{\mathbf{J},\mathrm{TM}} = -\,\mathbf{e}_{\mathbf{J},\mathrm{TE}}, \quad b^i_{\mathbf{0},\mathrm{TM}} = -b^i_{\mathbf{0},\mathrm{TE}} \end{gathered} \tag{4.22}$$

In conclusion, the relationship for the reflection and transmission coefficients between the PEC screen and its complementary structure can be given by

$$\Gamma_a^{\mathrm{TE(TM)}} = -\delta_{\mathbf{J_0 J}} - \Gamma_p^{\mathrm{TM(TE)}} \tag{4.23}$$

$$T_a^{\mathrm{TE(TM)}} = \delta_{\mathbf{J_0 J}} - T_p^{\mathrm{TM(TE)}} \tag{4.24}$$

By using the above relationship, the problem for seeking MFIE solution is transformed to that of the EFIE.

4.1.3 Application of the PGF

Let $\mathbf{u} = \mathbf{r} - \mathbf{r}'$. $G_p(\mathbf{u})$ can be efficiently evaluated by application of the following acceleration technique discussed in [40]. When $|u_z = z - z'| > 0.5\sqrt{\Omega}$,

$$G_p(\mathbf{u}) = \frac{1}{\Omega} \sum_{\mathbf{J}} \frac{e^{-\gamma_{\mathbf{J}}|u_z|}}{2\gamma_{\mathbf{J}}} e^{-j\mathbf{k}_{\mathbf{J}\parallel}\cdot\mathbf{u}} \tag{4.25}$$

where

$$\boldsymbol{\kappa}_{\mathbf{J}\parallel} = j_1\mathbf{b}_1 + j_2\mathbf{b}_2, \;\; \mathbf{k}_{\mathbf{J}\parallel} = \boldsymbol{\kappa}_{\mathbf{J}\parallel} + \mathbf{k}_{\parallel}, \;\; \Omega = |\mathbf{a}_1 \times \mathbf{a}_2|,$$

$$\mathbf{b}_1 = \frac{2\pi}{\Omega}\mathbf{a}_2 \times \hat{z}, \;\; \mathbf{b}_2 = \frac{2\pi}{\Omega}\hat{z} \times \mathbf{a}_1, \;\; \gamma_{\mathbf{J}} = \sqrt{|\mathbf{k}_{\mathbf{J}\parallel}|^{\mathbf{2}} - \beta^{\mathbf{2}}}, \text{ and } \mathbf{J} = (j_1, j_2).$$

The above expression is the spectral representation of the PGF, which is with the exponential convergence.

When $|u_z| \leq 0.5\sqrt{\Omega}$,

$$G_p(\mathbf{u}) = \Phi_{ps} + \Phi_{pf} - \Gamma_{\Phi} \tag{4.26}$$

where Φ_{ps}, Φ_{pf}, and Γ_{Φ} are given as follows. Φ_{pf} and Γ_{Φ} are modified from [40] to facilitate the numerical implementation.

$$\Gamma_{\Phi}(\mathbf{u}) = \frac{1}{\Omega} \sum_{\mathbf{J}} \frac{e^{-j\mathbf{k}_{\mathbf{J}\|}\cdot\mathbf{u}}}{2\gamma_{\mathbf{J}}} \frac{\sum_{\pm} e^{-\gamma_{\mathbf{J}}(\sqrt{\Omega}\pm u_z)}}{1 - e^{-\gamma_{\mathbf{J}}\sqrt{\Omega}}} \tag{4.27}$$

$$\Phi_{ps}(\mathbf{u}) = \sum_{\mathbf{I}} e^{-j\mathbf{k}_{\|}\cdot\mathbf{r}_{\mathbf{I}}} \frac{\cos(\beta R_{\mathbf{I}})}{4\pi R_{\mathbf{I}}} [1 - \operatorname{erf}(ER_{\mathbf{I}})] \tag{4.28}$$

$$\Phi_{pf}(\mathbf{u}) = \frac{1}{2V} \sum_{\mathbf{I}} \frac{e^{-j\mathbf{u}\cdot\mathbf{k}_{\mathbf{I}}}}{|\mathbf{k}_{\mathbf{I}}|^2 - \beta^2} \cdot \left[\beta e^{-(|\mathbf{k}_{\mathbf{I}}|-\beta)^2/(2E)^2} \frac{1 - e^{-|\mathbf{k}_{\mathbf{I}}|\beta/E^2}}{|\mathbf{k}_{\mathbf{I}}|} + \sum_{\pm} e^{-(|\mathbf{k}_{\mathbf{I}}|\pm\beta)^2/(2E)^2} \right] \tag{4.29}$$

where

$$\mathbf{a}_3 = \hat{z}\sqrt{\Omega}, \quad \mathbf{b_3} = \frac{2\pi}{V}\mathbf{a}_1 \times \mathbf{a}_2, \quad V = \mathbf{a_3} \cdot (\mathbf{a}_1 \times \mathbf{a}_2),$$

$$\boldsymbol{\kappa}_{\mathbf{I}} = i_1\mathbf{b_1} + i_2\mathbf{b}_2 + i_3\mathbf{b}_3, \ \mathbf{k}_{\mathbf{I}} = \boldsymbol{\kappa}_{\mathbf{I}} + \mathbf{k}_{\|}, \ E = \sqrt{\pi}/V^{1/3},$$

$$\mathbf{r}_{\mathbf{I}} = i_1\mathbf{a_1} + i_2\mathbf{a_2} + i_3\mathbf{a_3}, \ R_{\mathbf{I}} = |\mathbf{u} - \mathbf{r}_{\mathbf{I}}|, \text{ and } \mathbf{I} = (\mathrm{i}_1, \mathrm{i}_2, \mathrm{i}_3).$$

In [40], $\Gamma_{\Phi}(\mathbf{u})$ involves the calculation of $e^{\sqrt{\Omega}\gamma_{\mathbf{J}}}$ or $e^{u_z\gamma_{\mathbf{J}}}$. In order to achieve the specified accuracy for Γ_{Φ}, the number of terms of the summation is generally large. As a result, $e^{\sqrt{\Omega}\gamma_{\mathbf{J}}}$ or $e^{u_z\gamma_{\mathbf{J}}}$ often may be beyond the range of floating point numbers. To avoid this situation, the expression for $\Gamma_{\Phi}(\mathbf{u})$ is modified to the present form (4.27).

It is obvious that the limit exists for Φ_{pf} when $|\mathbf{k}_{\mathbf{I}}|\beta/E^2$ approaches to zero. If the plane wave is normally incident, $\mathbf{k}_{\mathbf{I}} = \mathbf{0}$ at $\mathbf{I} = \mathbf{0}$. There is no trouble to calculate Φ_{pf} for this case using (4.29).

It should be noted that unlike the free-space Green's function, the periodic Green's function has the singular points in both spatial and spectral domains. When $\mathbf{u} = 0$ and $|\mathbf{k}_{\mathbf{I}}| - \beta = 0$, the PGF encounter the singularity in Φ_{ps} and Φ_{pf}, respectively. In the case of $\mathbf{u} = 0$, one has to deal with the singularity [79]-[82] when evaluating the matrix elements obtained from the MoM method.

4.2 Numerical results

The EFIE approach on PEC is implemented using Fortran language. The evaluation of matrix elements is time-consuming because of the frequent direct calculation of the PGF. To improve the efficiency of this approach, the interpolation technique is applied to the tabulated PGF. Since the PGF is with singularity, the quasi-PGF without the term carrying the singularity is first calculated on uniform grids. Then the quasi-PGF needed to compute is obtained from the table using the second or third-order polynomial interpolation in two or three dimension. Finally, the corresponding PGF is obtained by adding up the term with singularity to the quasi-PGF. To validate the present approach, the reflection and transmission coefficients of several structures are calculated.

The first example is the infinite PEC plate. The PEC plate is infinitely thin. The 2-D lattice has $\mathbf{a_1} = \hat{x}2$ cm and $\mathbf{a_2} = \hat{x}1 + \hat{y}\sqrt{3}/3$ cm. Assume the geometrical center of the unit cell is at the origin. The PEC plate is located at $z = 0$.

The incident plane wave has the incident angles $\theta^i = 60^{\mathrm{o}}$ and $\phi^i = 0^{\mathrm{o}}$. The incident electric field is along y-direction. As shown in Appendix B, this incident plane wave is the $\mathbf{0}$th TEz Floquet's mode. The special testing and basis function on PB are applied to this example. The total numbers of edges and unknowns are 630 and 600, respectively. The Fortran program is run on a PC machine with a 3.2 GHz Pentium IV processor. The CPU time is about 2.99 s per frequency point. This array of PEC plate is essentially the infinite PEC plate. Thus, the induced normalized electric current should be exactly $\bar{\mathbf{J}} = \eta \mathbf{J_s} = \hat{y} E_0 e^{j\frac{\sqrt{3}}{2}\beta x}$. Figure 4.4 shows the normalized current distribution at 9 GHz. In Figure 4.4(a), the current varies with x along the line at $y_0 = 0.192$ mm. In Figure 4.4(b), the current varies with y along the line at $x_0 = -4.33$ mm. As shown in this figure, there are good agreements between the numerical results and exact solution. Figure 4.5 shows the reflection coefficient of the $\mathbf{0}$th-order TEz Floquet's mode for this array. The exact solution of reflection coefficient is $\Gamma = -1$. If the testing and basis functions (4.3)-(4.6) are applied to the edges on the PB, there are excellent agreements between the numerical results and the exact solution. However, if there is no testing and basis functions assigned to the edges on PB, the reflection coefficient is totally wrong.

The second example is the same as the first one, except for a rectangular aperture perforated in the PEC plate. The rectangular aperture has the width $l_x = 1.2$ cm and height $l_y = 0.12$ cm. Its geometrical

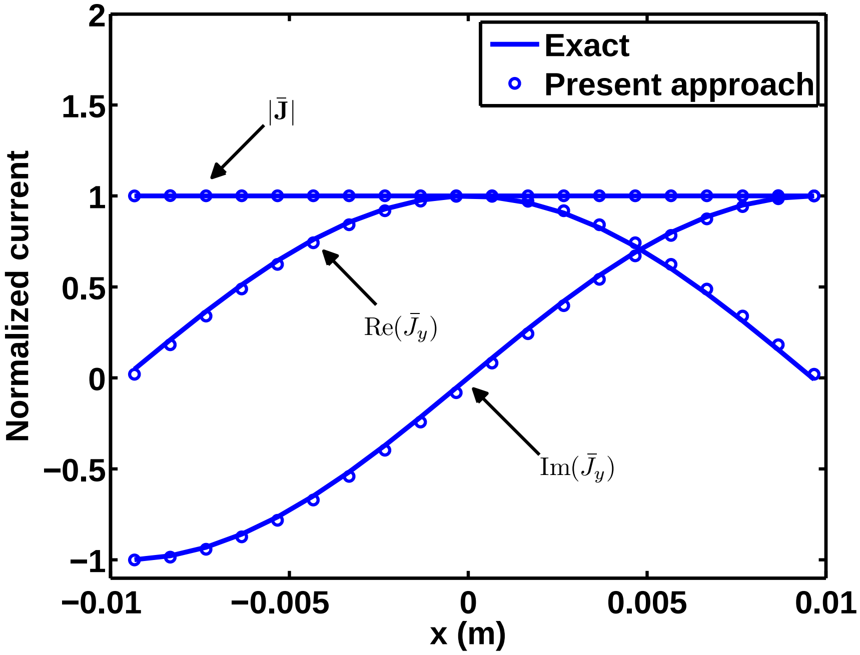

(a) Along x-direction

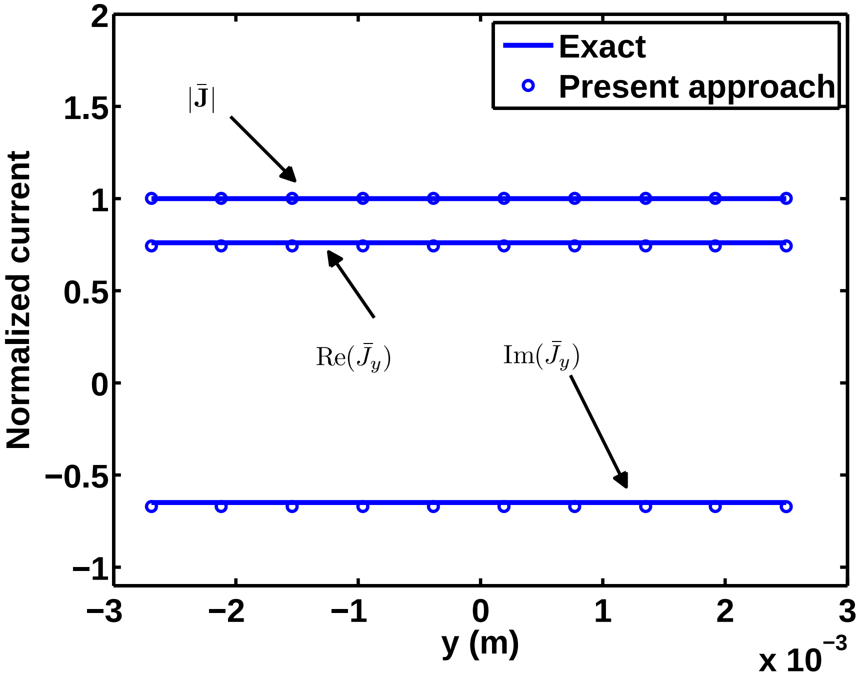

(b) Along y-direction

Figure 4.4 Normalized current distribution at $f = 9$ GHz. $\mathbf{a_1} = \hat{x}2$ cm and $\mathbf{a_2} = \hat{x}1 + \hat{y}\sqrt{3}/3$ cm. $\theta^i = 60^\circ$ and $\phi^i = 0^\circ$.

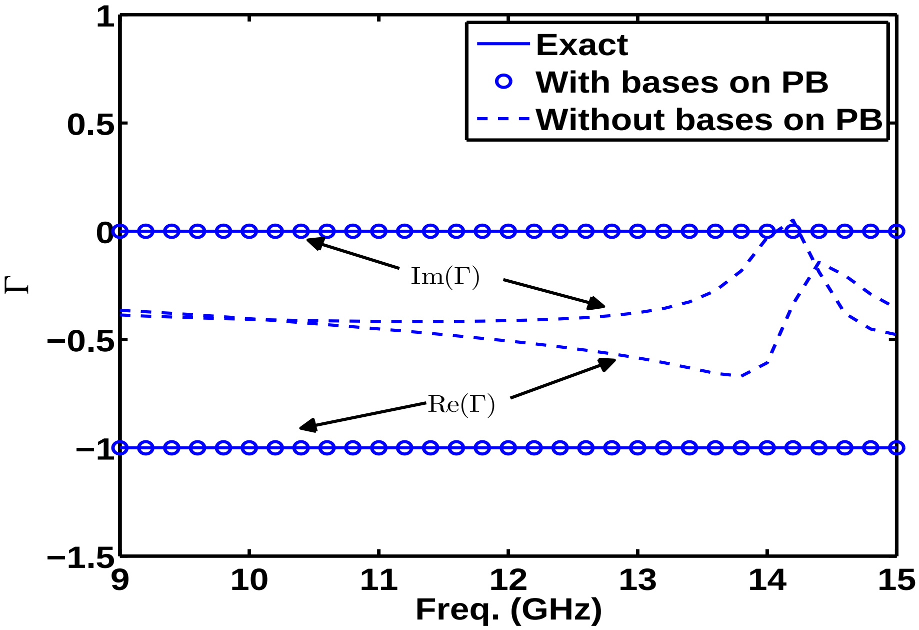

Figure 4.5 Reflection coefficient of the 0th-order TEz mode for the infinite PEC plate. $\mathbf{a_1} = \hat{x}2$ cm and $\mathbf{a_2} = \hat{x}1 + \hat{y}\sqrt{3}/3$ cm. $\theta^i = 60^o$ and $\phi^i = 0^o$

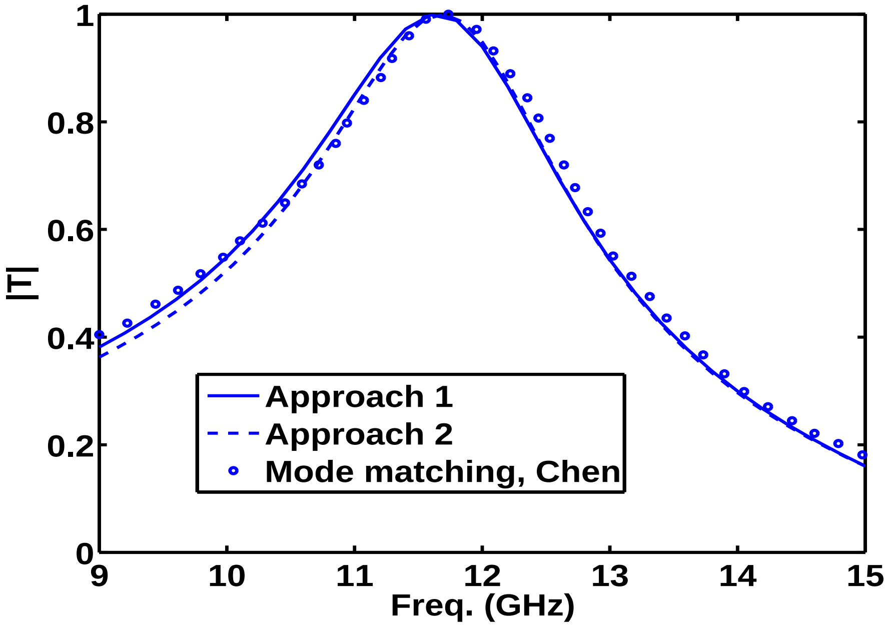

Figure 4.6 Transmission coefficient of the 0th-order TEz Floquet's mode for the doubly periodic array of rectangular apertures. $\mathbf{a_1} = \hat{x}2$ cm and $\mathbf{a_2} = \hat{x}1 + \hat{y}\sqrt{3}/3$ cm. The rectangular aperture has the width $l_x = 1.2$ cm and height $l_y = 0.12$ cm. $\theta^i = 60^o$ and $\phi^i = 0^o$. The circle indicates the results taken from [22].

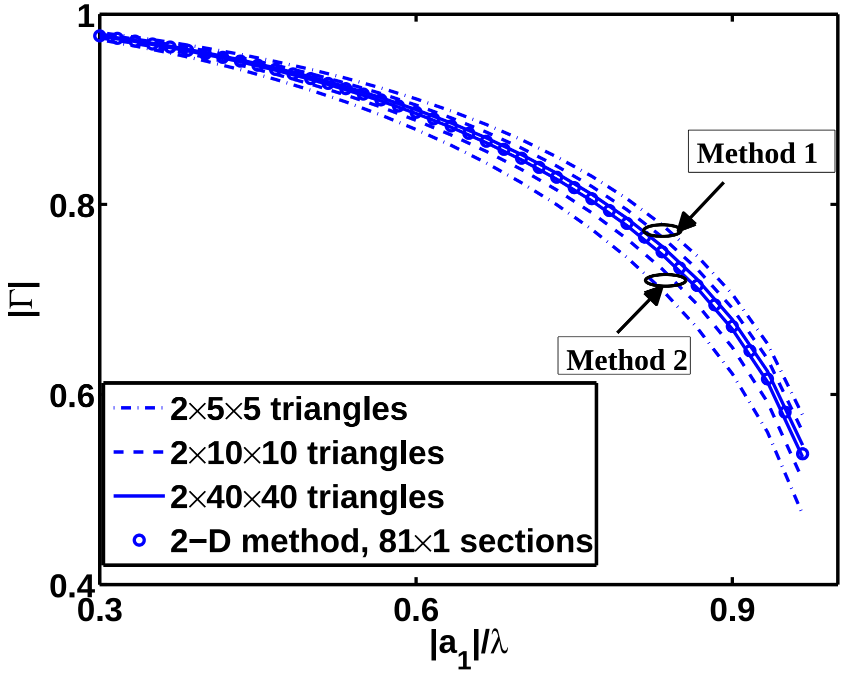

(a)

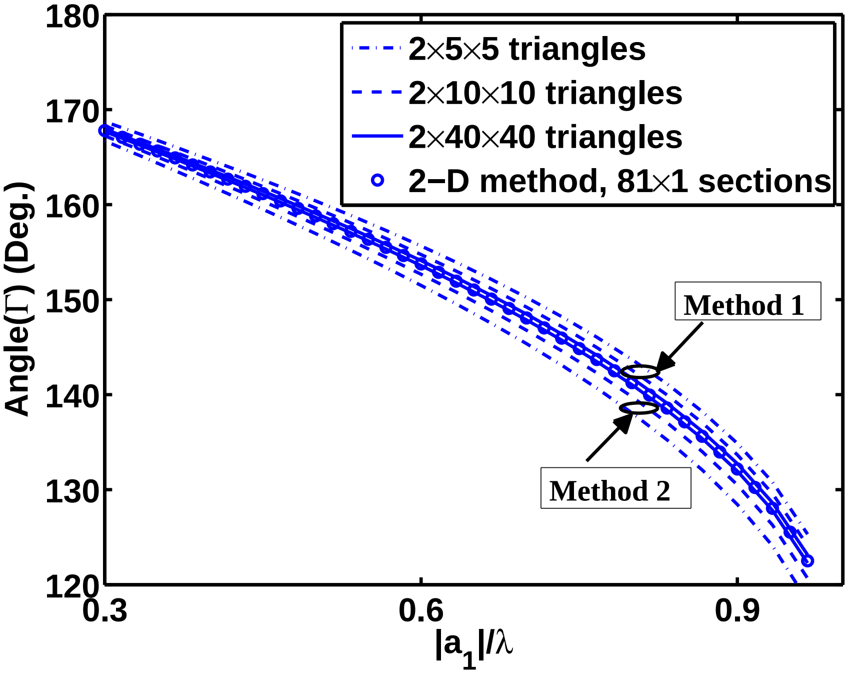

(b)

Figure 4.7 Reflection coefficient of the 0th-order TEz mode for the PEC strip. $\mathbf{a_1} = \hat{x}1$ m and $\mathbf{a_2} = \hat{y}0.5$ m. The rectangular PEC plate has the width $l_x = 0.5$ m and height $l_y = 0.5$ m. $\theta^i = 0^\circ$ and $\phi^i = 0^\circ$.

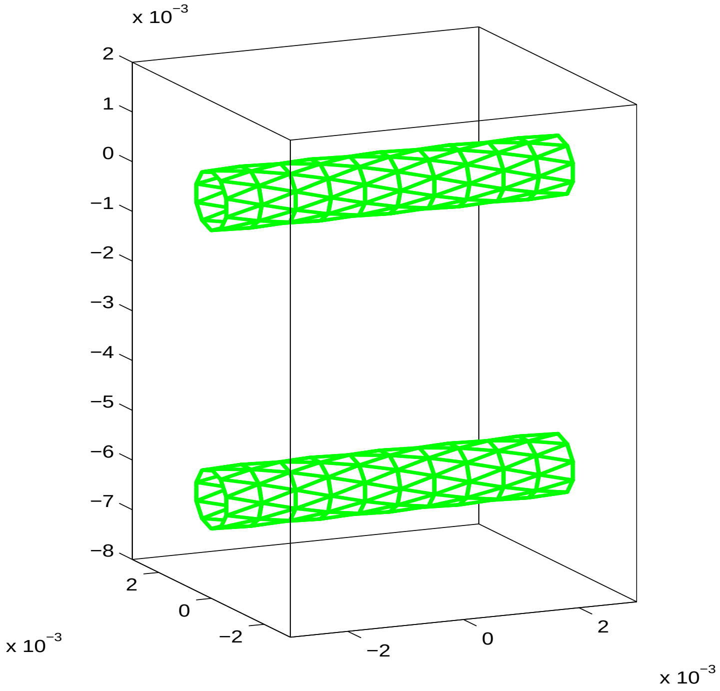

Figure 4.8 Two meshed cylinders in a unit cell. $\mathbf{a_1} = \hat{x}6$ mm and $\mathbf{a_2} = \hat{y}6$ mm. Each cylinder has the radius $r = 0.6$ mm and length $L = 6$ mm. The space between two cylinders is $d = 6$ mm.

center is also located at the origin. The transmission coefficient is computed by using two approaches. When directly using (4.14), i.e., EFIE on the PEC part, the special testing and basis functions for the edge on PB is applied. The number of unknowns is 3601. The CPU time is about 377 s for each frequency point. When using (4.24), the EFIE is first applied to calculate the transmission coefficient for the complementary structure. Because the PEC plate in its complementary structure is inside the unit cell, the special testing and basis functions for the edge on PB are not applied. For the second approach, the number of unknowns is 237. The CPU time is about 2.36 s for each frequency point. Figure 4.6 shows the transmission coefficient of the **0**th-order TEz Floquet's mode for this array. Good agreements are observed between the results of three approaches. It is worth noting that the first approach demands much more dense mesh to achieve the converged results than the second one. This is due to the singular current distribution near the edge of the plate. Thus, the second approach is suggested for the periodic array of apertures.

In the third example, the PEC strip is simulated to demonstrate the convergence of reflection coefficients. The strip is infinite long along y-direction. $\mathbf{a_1} = \hat{x}1$ m and $\mathbf{a_2} = \hat{y}0.5$ m. In one unit cell, the

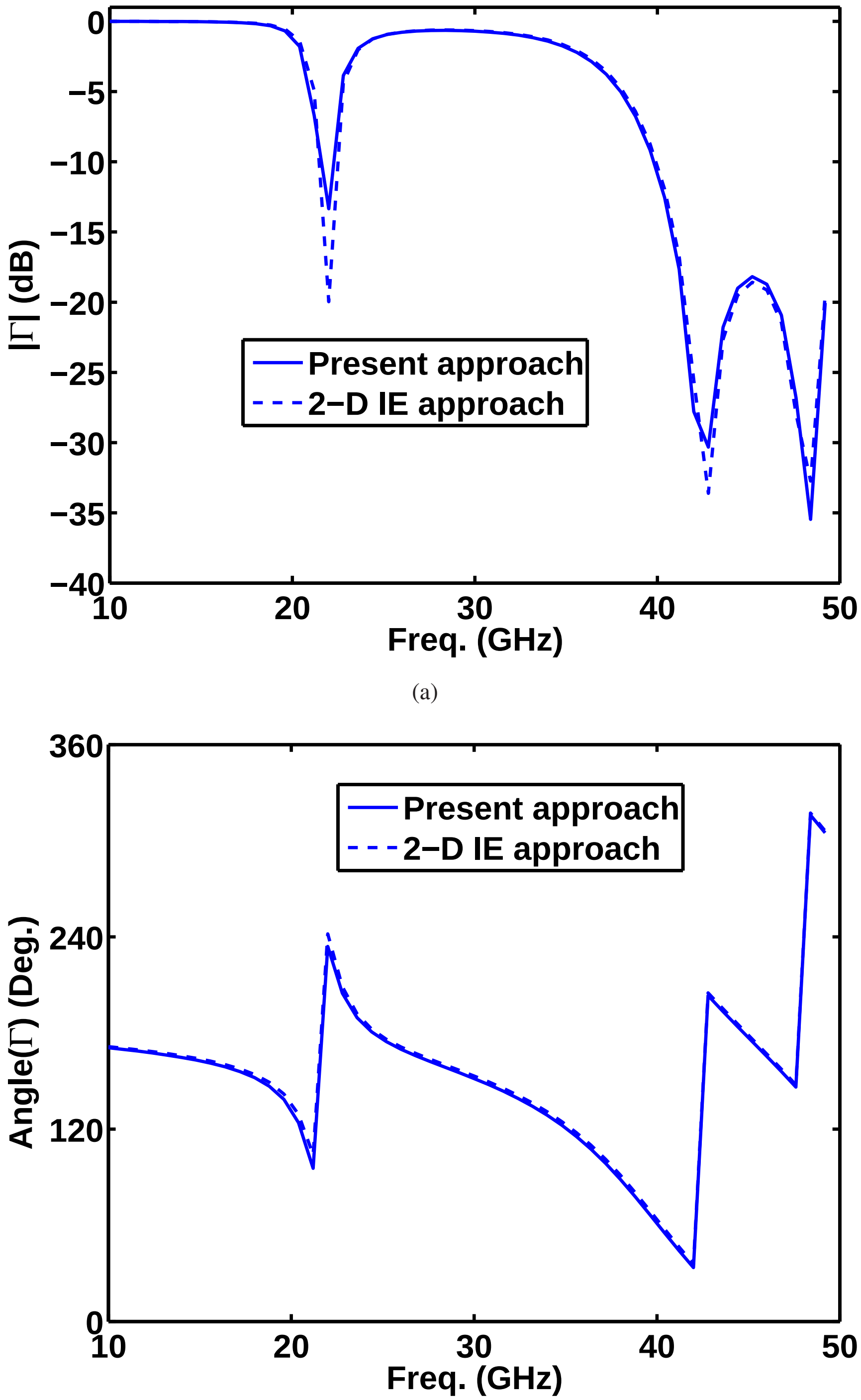

(a)

(b)

Figure 4.9 Reflection coefficient of the 0th-order TMz mode for the two-layer array of PEC cylinders shown in Fig. 4.8. $\theta^i = 0^o$ and $\phi^i = 0^o$.

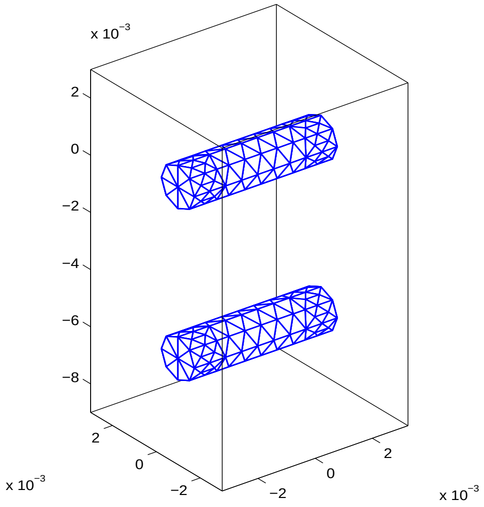

Figure 4.10 Two meshed cylinders in a unit cell. $\mathbf{a_1} = \hat{x}6$ mm and $\mathbf{a_2} = \hat{y}6.5$ mm. Each cylinder has the radius $r = 0.75$ mm and length $L = 5$ mm. The space between two cylinders is $d = 6$ mm.

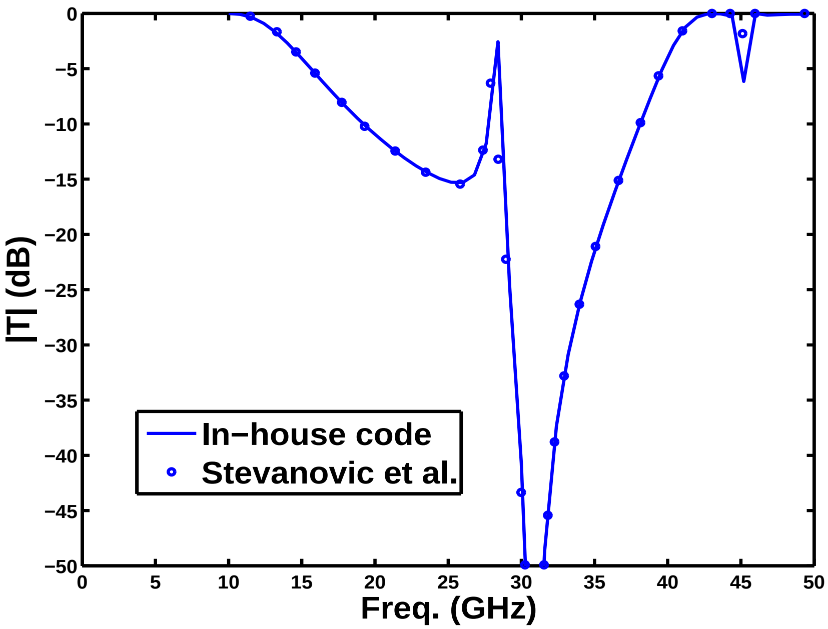

Figure 4.11 Transmission coefficient of the 0th-order TMz mode for the two-layer array of PEC cylinders shown in Fig. 4.10. $\theta^i = 0^o$ and $\phi^i = 0^o$. The circle indicates the results taken from [33].

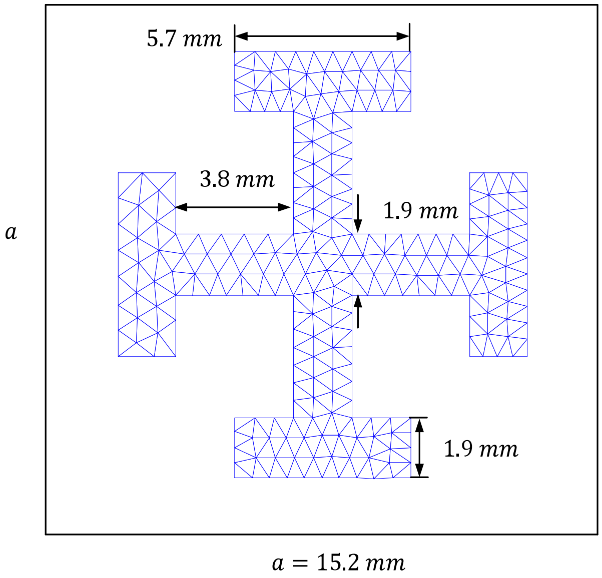

Figure 4.12 Geometry of the Jerusalem cross in a unit cell. $\mathbf{a_1} = \hat{x}15.2$ mm and $\mathbf{a_2} = \hat{y}15.2$ mm.

PEC plate has the width $l_x = 0.5$ m and height $l_y = 0.5$ m. The geometrical centers of the unit cell and the PEC plate coincide with each other. The top and bottom sides involve testing and basis functions for the edges on PB. The left and right sides are not associated with the unknowns. The incident plane wave has the incident angles $\theta^i = 0^o$ and $\phi^i = 0^o$. The incident electric field is along y-direction. For this case, the 3-D problem can be reduced to the 2-D problem. Then the 2-D IE approach can be used to calculate the reflection coefficient [67], [84]. Figure 4.7 shows the convergence of the reflection coefficient of the 0th-order TEz mode. As shown in this figure, the dense mesh is required to achieve the convergence. This is due to the edge effect of PEC.

The fourth example is the doubly periodic array of two PEC cylinders. Figure 4.8 shows one unit cell including the meshed cylinders. The axis of each cylinder is along x-direction. $\mathbf{a_1} = \hat{x}6$ mm and $\mathbf{a_2} = \hat{y}6$ mm. Each cylinder has the radius $r = 0.6$ mm and length $L = 6$ mm. The space between two cylinders is $d = 6$ mm. Two cross sections of each cylinder touch two sides of the periodic boundary. Thus, these two sides involve the testing and basis functions for the edges on PB. The total number of unknowns is 600. The average CPU time is about 3.9 s per frequency point. The reflection coefficients are shown in Figure 4.9. As shown in this figure, there are good agreements between the results of the present approach and 2-D IE approach except at some dips. The discrepancy is due to the different

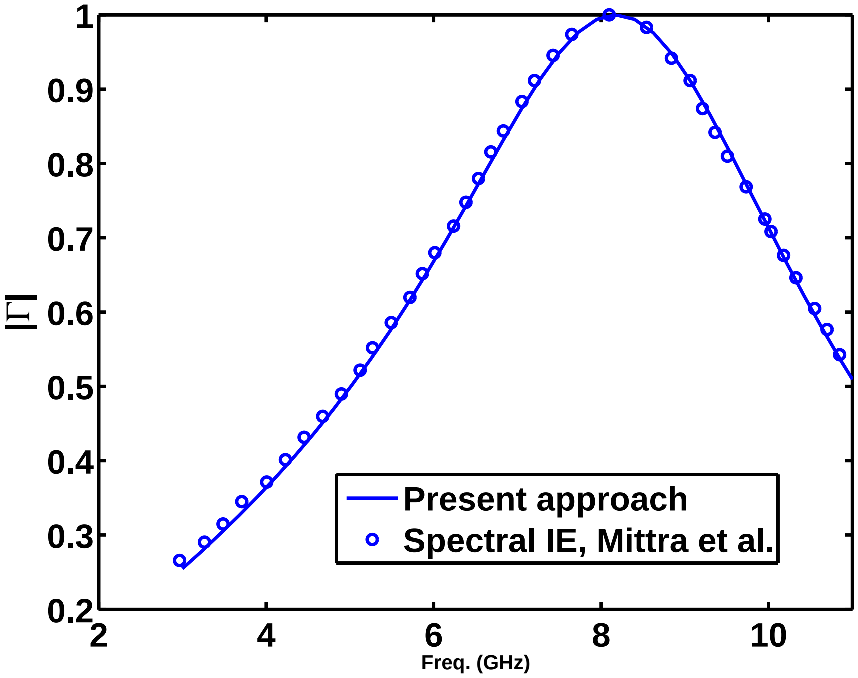

(a)

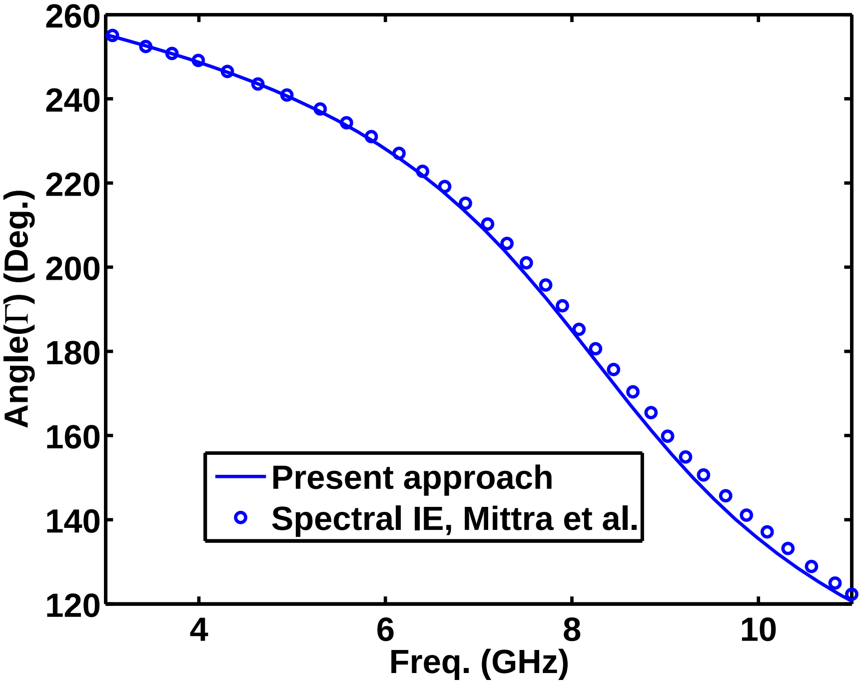

(b)

Figure 4.13 Reflection coefficient of the 0th-order TMz mode for the doubly periodic array of PEC Jerusalem cross. $\theta^i = 0^\circ$ and $\phi^i = 0^\circ$. The circle indicates the results taken from [9].

mesh type and density for two approaches.

The fifth example is still the doubly periodic array of two PEC cylinders. Unlike the fourth example, the cylinders are not truncated by the PB. Thus, the mesh is distributed on the closed surface of the cylinders as shown in Fig. 4.10. The axis of each cylinder is along x-direction. $\mathbf{a_1} = \hat{x}6$ mm and $\mathbf{a_2} = \hat{y}6.5$ mm. Each cylinder has the radius $r = 0.75$ mm and length $L = 5$ mm. The space between two cylinders is $d = 6$ mm. The number of unknowns is 696. No special testing and basis functions on the PB are applied since the PEC surface is located inside the unit cell. The average CPU time is about 6.9 s per frequency point. Figure 4.11 shows the transmission coefficients of this array. The numerical results are compared with those from the approach in [33]. The difference between two approaches is the application of different forms of PGF. In [33], the Ewald transformation [38] is applied to speed up the convergence of PGF.

The last example is the doubly periodic array of the Jerusalem cross. Figure 4.12 shows the geometry of the Jerusalem cross. The number of unknowns is 502. Similar to the above example, there are no special testing and basis functions on the PB to be applied. The average CPU time is about 2.2 s per frequency point. The reflection coefficient of the $\mathbf{0}$th-order TMz mode is illustrated in Fig. 4.13.

CHAPTER 5 ERROR IN PROJECTION OF PLANE WAVES USING VARIOUS BASIS FUNCTIONS

In this chapter, the projection error of various basis functions is investigated. The equivalent current is expanded by various basis functions. Then application of the weighted residual method will yield the unknown coefficients of basis functions. After obtaining the coefficients, the projection error can be found. The root mean square (RMS) error of current is used as the error measure since the current is integrable. The numerical projection error of the triangular basis, the basis of their higher-order version, and the divergence-conforming basis on rectangular and triangular elements are shown. Furthermore, the closed forms of the projection error on the infinite meshes are derived. The basis functions involved are pulse basis, triangular basis, the second-order basis in 1D case, the divergence-conforming basis on rectangular elements and the one-directional triangular elements in 2D case. It is found that the projection error of p-th order 1D basis is asymptotically inversely proportional to $(p+1)$-th power of the density of unknowns. Based on the closed-form projection errors in 1D case, it is found when the expansion basis is fixed, the application of different testing functions only affect the coefficient of the projection error rather than the order. In addition, the error of divergence-conforming basis in projection of curl-free vectors is generally less than that of divergence-free vectors. This is expected since both the divergence-conforming basis and the expanded vector are with the same property, namely, curl-free.

5.1 Projection error in the 1-D case

In 1-D case, the plane wave is simply expressed as

$$J(x) = \exp(jkx) \tag{5.1}$$

The infinite mesh consists of the uniform linear elements with equally spaced nodes. The spacing between two adjacent nodes is h. The current in (5.1) is projected into an approximated space

$$\tilde{J}(x) = \sum_n a_n N_n(x) \tag{5.2}$$

where $N_n(x)$ is the expansion basis function, and a_n is the corresponding coefficient. Using the weighted residual method, we obtain

$$\sum_n a_n \int_{x_{m1}}^{x_{m2}} N_n(x) T_m(x) dx = \int_{x_{m1}}^{x_{m2}} J(x) T_m(x) dx \tag{5.3}$$

where $T_m(x)$ is the testing function defined at $[x_{m1}, x_{m2}]$.

5.1.1 Projection error of lower-order basis functions

Consider the case that the expansion and testing functions are both triangular basis functions. From (5.3),

$$a_{m-1} + 4a_m + a_{m+1} = 6\exp(jmkh)\mathrm{sinc}^2(kh/2) \tag{5.4}$$

where $\mathrm{sinc}\, x = \sin x\, / x$. Since the plane wave propagates along the uniform mesh, the phase difference between a_{m+1} and a_m should be $\Delta\theta = kh$. Thus, it can be assumed

$$a_m = d_0 \exp(jmkh) \tag{5.5}$$

where d_0 is the coefficient to be solved. Substitution of (5.5) into (5.4) yields

$$d_0 = \frac{3\,\mathrm{sinc}^2(kh/2)}{2 + \cos(kh)} \tag{5.6}$$

The assumption is valid since it makes (5.4) hold on for any value of integer m. At $x \in [x_{m-1}, x_m]$, the error is

$$\mathrm{Err}(x) = |\exp(jkx) - a_m(x - x_{m-1})/h - a_{m-1}(x_m - x)/h| \tag{5.7}$$

The RMS error is obtained by

$$\mathrm{Err}_{\mathrm{RMS}} = \sqrt{\frac{\int_{x_{m-1}}^{x_m} \mathrm{Err}^2(x)dx}{\int_{x_{m-1}}^{x_m} |\exp(jkx)|^2 dx}} \tag{5.8}$$

Evaluating (5.8) with (5.5)-(5.7) yields

$$\mathrm{Err}_{\mathrm{RMS}} = \sqrt{1 - \frac{3\mathrm{sinc}^4(kh/2)}{\cos(kh) + 2}} \tag{5.9}$$

When h is small, one can get the asymptotical expression for the RMS error by using $\cos x \approx 1 - x^2/2! + x^4/4!$ and $\operatorname{sinc} x \approx 1 - x^2/3! + x^4/5!$

$$\mathrm{Err}_{\mathrm{RMS\_ASM}} = \frac{(kh)^2}{12\sqrt{5}} \tag{5.10}$$

Table 5.1 One-dimensional projection error in closed form

Testing function	Expansion function	$\mathrm{Err}_{\mathrm{RMS}}$	$\mathrm{Err}_{\mathrm{RMS\_ASM}}$
Point function	Pulse function	$\sqrt{2(1-\operatorname{sinc}(kh/2))}$	$\frac{kh}{2\sqrt{3}}$
Pulse function	Pulse function	$\sqrt{1-\operatorname{sinc}^2(kh/2)}$	$\frac{kh}{2\sqrt{3}}$
Point function	Triangular function	$\sqrt{2[1-\operatorname{sinc}^2(kh/2)]-\frac{2}{3}\sin^2(kh/2)}$	$\sqrt{\frac{2}{15}\frac{(kh)^2}{4}}$
Triangular function	Triangular function	$\sqrt{1-\frac{3\operatorname{sinc}^4(kh/2)}{\cos(kh)+2}}$	$\frac{(kh)^2}{12\sqrt{5}}$

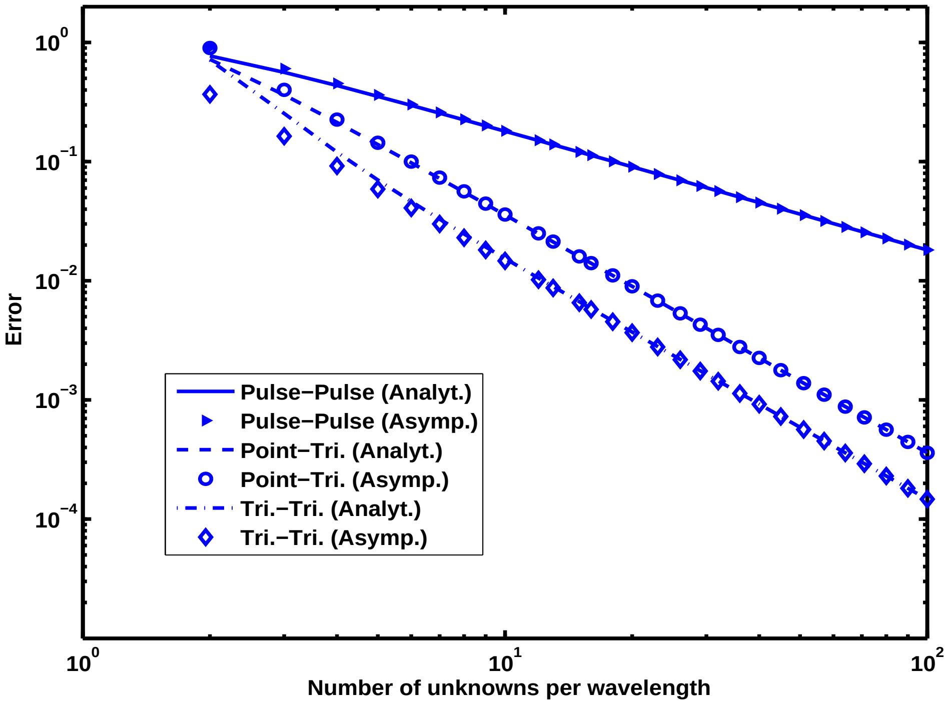

Figure 5.1 Projection error of lower-order basis functions in the 1-D case.

Similarly, the projection error can be obtained for the other cases: expansion function of pulse basis and testing function of point function; expansion and testing function of pulse function; expansion function of triangular basis and testing function of point function. The expressions of the projection error are listed in Table 5.1. As shown in this table, when using the expansion function of pulse function, the error for the testing function of pulse function is very close to that of point function. Thus, there appears to be little or no advantage for Galerkin method [60] for this case. Figure 5.1 plots the projection error in Table 5.1 as a function of number of unknowns per wavelength. It should be mentioned that the error estimate for pulse and triangular basis are different from [56]. It is because the RMS and discrete RMS error are employed in this paper and [56], respectively. The former performs the integration over the mesh while the latter executes the summation of the values at the single point of each element.

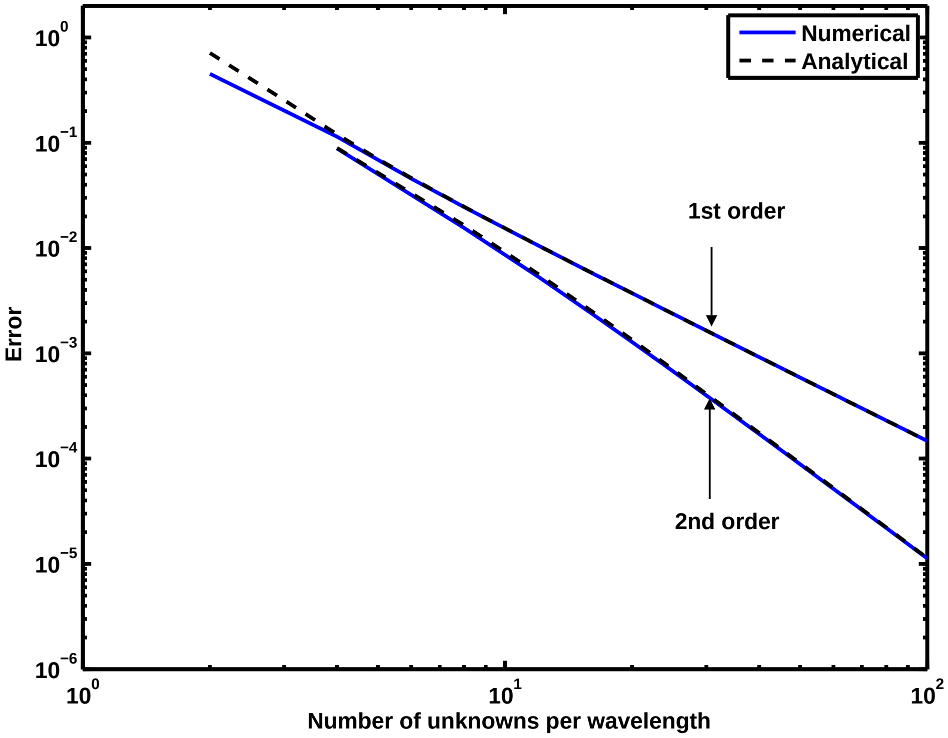

Figure 5.2 Numerical and analytical results for the first and second order basis functions.

5.1.2 Projection error of higher-order basis functions

Using the same approach as above, the RMS projection error is derived for expansion and testing function of second order basis function

$$\begin{aligned} \mathrm{Err}_{\mathrm{RMS}} =&\{[(6t^2-30)\cos^4 t - 30t\sin t\cos^3 t + (33t^2+15+t^6)\cos^2 t \\ &- 30t\sin(2t) - 2t^6 + 15 + 6t^2]/[t^6(-2+\cos^2 t)]\}^{1/2} \end{aligned} \tag{5.11}$$

where $t = kh/2$. The asymptotical RMS error can be obtained by using the Taylor series expansion of $\sin x$ and $\cos x$

$$\mathrm{Err}_{\mathrm{RMS\_ASM}} = \sqrt{\frac{2}{945}}(kh/2)^3 \tag{5.12}$$

It should be noted that the nominator in square root sign of (5.11) is $O(h^{12})$. It is much smaller than 15 in the nominator. Thus, the double or higher precision should be applied for the computer program to accurately calculate the projection error in (5.11).

As shown in the above expressions, the projection errors using the expansion basis of pulse, triangular, and second order basis are asymptotically proportional to 1, 2, and 3 power of the density of unknowns, respectively. When the expansion basis is fixed, the application of different testing functions only affect the constant coefficient of the projection error rather than the order.

Furthermore, the projection error of higher-order 1-D basis function is calculated numerically. For the sake of simplicity, the computational domain is defined within $x \in [0, \lambda]$ and divided into N_e linear elements. For the linear element e with the nodes x_1 and x_2, the coordinate transformation $x = x_1\,\xi_1 + x_2\,\xi_2$ is applied, where $\xi_1 + \xi_2 = 1$. There are $p + 1$ interpolatory basis functions of order p defined on element e

$$N_i(\xi_1, \xi_2) = P_I^p(\xi_1)P_J^p(\xi_2) \tag{5.13}$$

where $I + J = p$, and $P_I^p(\xi)$ is the Silvester polynomial [62]

$$P_I^p(\xi) = \begin{cases} \frac{1}{I!}\prod\limits_{k=0}^{I-1}(p\xi - k), & 1 \le I \le p \\ 1, & I = 0 \end{cases} \tag{5.14}$$

The Galerkin method is used to obtain the coefficient of basis functions. The Gaussian Legendre quadrature is employed to accurately evaluate the 1-D integral. Unlike at the node inside the computational domain, the coefficient at the end node corresponds to only half basis function rather than one basis function. Figure 5.2 shows the analytical and numerical results for first and second order basis. There is a good agreement between the analytical and numerical results except the discrepancy due to the edge effect when $\lambda/h \le 2$. The projection error of the basis from 1st to 5th order is shown in Figure 5.3. As shown in this figure, the projection error of p-th order basis is asymptotically proportional to $(p + 1)$ power of the density of unknowns.

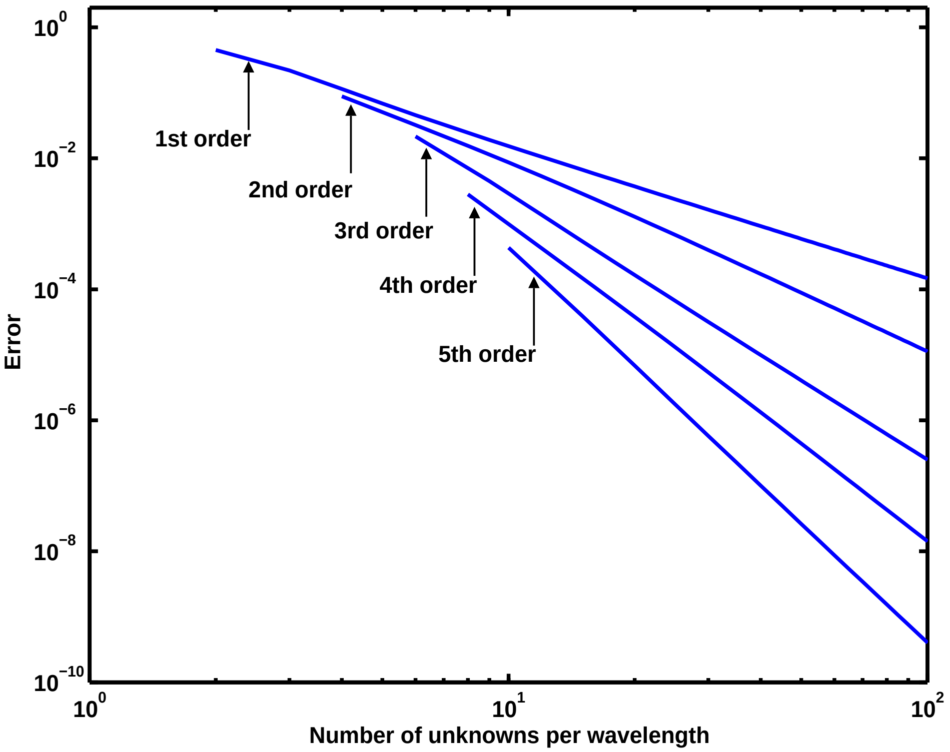

Figure 5.3 Projection error of higher-order basis functions in the 1-D case.

5.2 Projection error in the 2-D case

For a plane wave with incident direction of $\hat{k}$ and polarization direction of $\hat{p}$, the magnetic field on the plane of $z = 0$ is given by

$$\mathbf{H}^{inc} = \hat{k} \times \hat{p}\, H_0 \exp(-jk\hat{k} \cdot \boldsymbol{\rho}) \tag{5.15}$$

where $\hat{k} = -\hat{z}\cos\theta_i + \hat{k}_t \sin\theta_i$, $\hat{k}_t = -(\hat{x}\cos\phi_i + \hat{y}\sin\phi_i)$, $\boldsymbol{\rho} = \hat{x}x + \hat{y}y$, and $\hat{p} = \hat{\theta}\cos\alpha + \hat{\phi}\sin\alpha$. α is the polarization angle. (θ_i, ϕ_i) are the incident angles. The equivalent electric current on the plane of $z = 0$ is

$$\mathbf{J} = \hat{z} \times \mathbf{H}^{inc} = \hat{z} \times (\hat{k} \times \hat{p})\, H_0 \exp(-jk \sin\theta_i\, \hat{k}_t \cdot \boldsymbol{\rho}) \tag{5.16}$$

For the θ-polarization ($\alpha = 0°$),

$$\mathbf{J} = -\hat{k}_t\, H_0 \exp(-jk \sin\theta_i\, \hat{k}_t \cdot \boldsymbol{\rho}) \tag{5.17}$$

For the ϕ polarization ($\alpha = 90°$),

$$\mathbf{J} = \hat{\phi}\cos\theta_i H_0 \exp(-jk \sin\theta_i\, \hat{k}_t \cdot \boldsymbol{\rho}) \tag{5.18}$$

It is obvious that the equivalent vector currents of θ and ϕ polarization are curl- and divergence- free, respectively.

5.2.1 Projection error of basis functions on rectangular elements

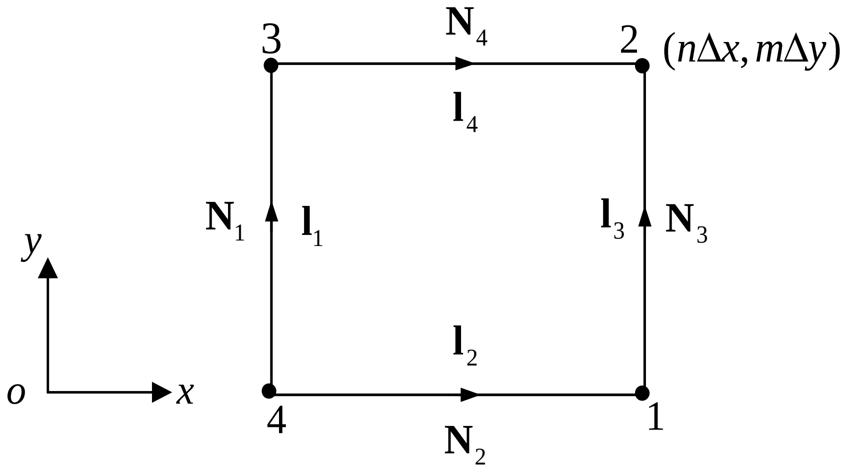

Figure 5.4 Curl-conforming basis functions on a rectangular element.

The rectangular element is shown in Figure 5.4. The rectangular element in xy-plane is transformed into a square element in $\xi_1\xi_2$-plane by the coordinate transformation

$$\mathbf{r} = \mathbf{r}_1\xi_1(1-\xi_2) + \mathbf{r}_2\xi_1\xi_2 + \mathbf{r}_3(1-\xi_1)\xi_2 + \mathbf{r}_4(1-\xi_1)(1-\xi_2) \tag{5.19}$$

The curl-conforming basis functions are expressed by

$$\begin{aligned} \mathbf{N}_1 &= (1-\xi_1)\mathbf{l}_3/l_3 \\ \mathbf{N}_2 &= (1-\xi_2)\mathbf{l}_2/l_2 \\ \mathbf{N}_3 &= \xi_1\mathbf{l}_3/l_3 \\ \mathbf{N}_4 &= \xi_2\mathbf{l}_2/l_2 \end{aligned} \tag{5.20}$$

The divergence-conforming basis functions, which are known as the rooftop basis functions in electromagnetics, are

$$\mathbf{S}_M = \hat{z} \times \mathbf{N}_M \ (M = 1, \cdots, 4) \tag{5.21}$$

Assume the plane wave propagates along the infinite mesh, which is uniform, namely $\Delta x = \Delta y = h$. The coefficients corresponding to basis functions $\mathbf{N}_1$, $\mathbf{N}_2$, $\mathbf{N}_3$, and $\mathbf{N}_4$, are denoted by $a_{m\,n-1}$, $b_{m-1\,n}$,

a_{mn}, and b_{mn}, respectively. On the rectangular element, the equivalent current in (5.17) and (5.18) is approximated using the divergence-conforming basis function

$$\tilde{\mathbf{J}} = a_{m\,n-1}\mathbf{S}_1 + a_{m\,n}\mathbf{S}_3 + b_{m\,n-1}\mathbf{S}_2 + b_{m\,n}\mathbf{S}_4 \tag{5.22}$$

$\mathbf{S}_{1(3)}$ is orthogonal to $\mathbf{S}_{2(4)}$. Thus, using the Galerkin method, one can obtain two sets of equation in which the coefficient a_{mn} is decoupled with b_{mn}

$$a_{m\,n-1} + 4a_{mn} + a_{m\,n+1} = B_1 \tag{5.23a}$$

$$b_{m-1\,n} + 4b_{mn} + b_{m+1\,n} = B_2 \tag{5.23b}$$

where

$$B_1 = 6V_1\frac{\exp(j\beta_2)-1}{j\beta_2}\,\frac{\exp(j2\beta_1)-2\exp(j\beta_1)+1}{(j\beta_1)^2}\exp[j(n-1)\beta_1 + j(m-1)\beta_2]$$

$$B_2 = 6V_2\frac{\exp(j\beta_1)-1}{j\beta_1}\,\frac{\exp(j2\beta_2)-2\exp(j\beta_2)+1}{(j\beta_2)^2}\exp[j(n-1)\beta_1 + j(m-1)\beta_2]$$

$$V_1 = \hat{y}\cdot(\hat{k}\times\hat{p}),\ V_2 = \hat{x}\cdot(\hat{k}\times\hat{p}),\ \beta_1 = kh\sin\theta_i\cos\phi_i,\ \ \beta_2 = kh\sin\theta_i\sin\phi_i.$$

For a plane wave with the non-constant factor of $\exp(jk\sin\theta_i\cos\phi_i\,x + jk\sin\theta_i\sin\phi_i\,y)$, one may assume the coefficients to be with the form

$$a_{mn} = d_1\exp[j(n-1)\beta_1 + j(m-1)\beta_2] \tag{5.24a}$$

$$b_{mn} = d_2\exp[j(n-1)\beta_1 + j(m-1)\beta_2] \tag{5.24b}$$

Substitution of (5.24) into (5.23) yields

$$d_1 = \frac{6V_1}{4+2\cos(\beta_1)}\,\frac{\exp(j\beta_2)-1}{j\beta_2}\,\frac{\exp(j2\beta_1)-2\exp(j\beta_1)+1}{(j\beta_1)^2} \tag{5.25a}$$

$$d_2 = \frac{6V_2}{4+2\cos(\beta_2)}\,\frac{\exp(j\beta_1)-1}{j\beta_1}\,\frac{\exp(j2\beta_2)-2\exp(j\beta_2)+1}{(j\beta_2)^2} \tag{5.25b}$$

Again, the RMS error is obtained by

$$\mathrm{Err}_{\mathrm{RMS}} = \sqrt{\frac{\iint_{\Delta s}|\tilde{\mathbf{J}}-\mathbf{J}|^2 ds}{\iint_{\Delta s}|\mathbf{J}|^2 ds}} \tag{5.26}$$

where Δs indicates the rectangular element shown in Figure 5.4. From (5.26), the RMS error for θ-polarization is

$$\mathrm{Err}_{\mathrm{RMS}} = \sqrt{\frac{3-2(|d_1|^2+|d_2|^2)-(|d_1|^2\cos\beta_1+|d_2|^2\cos\beta_2)}{3}} \tag{5.27}$$

The RMS error for ϕ polarization is

$$\mathrm{Err}_{\mathrm{RMS}} = \sqrt{\frac{3\cos^2\theta_i - 2(|d_1|^2 + |d_2|^2) - (|d_1|^2\cos\beta_1 + |d_2|^2\cos\beta_2)}{3\cos^2\theta_i}} \tag{5.28}$$

Simplifying (5.27) and (5.28), one will obtain

$$\mathrm{Err}_{\mathrm{RMS}} = \sqrt{1 - \frac{3\cos^2\phi_i}{2+\cos\beta_1}\mathrm{sinc}^2(\beta_2/2)\mathrm{sinc}^4(\beta_1/2) - \frac{3\sin^2\phi_i}{2+\cos\beta_2}\mathrm{sinc}^2(\beta_1/2)\mathrm{sinc}^4(\beta_2/2)} \tag{5.29}$$

for θ-polarization, and

$$\mathrm{Err}_{\mathrm{RMS}} = \sqrt{1 - \frac{3\sin^2\phi_i}{2+\cos\beta_1}\mathrm{sinc}^2(\beta_2/2)\mathrm{sinc}^4(\beta_1/2) - \frac{3\cos^2\phi_i}{2+\cos\beta_2}\mathrm{sinc}^2(\beta_1/2)\mathrm{sinc}^4(\beta_2/2)} \tag{5.30}$$

for ϕ polarization.

When $\theta_i = 90^\circ$ and $\phi_i = 0^\circ$, the RMS error will be reduced to

$$\mathrm{Err}_{\mathrm{RMS}} = \sqrt{1 - \frac{3\,\mathrm{sinc}^4(kh/2)}{2+\cos(kh)}} \tag{5.31}$$

for θ-polarization, which is the same as the 1-D RMS error of triangular basis function using Galerkin method and

$$\mathrm{Err}_{\mathrm{RMS}} = \sqrt{1 - \mathrm{sinc}^2(kh/2)} \tag{5.32}$$

for ϕ polarization, which is the same as that of pulse basis function using Galerkin method. This is expected since when $\theta_i = 90^\circ$ and $\phi_i = 0^\circ$, the divergence-confirming basis on the rectangular element can be equivalent to the triangular and pulse basis for θ and ϕ polarization, respectively.

When $|\beta_1| << 1$ and $|\beta_2| << 1$, the asymptotical RMS error can be obtained by using Taylor series expansion of $\cos x$ and $\mathrm{sinc}\, x$

$$\mathrm{Err}_{\mathrm{RMS\_ASM}} = \frac{kh\sin\theta_i}{2\sqrt{6}}\sqrt{\sin^2(2\phi_i) + (kh\sin\theta_i)^2[1 - 1.25\sin^2(2\phi_i)]/30} \tag{5.33}$$

for θ-polarization and

$$\mathrm{Err}_{\mathrm{RMS\_ASM}} = \frac{kh\sin\theta_i}{2\sqrt{6}}\sqrt{2 - \sin^2(2\phi_i)} \tag{5.34}$$

for ϕ-polarization. The asymptotical expression indicates that when kh is small, the RMS error normalized by $\sin\theta_i$ is almost not dependent on θ_i and linearly varies with the size of element at the specified ϕ_i.

In addition, the RMS error of the basis on rectangular element is numerically calculated. The computational domain is truncated into a rectangular area. Each coefficient at the edge of the domain corresponds to a half basis function rather than one basis function. Figure 5.5 shows the analytical, numerical and asymptotical RMS error of the divergence-conforming basis on rectangular element. The mesh size is $\Delta x = \Delta y = h = 0.1\lambda$. The whole size of domain for numerical error is set to $2\lambda \times 2\lambda$. As shown in Figure 5.5, the numerical and analytical results agree very well. Thus, the edge effect is not significant for the RMS error. Figure 5.6 shows the numerical RMS error normalized by $\sin\theta_i$. As shown in this figure, the normalized error is almost not dependent on the angle θ_i. From (5.17) or (5.18), we find that the apparent wavelength on the plane of $z = 0$ is $\lambda/\sin\theta_i$. The number of unknowns per wavelength is larger than the original mesh density $\lambda/h = 10$. Thus, the smaller θ_i is, the smaller the projection error is.

It is observed that the projection error for θ-polarization is less than that for ϕ-polarization. This is because both the current of θ-polarization and the divergence-conforming basis function are curl-free. Figure 5.7 plots the error pattern for different sizes of element. As shown in this figure, the projection error deceases linearly with the size of element decreasing. This is consistent with what the asymptotical expression indicates.

5.2.2 Projection error of basis functions on triangular elements

In this subsection,the current is expanded by the divergence-conforming basis function on triangular elements. This type of basis function and RWG basis function are essentially identical [85]. The RWG basis function is also used as the testing function. The derivation of analytical RMS error of RWG basis function is complex. It is only derived of the analytical RMS error of RWG basis function on infinite one-directional mesh [54] as shown in Fig. 5.8(a). The details of derivation are given in Appendix. For θ-polarization,

$$\mathrm{Err}_{\mathrm{RMS}} = \sqrt{1 - \{\frac{3[|I_1|^2 + |I_2|^2 + |I_1 + I_2|^2]}{4 - \cos^2(\beta_1 - \beta_2)} + \frac{3}{2}|I_3|^2\}} \tag{5.35}$$

and for ϕ-polarization,

$$\mathrm{Err}_{\mathrm{RMS}} = \sqrt{1 - \{\frac{3[|I_1|^2 + |I_2|^2 + |I_1 + I_2|^2]}{4 - \cos^2(\beta_1 - \beta_2)} + \frac{3}{2}|I_3|^2\}/\cos^2\theta_i} \tag{5.36}$$

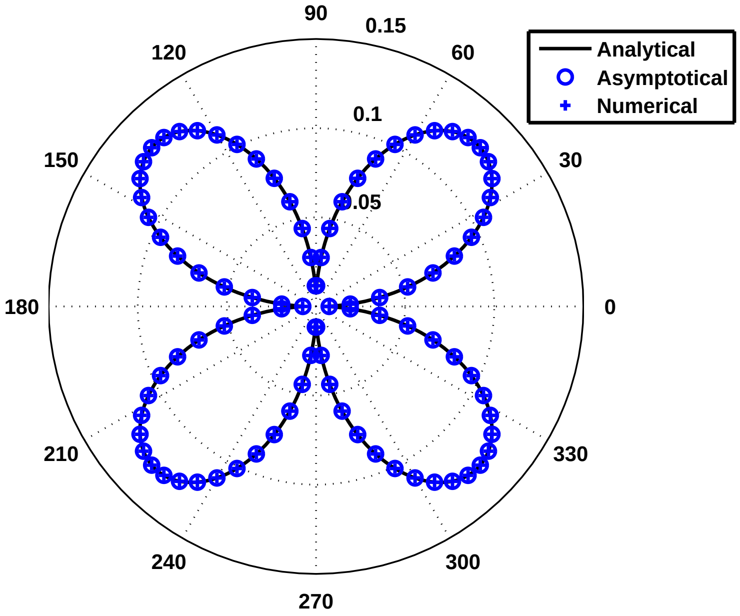

(a) θ-polarization

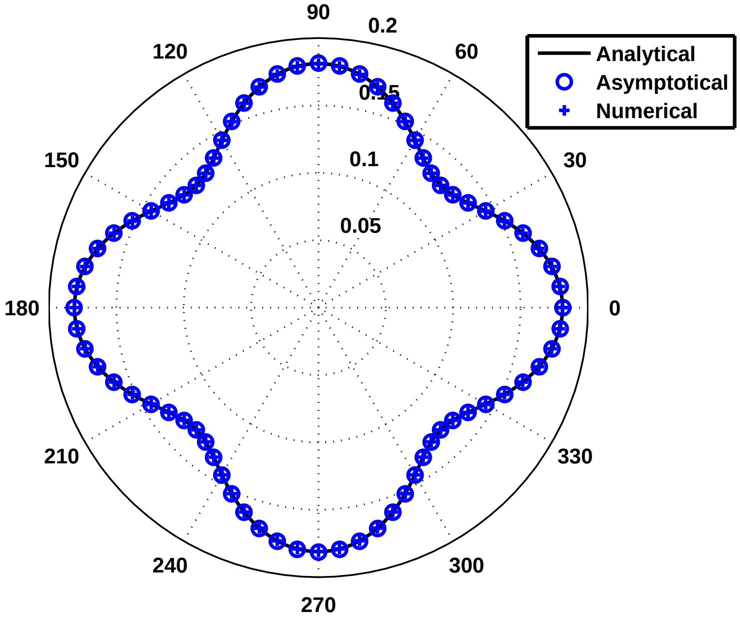

(b) ϕ-polarization

Figure 5.5 Projection error, normalized by $\sin\theta_i$, of basis functions on rectangular element at $\theta_i = 30°$ ($h = 0.1\lambda$).

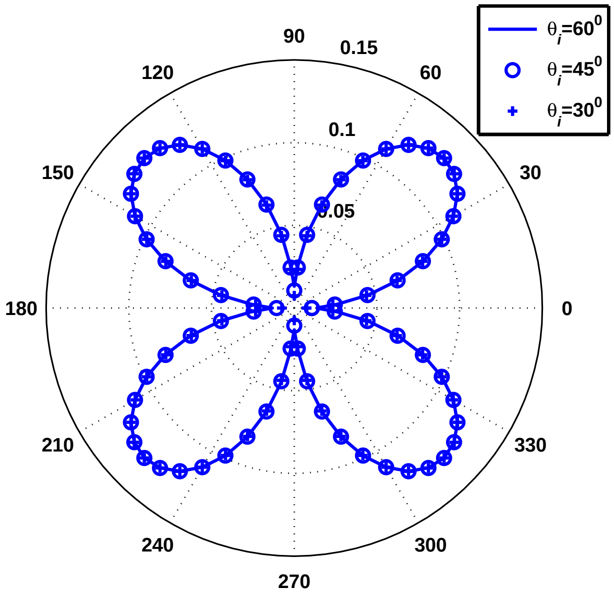

(a) θ-polarization

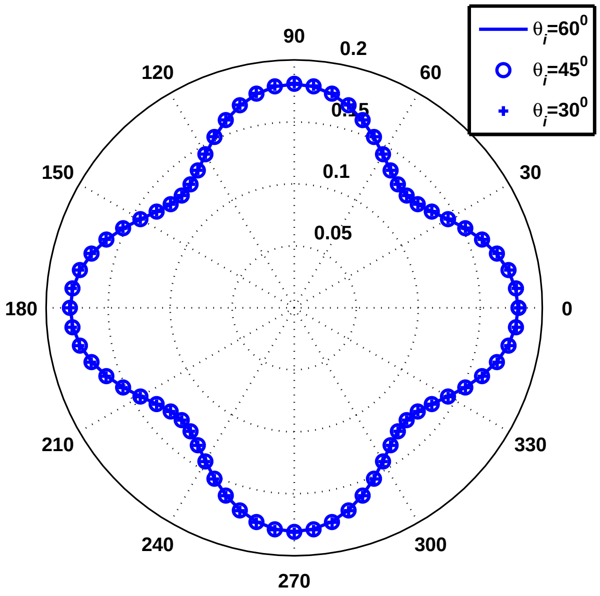

(b) ϕ-polarization

Figure 5.6 Numerical projection error, normalized by $\sin\theta_i$, of basis functions on rectangular elements in different θ_i ($h = 0.1\lambda$).

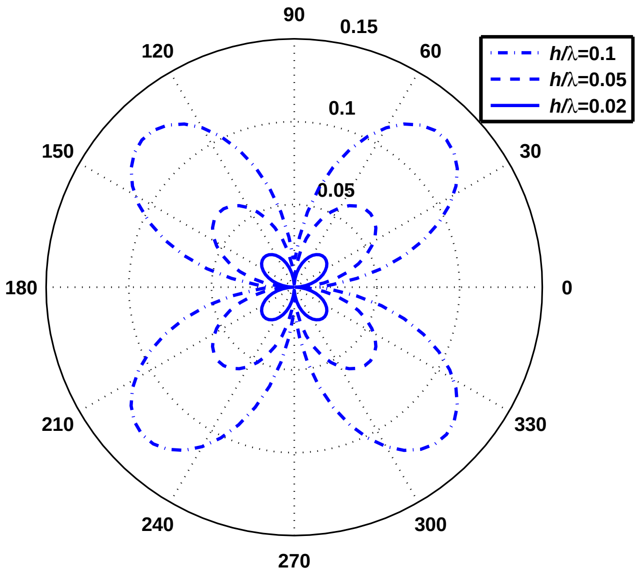

(a) θ-polarization

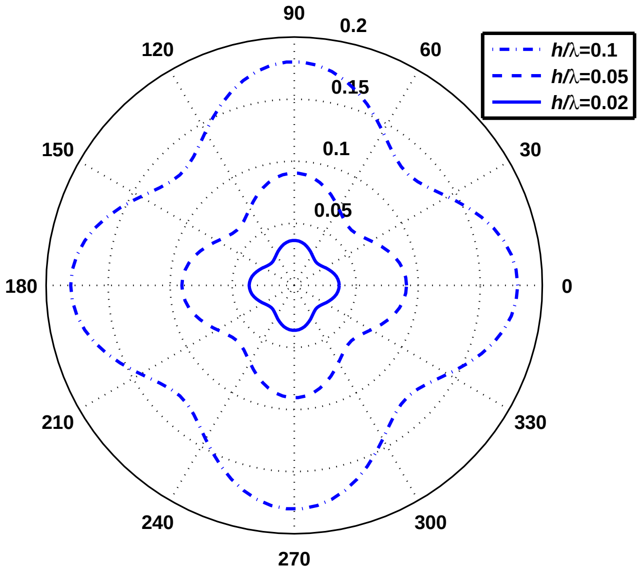

(b) ϕ-polarization

Figure 5.7 Numerical projection error, normalized by $\sin\theta_i$, of basis functions on rectangular elements with different sizes. $\theta_i = 89^\circ$.

where

$$I_1 = E_1 + E_1^* \exp(j\beta_2)$$

$$I_2 = E_2 + E_2^* \exp(j\beta_1)$$

$$I_3 = E_3 + E_3^* \exp(j\beta_1 + j\beta_2)$$

$$E_1 = -V_1 I_{11}(j\beta_1, j\beta_2) - V_2 I_{12}(j\beta_1, j\beta_2)$$

$$E_2 = V_1 I_{21}(j\beta_1, j\beta_2) + V_2 I_{22}(j\beta_1, j\beta_2)$$

$$E_3 = \sqrt{2}[-V_1 I_{11}(j\beta_1, j\beta_2) + V_2 I_{22}(j\beta_1, j\beta_2)]$$

$$V_1 = \begin{cases} \sin\phi_i, & \theta\text{-polariztion} \\ \cos\theta_i \cos\phi_i, & \phi\text{-polariztion} \end{cases}, \quad V_2 = \begin{cases} -\cos\phi_i, & \theta\text{-polariztion} \\ \cos\theta_i \sin\phi_i, & \phi\text{-polariztion} \end{cases}$$

$$I_{11}(x_1, x_2) = \frac{e^{x_1-x_2} - (x_1 - x_2) - 1}{(x_1 - x_2)^2} \frac{e^{x_2}}{x_2} - \frac{1}{x_2^2} \left[e^{x_2} \frac{e^{x_1-x_2} - 1}{x_1 - x_2} - \frac{e^{x_1} - 1}{x_1} \right]$$

$$I_{12}(x_1, x_2) = \frac{e^{x_1-x_2} - (x_1 - x_2) - 1}{(x_1 - x_2)^2} \frac{e^{x_2}}{x_2} - \frac{1}{x_1 x_2} \left[1 - \frac{e^{x_1} - 1}{x_1} \right]$$

$$I_{21}(x_1, x_2) = I_{12}(x_2, x_1), \; I_{22}(x_1, x_2) = I_{11}(x_2, x_1)$$

The asymptotical RMS error can be obtained

$$\text{Err}_{\text{RMS\_ASM}} = \frac{kh \sin\theta_i}{2\sqrt{6}} \sqrt{2 - \sin^2(2\phi_i)} \tag{5.37}$$

for θ-polarization and

$$\text{Err}_{\text{RMS\_ASM}} = \frac{kh \sin\theta_i}{2\sqrt{6}} \sqrt{2 + \sin^2(2\phi_i) - 2\sin(2\phi_i)} \tag{5.38}$$

for ϕ-polarization.

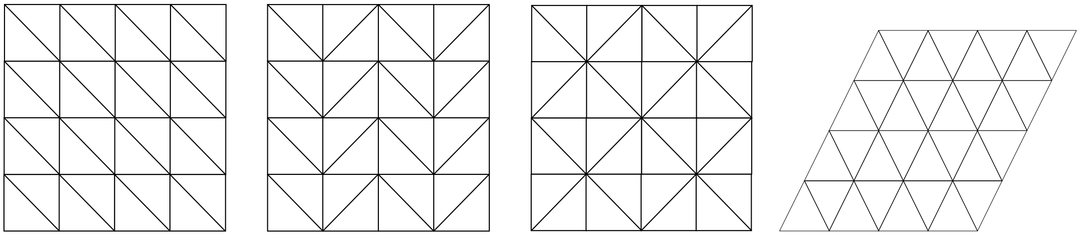

(a) One-directional (b) Arrow (c) Diamond (d) Hexagonal

Figure 5.8 Four types of triangular meshes.

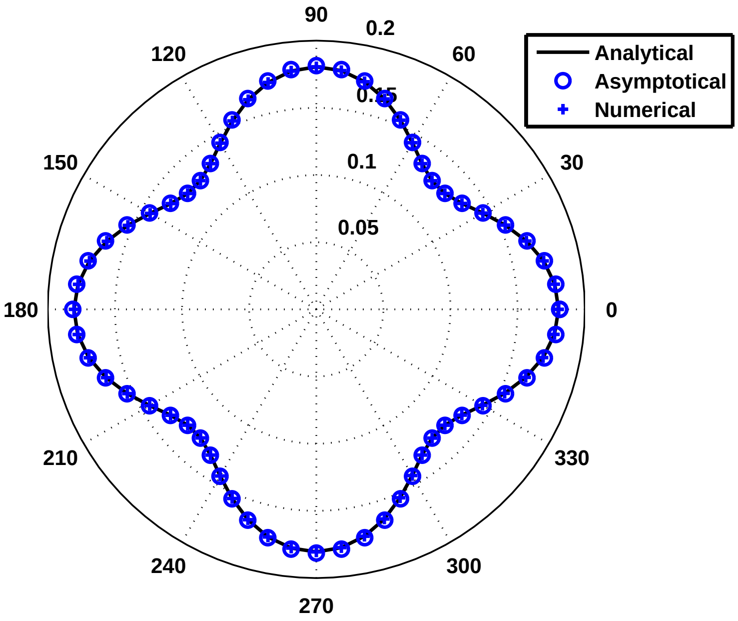

(a) θ-polarization

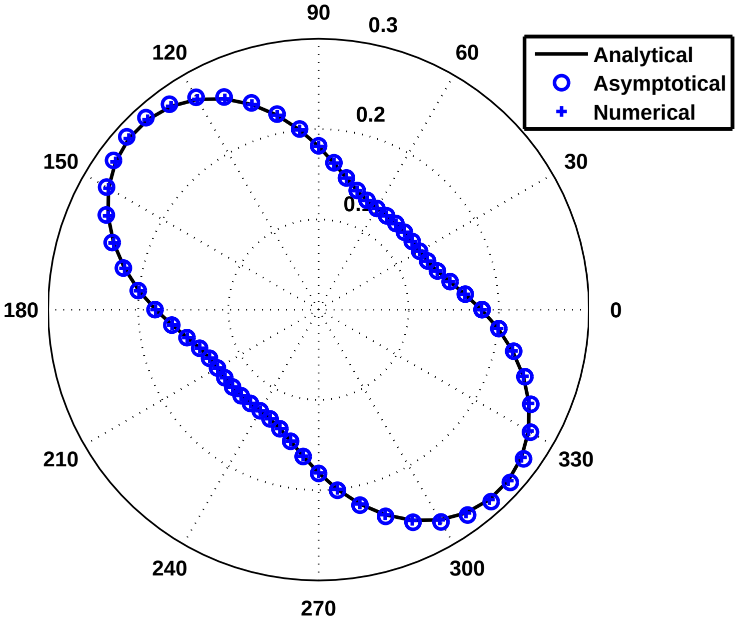

(b) ϕ-polarization

Figure 5.9 The projection error, normalized by $\sin\theta_i$, of basis functions on the one-directional triangular mesh at $\theta_i = 30°$. $h = 0.1\lambda$.

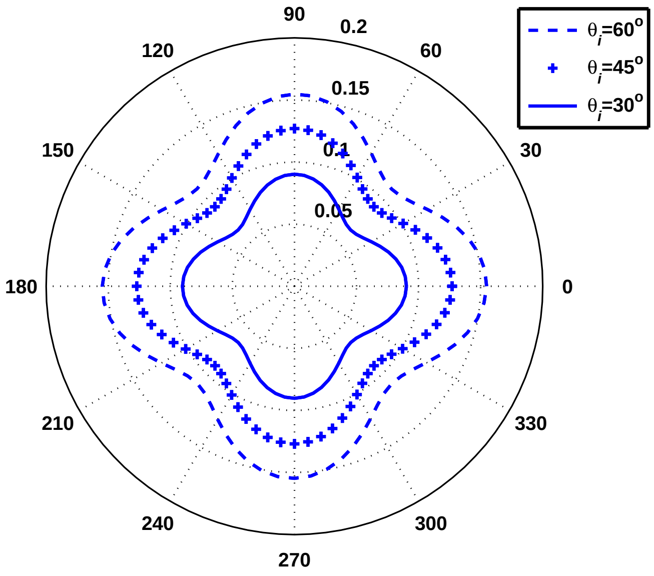

(a) θ-polarization

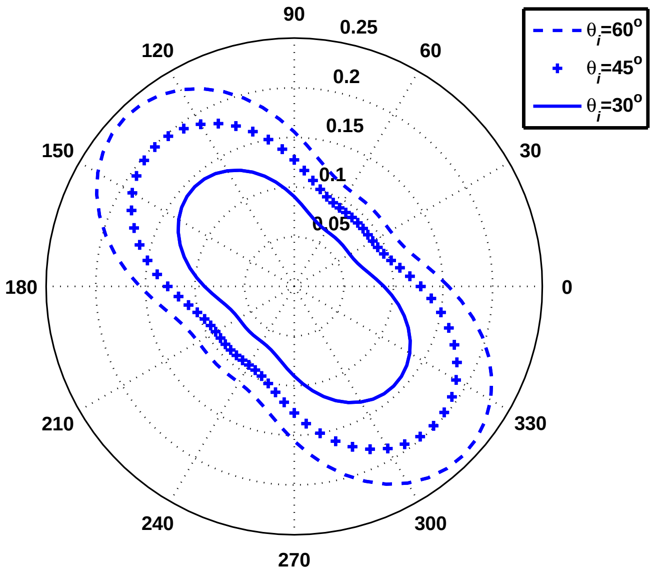

(b) ϕ-polarization

Figure 5.10 Analytical projection error for the one-directional triangular mesh as a function of ϕ_i at different angles θ_i. $h = 0.1\lambda$.

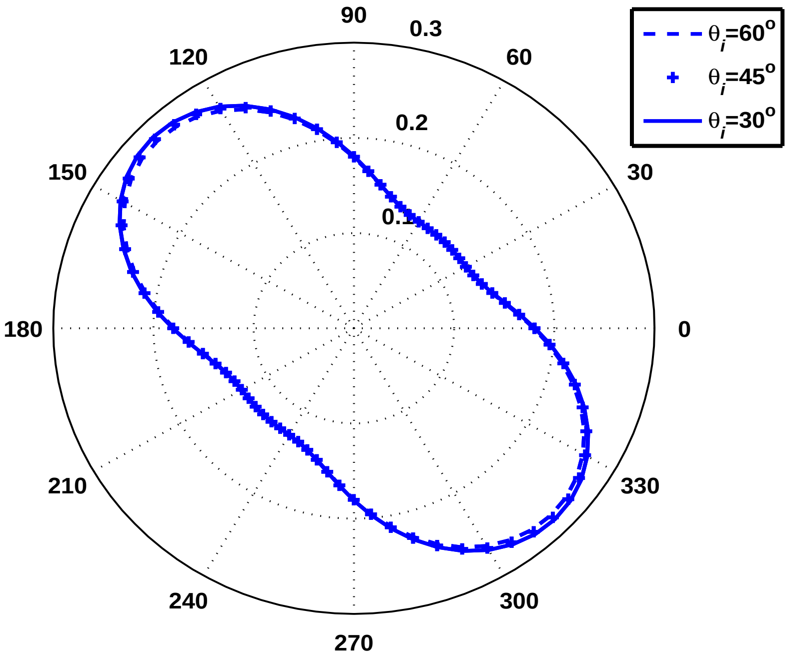

Figure 5.11 Analytical projection error, normalized by $\sin\theta_i$, for the one-directional triangular mesh as a function of ϕ_i (ϕ-polarization). $h = 0.1\lambda$.

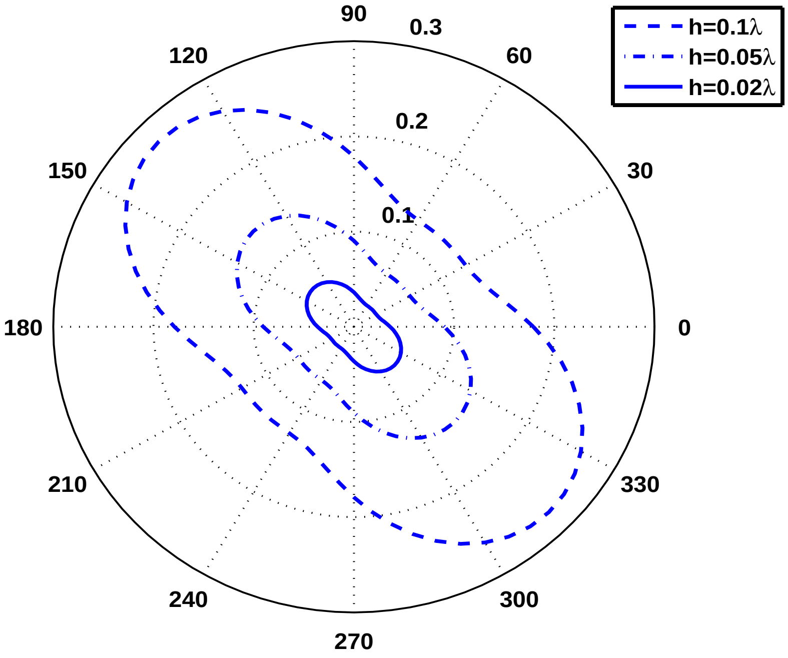

Figure 5.12 Analytical projection error, normalized by $\sin\theta_i$, for the one-directional triangular mesh with different sizes (ϕ-polarization). $\theta_i = 89°$.

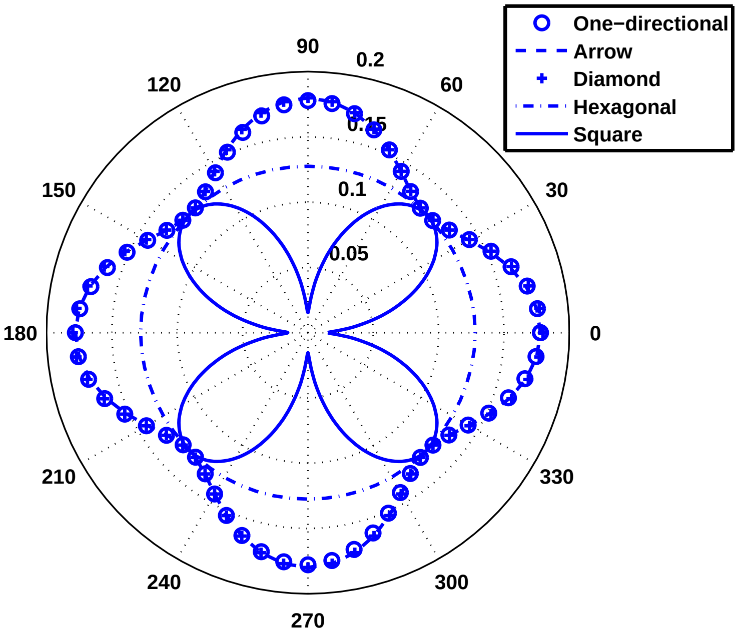

(a) θ-polarization

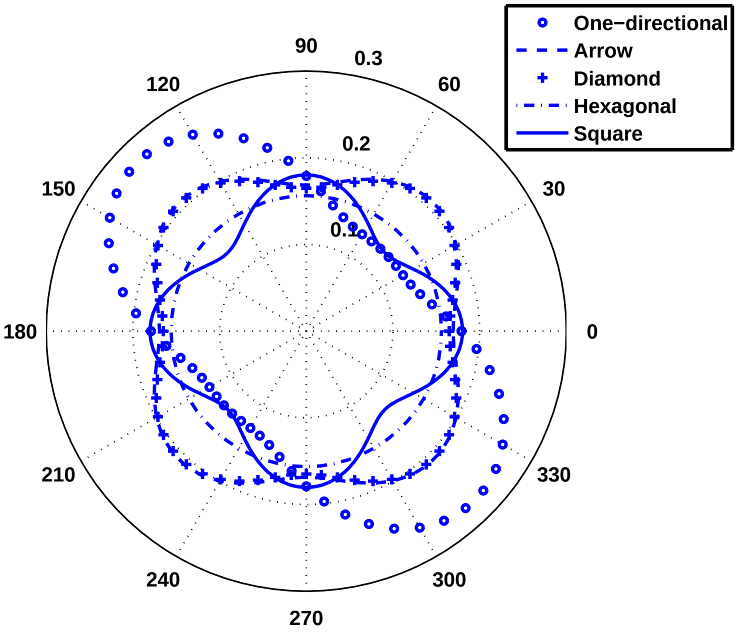

(b) ϕ-polarization

Figure 5.13 The numerical projection error, normalized by $\sin\theta_i$, for five different meshes as a function of ϕ_i. $\theta_i = 89^\circ$ and $h = 0.1\lambda$.

Additionally, it is numerically calculated of the RMS error of RWG basis function on one-directional, arrow, diamond, and hexagonal meshes [54], [65], [66]. For each mesh, the shortest distance between nodes is h. Figure 5.9 shows the analytical, asymptotical and numerical projection error of the RWG basis function on the one-directional mesh. Good agreement between them can be observed in this figure.

Figure 5.10 shows the projection error for one-directional mesh as a function of ϕ_i with different θ_i. It is found that the error in the projection of θ-polarization current (curl-free vector) is less than that of ϕ-polarization (divergence-free vector). This is because that the RWG basis functions are curl-free. As shown in Figure 5.10, the projection error is anisotropic and varies with the direction of propagation. Also, the severity of the anisotropic behavior relates to the element arrangement of the meshes and the polarization of the incident plane wave. Like the projection error of basis functions on rectangular elements, the smaller θ_i is, the smaller the projection error is. As indicated by the asymptotical form, the projection error normalized by $\sin\theta_i$ almost does not depend on θ_i, as shown in Figure 5.11. In Figure 5.12, the projection error plotted as a function of ϕ_i with three different values of h/λ has the same shape but different magnitude. The smaller the value of h/λ is, the smaller the error is. Furthermore, it is found that the error is proportional to h/λ.

Figure 5.13 shows the projection error as a function of ϕ_i for five different meshes with $\lambda/h = 10$ [65], [66]. The average unknowns density is $200/\lambda^2$ for the square mesh, $300/\lambda^2$ for one-directional, arrow, and diamond meshes, and $346/\lambda^2$ for hexagonal mesh. It is observed again that the error in the projection of θ-polarization current is less than that of ϕ-polarization. For the one-directional and arrow (or diamond) meshes, the projection errors are different for the ϕ-polarization; however, they agree with each other for the θ-polarization. The error in the hexagonal mesh is almost omnidirectional and less than the errors in the other three meshes in which the longest edge is $\sqrt{2}h$. The shape of the error curves for the ϕ-polarization is similar to that of the phase error in the finite element method using triangular nodal elements [54], [65], [66]. Moreover, the error pattern shape of rectangular element for ϕ-polarization is similar to that of one-directional, arrow and diamond meshes for θ-polarization.

CHAPTER 6 CONCLUSIONS

In Chapter 2, the IE approach for scattering from the singly periodic array of 2-D PEC conducting objects is described. In addition, the hybrid IE-plane wave approach is implemented to calculate the band structure of the metallic crystals. The numerical results generated by the in-house code can serve as the benchmark results to validate the proposed approaches in Chapters 3 and 4.

In Chapter 3, a DDM approach, which is based on equivalence principle and connection scheme (EPACS), is developed to calculate the scattering from multilayered periodic arrays. This approach does not involve the multilayered periodic Green's function. More importantly, based on EPACS, an effective approach is proposed to handle the case of semi-infinitely layered periodic arrays. The numerical results are provided to verify the proposed method. The efficiency of the proposed method is also demonstrated in this chapter. This method can be extended readily to calculate the scattering from 3-D doubly periodic structures with multiple and semi-infinite layers.

Chapter 4 addresses several issues in the integral-equation (IE) method for scattering from the doubly periodic array. First, the formulation in [21] is modified to facilitate the numerical implementation. Second, special testing and basis functions are proposed for the edges on the periodic boundary. The application of them can model the currents flowing out the truncated boundary of PEC. Third, the relationship for the reflection and transmission coefficients between the PEC screen with periodicity and its complementary structure is given. Numerical results are provided to validate the proposed approach.

In chapter 5, the projection error in 1D and 2D case is analyzed. The analytical projection error on the infinite meshes are given for 1D and 2D cases. The 1D case includes the pulse basis, triangular basis, the second-order basis, and the 2D case includes roof-top basis function and RWG basis function on the one-directional triangular mesh. In addition, the projection error of basis functions on rectangular elements is numerically calculated within a finite computational domain. A half basis function and one basis function are applied for each coefficient at the edge of and inside the domain, respectively. There are good agreements between the analytical and numerical results. It is found the projection error of p-th order 1D basis function is asymptotically inversely proportional to $(p+1)$-th power of the density of unknowns. It is also found that the error in projection of curl-free vectors is generally less than that of divergence-free vectors using the divergence-conforming basis function on both rectangular and triangular elements. In fact, the divergence-conforming basis is with the property of curl-free. So the basis function and the expanded vector are with the same property, i.e. curl-free. Thus, the projection error of curl-free vector should be smaller. The error in the 2D case decreases linearly with the mesh density increasing due to the low order of the basis functions.

APPENDIX A DERIVATION OF $R^{(1)}$

In what follows, the derivation of $R^{(1)}$ in (3.7) is given in detail. Rewriting (3.5) as

$$\begin{bmatrix} T_{11} & T_{12} & T_{13} & T_{14} \\ T_{21} & T_{22} & T_{23} & T_{24} \\ T_{31} & T_{32} & T_{33} & T_{34} \\ T_{41} & T_{42} & T_{43} & T_{44} \end{bmatrix} \begin{bmatrix} E_{t1} \\ E_{b1} \\ E_{l1} \\ E_{r1} \end{bmatrix} = \begin{bmatrix} S_{11} & S_{12} & S_{13} & S_{14} \\ S_{21} & S_{22} & S_{23} & S_{24} \\ S_{31} & S_{32} & S_{33} & S_{34} \\ S_{41} & S_{42} & S_{43} & S_{44} \end{bmatrix} \begin{bmatrix} J_{t1} \\ J_{b1} \\ J_{l1} \\ J_{r1} \end{bmatrix} \tag{A.1}$$

and employing (3.6), one will obtain

$$\begin{bmatrix} T_{11} & T_{12} & T'_{13} \\ T_{21} & T_{22} & T'_{23} \\ T_{31} & T_{32} & T'_{33} \\ T_{41} & T_{42} & T'_{43} \end{bmatrix} \begin{bmatrix} E_{t1} \\ E_{b1} \\ E_{l1} \end{bmatrix} = \begin{bmatrix} S_{11} & S_{12} & S'_{13} \\ S_{21} & S_{22} & S'_{23} \\ S_{31} & S_{32} & S'_{33} \\ S_{41} & S_{42} & S'_{43} \end{bmatrix} \begin{bmatrix} J_{t1} \\ J_{b1} \\ J_{l1} \end{bmatrix} \tag{A.2}$$

where $T'_{i3} = T_{i3} + T_{i4}e^{-jk_xP_L}$ and $S'_{i3} = S_{i3} - S_{i4}e^{-jk_xP_L}$ $(i = 1, 2, 3, 4)$. Reorganizing the last two sets of equations in (A.2) yields

$$\begin{bmatrix} T'_{33} & -S'_{33} \\ T'_{43} & -S'_{43} \end{bmatrix} \begin{bmatrix} E_{l1} \\ J_{l1} \end{bmatrix} = - \begin{bmatrix} T_{31} & T_{32} \\ T_{41} & T_{42} \end{bmatrix} \begin{bmatrix} E_{t1} \\ E_{b1} \end{bmatrix} + \begin{bmatrix} S_{31} & S_{32} \\ S_{41} & S_{42} \end{bmatrix} \begin{bmatrix} J_{t1} \\ J_{b1} \end{bmatrix} \tag{A.3}$$

Thus,

$$\begin{bmatrix} E_{l1} \\ J_{l1} \end{bmatrix} = \begin{bmatrix} T'_{33} & -S'_{33} \\ T'_{43} & -S'_{43} \end{bmatrix}^{-1} \left\{ - \begin{bmatrix} T_{31} & T_{32} \\ T_{41} & T_{42} \end{bmatrix} \begin{bmatrix} E_{t1} \\ E_{b1} \end{bmatrix} + \begin{bmatrix} S_{31} & S_{32} \\ S_{41} & S_{42} \end{bmatrix} \begin{bmatrix} J_{t1} \\ J_{b1} \end{bmatrix} \right\} \tag{A.4}$$

Reorganizing the first two sets of equations in (A.2) yields

$$\begin{bmatrix} T'_{13} & -S'_{13} \\ T'_{23} & -S'_{23} \end{bmatrix} \begin{bmatrix} E_{l1} \\ J_{l1} \end{bmatrix} + \begin{bmatrix} T_{11} & T_{12} \\ T_{21} & T_{22} \end{bmatrix} \begin{bmatrix} E_{t1} \\ E_{b1} \end{bmatrix} = \begin{bmatrix} S_{11} & S_{12} \\ S_{21} & S_{22} \end{bmatrix} \begin{bmatrix} J_{t1} \\ J_{b1} \end{bmatrix} \tag{A.5}$$

Combining (A.4) and (A.5), one can get

$$P \begin{bmatrix} E_{t1} \\ E_{b1} \end{bmatrix} = Q \begin{bmatrix} J_{t1} \\ J_{b1} \end{bmatrix} \tag{A.6}$$

where

$$P = \begin{bmatrix} T_{11} & T_{12} \\ T_{21} & T_{22} \end{bmatrix} - \begin{bmatrix} T'_{13} & -S'_{13} \\ T'_{23} & -S'_{23} \end{bmatrix} \begin{bmatrix} T'_{33} & -S'_{33} \\ T'_{43} & -S'_{43} \end{bmatrix}^{-1} \begin{bmatrix} T_{31} & T_{32} \\ T_{41} & T_{42} \end{bmatrix}$$

$$Q = \begin{bmatrix} S_{11} & S_{12} \\ S_{21} & S_{22} \end{bmatrix} - \begin{bmatrix} T'_{13} & -S'_{13} \\ T'_{23} & -S'_{23} \end{bmatrix} \begin{bmatrix} T'_{33} & -S'_{33} \\ T'_{43} & -S'_{43} \end{bmatrix}^{-1} \begin{bmatrix} S_{31} & S_{32} \\ S_{41} & S_{42} \end{bmatrix}$$

From (A.6),

$$\begin{bmatrix} E_{t1} \\ E_{b1} \end{bmatrix} = R^{(1)} \begin{bmatrix} J_{t1} \\ J_{b1} \end{bmatrix} \tag{A.7}$$

where

$$R^{(1)} = P^{-1} Q \tag{A.8}$$

APPENDIX B Derivation of formulations for doubly periodic arrays

B.1 Derivation of matrix elements

In this section, the derivation of (4.9) is given. Multiplying the testing function on both sides of (4.1) and performing the integral over PEC surface give (4.8) and

$$Z_{mn} = \int_s \int_{s'} \left[-(\mathbf{T}_m \cdot \nabla G_p)\nabla' \cdot \mathbf{B}_n - \beta^2 \mathbf{T}_m \cdot \mathbf{B}_n G_p \right] ds' ds \tag{B.1}$$

Applying the following identity

$$\nabla \cdot (f\mathbf{A}) = \mathbf{A} \cdot \nabla f + f \nabla \cdot \mathbf{A} \tag{B.2}$$

and the surface divergence theorem, one can change the integral of the first term in (B.1) into

$$\begin{aligned} I_1 = & \int_s \int_{s'} \nabla \cdot \mathbf{T}_m \nabla' \cdot \mathbf{B}_n G_p ds' ds \\ & - \int_{C^+} (\mathbf{u} \cdot \mathbf{T}_m) \int_{s'} \nabla' \cdot \mathbf{B}_n G_p ds' dl \\ & - \int_{C^-} (\mathbf{u} \cdot \mathbf{T}_m) \int_{s'} \nabla' \cdot \mathbf{B}_n G_p ds' dl \end{aligned} \tag{B.3}$$

where s denotes two triangular elements associated with $\mathbf{T}_m$, and s' denotes two ones associated with $\mathbf{B}_n$. $\mathbf{u}$ denotes the unit vector normal to contour $C^{\pm}$ bounding the two triangular elements s. Assume E^+ and E^- are the two elements denoted by s, as shown in Fig. 4.2. Since $\mathbf{u} \cdot \mathbf{T}_m = 0$ holds at the four edges which do not correspond to the testing function $\mathbf{T}_m$, (B.3) will reduce to

$$\begin{aligned} I_1 = & \int_s \int_{s'} \nabla \cdot \mathbf{T}_m \nabla' \cdot \mathbf{B}_n G_p ds' ds \\ & - \int_{l^+} (\mathbf{u} \cdot \mathbf{T}_m) \int_{s'} \nabla' \cdot \mathbf{B}_n G_p ds' dl \\ & - \int_{l^-} (\mathbf{u} \cdot \mathbf{T}_m) \int_{s'} \nabla' \cdot \mathbf{B}_n G_p ds' dl \end{aligned} \tag{B.4}$$

Here l^+ and l^- denote the edges corresponding to $\mathbf{T}_m$ on E^+ and E^-, respectively. $\nabla' \cdot \mathbf{B}_n$ is a constant and can be moved outside the line-surface integral. For the first type of edge, $\mathbf{u} \cdot \mathbf{T}_m = \pm 1$ at l^+ and l^-, respectively. Thus, the two line-surface integrals are cancelled with each other.

For the second type of edge, $\mathbf{u} \cdot \mathbf{T}_m = e^{j\mathbf{k}\cdot\mathbf{a_1}}$ and $\mathbf{u} \cdot \mathbf{T}_m = -1$ at l^+ and l^-, respectively. Then the term about line-surface integral is given by

$$I_{ls} = -\nabla' \cdot \mathbf{B}_n \left[e^{j\mathbf{k}\cdot\mathbf{a_1}} \int_{l^+} \int_{s'} G_p ds' dl - \int_{l^-} \int_{s'} G_p ds' dl \right] \tag{B.5}$$

The coordinate transformation $\mathbf{r}^+ = \mathbf{r}^- + \mathbf{a_1}$ is used for the first term in the bracket of (B.5). In addition, according to the Floquet's theorem,

$$G_p(\mathbf{u} + \mathbf{a_1}) = G_p(\mathbf{u}) e^{-j\mathbf{k}\cdot\mathbf{a_1}} \tag{B.6}$$

Thus,

$$I_{ls} = -\nabla' \cdot \mathbf{B}_n \left[e^{j\mathbf{k}\cdot\mathbf{a_1}} \int_{l^-} \int_{s'} G_p e^{-j\mathbf{k}\cdot\mathbf{a_1}} ds' dl - \int_{l^-} \int_{s'} G_p ds' dl \right] = 0 \tag{B.7}$$

Combination of (B.4) and (B.7) gives

$$I_1 = \int_s \int_{s'} \nabla \cdot \mathbf{T}_m \nabla' \cdot \mathbf{B}_n G_p ds' ds \tag{B.8}$$

In the similar manner, one can obtain (B.8) for the case of the third type of edges.

B.2 Proof of Babinet's principle

(i) Let the EM field

$$\mathbf{E}^{inc} = \mathbf{F}, \quad \bar{\mathbf{H}}^{inc} = \eta \mathbf{H}^{inc} = \hat{k} \times \mathbf{F} \tag{B.9}$$

be incident in $z > 0$ on the PEC screen on the plane $z = 0$; Let the total field in $z < 0$ be $\mathbf{E}^1$, $\bar{\mathbf{H}}^1$.

(ii) Let the EM field

$$\mathbf{E}^{inc} = -\hat{k} \times \mathbf{F}, \quad \bar{\mathbf{H}}^{inc} = \mathbf{F} \tag{B.10}$$

be incident in $z > 0$ on the complementary PEC screen on the plane $z = 0$; Let the total field in $z < 0$ be $\mathbf{E}^2$, $\bar{\mathbf{H}}^2$.

Then, the Babinet's principle asserts that [50]

$$\mathbf{E}^1 + \bar{\mathbf{H}}^2 = \mathbf{F}, \quad \bar{\mathbf{H}}^1 - \mathbf{E}^2 = \hat{k} \times \mathbf{F} \tag{B.11}$$

In fact, one may have

$$j\beta \int_S [\bar{\mathbf{J}}(\mathbf{r}') + \frac{1}{\beta^2}\nabla' \cdot \bar{\mathbf{J}}(\mathbf{r}')\nabla] G_p(\mathbf{r}, \mathbf{r}') ds' = \mathbf{F} \tag{B.12}$$

for Problem (i), and

$$j\beta \int_S [\mathbf{M}(\mathbf{r}') + \frac{1}{\beta^2}\nabla' \cdot \mathbf{M}(\mathbf{r}')\nabla] G_p(\mathbf{r}, \mathbf{r}') ds' = \mathbf{F} \tag{B.13}$$

for Problem (ii). Here $\bar{\mathbf{J}} = \eta \mathbf{J}$ and $\mathbf{M} = 2\mathbf{E} \times \hat{z}$. As shown in (B.12) and (B.13), $\bar{\mathbf{J}}$ and $\mathbf{M}$ satisfy the same integral equation on the same domain. Thus,

$$\bar{\mathbf{J}} = \mathbf{M} \tag{B.14}$$

The total fields $z < 0$ are given by

$$\mathbf{E}^1 = \mathbf{F} - j\beta \int_S [\bar{\mathbf{J}}(\mathbf{r}') + \frac{1}{\beta^2}\nabla' \cdot \bar{\mathbf{J}}(\mathbf{r}')\nabla] G_p(\mathbf{r}, \mathbf{r}') ds' \tag{B.15}$$

for Problem (i), and

$$\bar{\mathbf{H}}^2 = j\beta \int_S [\mathbf{M}(\mathbf{r}') + \frac{1}{\beta^2}\nabla' \cdot \mathbf{M}(\mathbf{r}')\nabla] G_p(\mathbf{r}, \mathbf{r}') ds' \tag{B.16}$$

for Problem (ii). Adding (B.15) to (B.16) yields

$$\mathbf{E}^1 + \bar{\mathbf{H}}^2 = \mathbf{F} \tag{B.17}$$

Taking curl of both sides of (B.17) and then taking advantage of Maxwell equations and $\nabla \times \mathbf{F} = -j\beta\hat{k} \times \mathbf{F}$ gives

$$\bar{\mathbf{H}}^1 - \mathbf{E}^2 = \hat{k} \times \mathbf{F} \tag{B.18}$$

B.3 Derivation of reflection and transmission coefficients

The electric and magnetic fields can be expanded into the TMz and TEz Floquet's modes

$$\begin{aligned} \mathbf{E}_t = & \sum_{\mathbf{J}} (a_{\mathbf{J}} e^{-\gamma_{\mathbf{J}} z} + b_{\mathbf{J}} e^{\gamma_{\mathbf{J}} z}) \sqrt{Z_{\mathbf{J},\mathrm{TM}}}\, \mathbf{e}_{t\mathbf{J},\mathrm{TM}} \\ & + \sum_{\mathbf{J}} (c_{\mathbf{J}} e^{-\gamma_{\mathbf{J}} z} + d_{\mathbf{J}} e^{\gamma_{\mathbf{J}} z}) \sqrt{Z_{\mathbf{J},\mathrm{TE}}}\, \mathbf{e}_{t\mathbf{J},\mathrm{TE}} \end{aligned} \tag{B.19}$$

$$E_z = \sum_{\mathbf{J}} (a_{\mathbf{J}} e^{-\gamma_{\mathbf{J}} z} - b_{\mathbf{J}} e^{\gamma_{\mathbf{J}} z}) \sqrt{Z_{\mathbf{J},\mathrm{TM}}}\, e_{z\mathbf{J},\mathrm{TM}} \tag{B.20}$$

$$\begin{aligned} \mathbf{H}_t &= \sum_{\mathbf{J}} (a_{\mathbf{J}} e^{-\gamma_{\mathbf{J}} z} - b_{\mathbf{J}} e^{\gamma_{\mathbf{J}} z}) \frac{1}{\sqrt{Z_{\mathbf{J},\mathrm{TM}}}} \mathbf{h}_{t\mathbf{J},\mathrm{TM}} \\ &+ \sum_{\mathbf{J}} (c_{\mathbf{J}} e^{-\gamma_{\mathbf{J}} z} - d_{\mathbf{J}} e^{\gamma_{\mathbf{J}} z}) \frac{1}{\sqrt{Z_{\mathbf{J},\mathrm{TE}}}} \mathbf{h}_{t\mathbf{J},\mathrm{TE}} \end{aligned} \tag{B.21}$$

$$H_z = \sum_{\mathbf{J}} (c_{\mathbf{J}} e^{-\gamma_{\mathbf{J}} z} + d_{\mathbf{J}} e^{\gamma_{\mathbf{J}} z}) \frac{1}{\sqrt{Z_{\mathbf{J},\mathrm{TE}}}} h_{z\mathbf{J},\mathrm{TE}} \tag{B.22}$$

Table B.1 Description of TMz and TEz Floquet's modes

TMz	TEz
$\mathbf{h}_{t\mathbf{J},\mathrm{TM}} = j\chi_{\mathbf{J}} \frac{\hat{z}\times\mathbf{k}_{\mathbf{J}\parallel}}{\lvert\mathbf{k}_{\mathbf{J}\parallel}\rvert}$	$\mathbf{e}_{t\mathbf{J},\mathrm{TE}} = -j\chi_{\mathbf{J}} \frac{\hat{z}\times\mathbf{k}_{\mathbf{J}\parallel}}{\lvert\mathbf{k}_{\mathbf{J}\parallel}\rvert}$
$\mathbf{e}_{t\mathbf{J},\mathrm{TM}} = j\chi_{\mathbf{J}} \frac{\mathbf{k}_{\mathbf{J}\parallel}}{\lvert\mathbf{k}_{\mathbf{J}\parallel}\rvert}$	$\mathbf{h}_{t\mathbf{J},\mathrm{TE}} = j\chi_{\mathbf{J}} \frac{\mathbf{k}_{\mathbf{J}\parallel}}{\lvert\mathbf{k}_{\mathbf{J}\parallel}\rvert}$
$e_{z\mathbf{J},\mathrm{TM}} = \frac{\lvert\mathbf{k}_{\mathbf{J}\parallel}\rvert}{\gamma_{\mathbf{J}}}\chi_{\mathbf{J}}$	$h_{z\mathbf{J},\mathrm{TE}} = \frac{\lvert\mathbf{k}_{\mathbf{J}\parallel}\rvert}{\gamma_{\mathbf{J}}}\chi_{\mathbf{J}}$
$Z_{\mathbf{J},\mathrm{TM}} = \frac{\gamma_{\mathbf{J}}}{j\omega\epsilon}$	$Z_{\mathbf{J},\mathrm{TE}} = \frac{j\omega\mu}{\gamma_{\mathbf{J}}}$

Table B.1 shows the vector function for the TMz and TEz Floquet's modes [33]. Here

$$\chi_{\mathbf{J}} = \frac{1}{\sqrt{\Omega}} e^{-j\mathbf{k}_{\mathbf{J}\parallel}\cdot\boldsymbol{\rho}} \tag{B.23}$$

When $\boldsymbol{\kappa}_{\mathbf{J}\parallel} = 0$ and $\mathbf{k}_{\parallel} = 0$ ($\sin\theta^i = 0$),

$$\mathbf{e}_{t\mathbf{J}} = j\chi_{\mathbf{J}}\hat{k}_{\rho} \tag{B.24}$$

for the TMz case and

$$\mathbf{e}_{t\mathbf{J}} = -j\chi_{\mathbf{J}}\hat{z}\times\hat{k}_{\rho} \tag{B.25}$$

for the TEz case. Here $\hat{k}_{\rho} = -(\hat{x}\cos\phi^i + \hat{y}\sin\phi^i)$.

It is easy to verify the following orthogonality of $\mathbf{e}_{t\mathbf{J}}$ and $\mathbf{h}_{t\mathbf{J}}$

$$\int_{\Omega} \mathbf{e}_{t\mathbf{J_1},\mathrm{TM}} \cdot \mathbf{e}^*_{t\mathbf{J_2},\mathrm{TM}} ds = \begin{cases} 1, & \mathbf{J_1} = \mathbf{J_2} \\ 0, & \mathbf{J_1} \neq \mathbf{J_2} \end{cases} \tag{B.26}$$

$$\int_{\Omega} \mathbf{h}_{t\mathbf{J_1},\mathrm{TM}} \cdot \mathbf{h}^*_{t\mathbf{J_2},\mathrm{TM}} ds = \begin{cases} 1, & \mathbf{J_1} = \mathbf{J_2} \\ 0, & \mathbf{J_1} \neq \mathbf{J_2} \end{cases} \tag{B.27}$$

$$\int_{\Omega} \mathbf{e}_{t\mathbf{J_1},\mathrm{TE}} \cdot \mathbf{e}^{*}_{t\mathbf{J_2},\mathrm{TE}} ds = \begin{cases} 1, & \mathbf{J_1} = \mathbf{J_2} \\ 0, & \mathbf{J_1} \neq \mathbf{J_2} \end{cases} \tag{B.28}$$

$$\int_{\Omega} \mathbf{h}_{t\mathbf{J_1},\mathrm{TE}} \cdot \mathbf{h}^{*}_{t\mathbf{J_2},\mathrm{TE}} ds = \begin{cases} 1, & \mathbf{J_1} = \mathbf{J_2} \\ 0, & \mathbf{J_1} \neq \mathbf{J_2} \end{cases} \tag{B.29}$$

$$\int_{\Omega} \mathbf{e}_{t\mathbf{J_1},\mathrm{TE}} \cdot \mathbf{e}^{*}_{t\mathbf{J_2},\mathrm{TM}} ds = 0, \quad \int_{\Omega} \mathbf{h}_{t\mathbf{J_1},\mathrm{TE}} \cdot \mathbf{h}^{*}_{t\mathbf{J_2},\mathrm{TM}} ds = 0 \tag{B.30}$$

The incident plane wave is a special case of (B.19)-(B.22), whose electric field is expressed as

$$\mathbf{E}^{inc} = (\hat{\theta} \cos\alpha + \hat{\phi} \sin\alpha) E_0 e^{-j\mathbf{k}\cdot\mathbf{r}} \tag{B.31}$$

where $\mathbf{k} = \mathbf{k}_{\|} - \hat{z}k_z$, $\mathbf{k}_{\|} = \hat{k}_{\rho}\beta \sin\theta^i$, and $k_z = \beta\cos\theta^i$.

It is easy to verify that the incident plane wave is the combination of **0**th-order TMz and TEz Floquet's modes. For θ-polarization ($\alpha = 0^{\mathrm{o}}$),

$$\mathbf{E}^{inc} = b^i_{\mathbf{0},\mathrm{TM}} e^{\gamma_{\mathbf{0}} z} \sqrt{Z_{\mathbf{0},\mathrm{TM}}} (\mathbf{e}_{t\mathbf{0},\mathrm{TM}} - e_{z\mathbf{0},\mathrm{TM}}) \tag{B.32}$$

where $b^i_{\mathbf{0},\mathrm{TM}} = jE_0\sqrt{\Omega\cos\theta^i/\eta}$ and $\gamma_{\mathbf{0}} = j\beta\cos\theta^i$. For ϕ-polarization ($\alpha = 90^{\mathrm{o}}$),

$$\mathbf{E}^{inc} = b^i_{\mathbf{0},\mathrm{TE}} e^{\gamma_{\mathbf{0}} z} \sqrt{Z_{\mathbf{0},\mathrm{TE}}}\, \mathbf{e}_{t\mathbf{0},\mathrm{TE}} \tag{B.33}$$

where $b^i_{\mathbf{0},\mathrm{TE}} = -jE_0\sqrt{\Omega\cos\theta^i/\eta}$.

For the MFIE approach, one can first apply the equivalence principle and image theory [48]-[49] to find the magnetic field in terms of the tangential electric fields on the apertures S_a. Assuming the screen is located at $z = 0$, one may have

$$\begin{aligned} &\mathbf{H}^{inc} + \mathbf{H}^{r} = \mathbf{H} + \boldsymbol{L}(\mathbf{M}), \quad z > 0 \\ &0 = \mathbf{H} - \boldsymbol{L}(\mathbf{M}), \quad z < 0 \end{aligned} \tag{B.34}$$

where

$$\boldsymbol{L}(\mathbf{M}) = j\omega\epsilon \int_{S_a} \mathbf{M}(\mathbf{r}') \cdot [\bar{\mathbf{I}} + \frac{1}{\beta^2}\nabla\nabla] G_p(\mathbf{r}, \mathbf{r}') ds' \tag{B.35}$$

$\mathbf{M} = 2\mathbf{E} \times \hat{z}$. $\mathbf{H}^r$ is the reflected field by infinite PEC surface. From (B.34), the MFIE on the aperture can be established

$$\boldsymbol{L}_t(\mathbf{M}) = \mathbf{H}_t^{inc}, \ z = 0 \tag{B.36}$$

The scattered field above the aperture can be found by

$$\mathbf{H}^s = -\boldsymbol{L}(\mathbf{M}) + \mathbf{H}^r, \quad z > 0 \tag{B.37}$$

The transverse components of incident and reflected magnetic fields are given by, respectively

$$\mathbf{H}_t^i = -b_{\mathbf{J_0}}^i e^{\gamma_{\mathbf{J_0}} z} \frac{1}{\sqrt{Z_{\mathbf{J_0}}}} \mathbf{h}_{t\mathbf{J_0}} \tag{B.38}$$

and

$$\mathbf{H}_t^r = -b_{\mathbf{J_0}}^i e^{-\gamma_{\mathbf{J_0}} z} \frac{1}{\sqrt{Z_{\mathbf{J_0}}}} \mathbf{h}_{t\mathbf{J_0}} \tag{B.39}$$

At $z = z_r$, the transverse component of $-\boldsymbol{L}(\mathbf{M})$ can be expanded as

$$-\boldsymbol{L}_t(\mathbf{M}) = \sum_{\mathbf{J}} a_{\mathbf{J}} e^{-\gamma_{\mathbf{J}} z_r} \frac{1}{\sqrt{Z_{\mathbf{J}}}} \mathbf{h}_{t\mathbf{J}} \tag{B.40}$$

Using (B.40) and the orthogonality of Floquet's modes yields

$$a_{\mathbf{J}} = -e^{\gamma_{\mathbf{J}} z_r} \sqrt{Z_{\mathbf{J}}} \int_{S_r} \boldsymbol{L}(\mathbf{M}) \cdot \mathbf{h}_{t\mathbf{J}}^* ds \tag{B.41}$$

since $\boldsymbol{L}_t(\mathbf{M}) \cdot \mathbf{h}_{t\mathbf{J}}^* = \boldsymbol{L}(\mathbf{M}) \cdot \mathbf{h}_{t\mathbf{J}}^*$. The reflection (transmission) coefficient is defined as the ratio of the Floquet's modes coefficient of the reflected (transmitted) electric field to that of the incident electric field. From (B.37), (B.39), (B.19), and (B.21), the reflection coefficient can be found by

$$\Gamma = \frac{a_{\mathbf{J}} - \delta_{\mathbf{J_0}\mathbf{J}} b_{\mathbf{J_0}}^i}{b_{\mathbf{J_0}}^i} \tag{B.42}$$

Substitution of (B.41) into (B.42) yields

$$\Gamma = -\frac{e^{\gamma_{\mathbf{J}} z_r} \sqrt{Z_{\mathbf{J}}}}{b_{\mathbf{J_0}}^i} \int_{S_r} \boldsymbol{L}(\mathbf{M}) \cdot \mathbf{h}_{t\mathbf{J}}^* ds - \delta_{\mathbf{J_0}\mathbf{J}} \tag{B.43}$$

At $z = z_t$, $\mathbf{H}_t$ can be expanded as

$$\mathbf{H}_t = \sum_{\mathbf{J}} (-b_{\mathbf{J}}) e^{\gamma_{\mathbf{J}} z_t} \frac{1}{\sqrt{Z_{\mathbf{J}}}} \mathbf{h}_{t\mathbf{J}} \tag{B.44}$$

Using (B.44) and the orthogonality of Floquet modes yields

$$b_{\mathbf{J}} = -e^{-\gamma_{\mathbf{J}} z_t}\sqrt{Z_{\mathbf{J}}}\int_{S_t}\mathbf{H}\cdot\mathbf{h}^*_{t\mathbf{J}}ds \tag{B.45}$$

The transmission coefficient can be found by

$$T = \frac{b_{\mathbf{J}}}{b^i_{\mathbf{J_o}}} \tag{B.46}$$

Substitution of (B.45) into (B.46) yields

$$T = -\frac{e^{-\gamma_{\mathbf{J}} z_t}\sqrt{Z_{\mathbf{J}}}}{b^i_{\mathbf{J_o}}}\int_{S_t}\mathbf{H}\cdot\mathbf{h}^*_{t\mathbf{J}}ds \tag{B.47}$$

It does hold that

$$\mathbf{M}\cdot\int_{\Omega}(\bar{\mathbf{I}}+\frac{1}{\beta^2}\nabla\nabla)G_p\cdot\mathbf{h}^*_{t\mathbf{J}}ds = -\frac{\gamma_{\mathbf{J}}e^{-\gamma_{\mathbf{J}}|u_z|}}{2\beta^2}\mathbf{h}^*_{\mathbf{J}}(\boldsymbol{\rho}')\cdot\mathbf{M} \tag{B.48}$$

for the TEz case, and

$$\mathbf{M}\cdot\int_{\Omega}(\bar{\mathbf{I}}+\frac{1}{\beta^2}\nabla\nabla)G_p\cdot\mathbf{h}^*_{t\mathbf{J}}ds = \frac{e^{-\gamma_{\mathbf{J}}|u_z|}}{2\gamma_{\mathbf{J}}}\mathbf{h}^*_{\mathbf{J}}(\boldsymbol{\rho}')\cdot\mathbf{M} \tag{B.49}$$

for the TMz case. Here Ω denotes S_r or S_t. Thus, for both TEz and TMz cases, one can obtain

$$\int_{\Omega}\boldsymbol{L}(\mathbf{M})\cdot\mathbf{h}^*_{t\mathbf{J}}ds = \int_{S_a}\frac{1}{2Z_{\mathbf{J}}}e^{-\gamma_{\mathbf{J}}|u_z|}\mathbf{h}^*_{\mathbf{J}}(\boldsymbol{\rho}')\cdot\mathbf{M}(\mathbf{r}')ds' \tag{B.50}$$

Assume the planes S_r and S_t are above and below the scatterers, respectively. Substitution of (B.50) into (B.43) and (B.47) yields (4.11) and (4.12).

Next, the derivation of (4.13)-(4.14) is given. The transverse component of incident wave is given by

$$\mathbf{E}^i_t = b^i_{\mathbf{J_o}}e^{\gamma_{\mathbf{J_o}}z}\sqrt{Z_{\mathbf{J_o}}}\mathbf{e}_{t\mathbf{J_o}} \tag{B.51}$$

When the incident wave is the plane wave, the coefficient $b^i_{\mathbf{J}}$ can be found by (B.32) and (B.33).

The transverse component of the total electric field is given by

$$\mathbf{E}_t(z=z_r) = \mathbf{E}^i_t + \mathbf{E}^s_t = b^i_{\mathbf{J_o}}e^{\gamma_{\mathbf{J_o}}z_r}\sqrt{Z_{\mathbf{J_o}}}\mathbf{e}_{t\mathbf{J_o}} + \mathbf{E}^s_t|_{z=z_r} \tag{B.52}$$

where $\mathbf{E}^s_t$ is the transverse component of the scattering field $\mathbf{E}^s$. $\mathbf{E}^s_t$ can be expanded as

$$\mathbf{E}^s_t(z=z_r) = \sum_{\mathbf{J}} a_{\mathbf{J}}e^{-\gamma_{\mathbf{J}}z_r}\sqrt{Z_{\mathbf{J}}}\mathbf{e}_{t\mathbf{J}} \tag{B.53}$$

Using (B.53) and the orthogonality of Floquet's modes yields

$$\int_{S_r} \mathbf{E}^s \cdot \mathbf{e}_{t\mathbf{J}}^* ds = a_{\mathbf{J}} e^{-\gamma_{\mathbf{J}} z_r} \sqrt{Z_{\mathbf{J}}} \tag{B.54}$$

since $\mathbf{E}_t^s \cdot \mathbf{e}_{t\mathbf{J}}^* = \mathbf{E}^s \cdot \mathbf{e}_{t\mathbf{J}}^*$. The reflection coefficient can be found by

$$\Gamma = \frac{a_{\mathbf{J}}}{b_{\mathbf{J_o}}^i} = \frac{e^{\gamma_{\mathbf{J}} z_r}}{b_{\mathbf{J_o}}^i \sqrt{Z_{\mathbf{J}}}} \int_{S_r} \mathbf{E}^s \cdot \mathbf{e}_{t\mathbf{J}}^* ds \tag{B.55}$$

At $z = z_t$,

$$\mathbf{E}_t(z = z_t) = b_{\mathbf{J_o}}^i e^{\gamma_{\mathbf{J_o}} z_t} \sqrt{Z_{\mathbf{J_o}}} \mathbf{e}_{t\mathbf{J_o}} + \mathbf{E}_t^s|_{z=z_t} \tag{B.56}$$

The transverse component of the total electric field can be expanded as

$$\mathbf{E}_t(z = z_t) = \sum_{\mathbf{J}} b_{\mathbf{J}} e^{\gamma_{\mathbf{J}} z_t} \sqrt{Z_{\mathbf{J}}} \mathbf{e}_{t\mathbf{J}} \tag{B.57}$$

Combing (B.56) and (B.57) and using the orthogonality of Floquet modes, one can obtain

$$\delta_{\mathbf{J_o J}} b_{\mathbf{J_o}}^i e^{\gamma_{\mathbf{J_o}} z_t} \sqrt{Z_{\mathbf{J_o}}} + \int_{S_t} \mathbf{E}^s \cdot \mathbf{e}_{t\mathbf{J}}^* ds = b_{\mathbf{J}} e^{\gamma_{\mathbf{J}} z_t} \sqrt{Z_{\mathbf{J}}} \tag{B.58}$$

The transmission coefficient can be found by

$$T = \frac{b_{\mathbf{J}}}{b_{\mathbf{J_o}}^i} = \delta_{\mathbf{J_o J}} + \frac{e^{-\gamma_{\mathbf{J}} z_t}}{b_{\mathbf{J_o}}^i \sqrt{Z_{\mathbf{J}}}} \int_{S_t} \mathbf{E}^s \cdot \mathbf{e}_{t\mathbf{J}}^* ds \tag{B.59}$$

The scattered field is given by

$$\mathbf{E}^s = -j\omega\mu \int_S \mathbf{J}(\mathbf{r}') \cdot [\bar{\mathbf{I}} + \frac{1}{\beta^2} \nabla\nabla] G_p(\mathbf{r}, \mathbf{r}') ds' \tag{B.60}$$

For convenience, $\mathbf{e}_{t\mathbf{J}}$ is rewritten as

$$\mathbf{e}_{t\mathbf{J}} = \mathbf{C}_{\mathbf{J}} e^{-j\mathbf{k}_{\mathbf{J}\parallel} \cdot \boldsymbol{\rho}} \tag{B.61}$$

Using

$$G_p(\mathbf{u}) = \frac{1}{\Omega} \sum_{\mathbf{J}} \frac{e^{-\gamma_{\mathbf{J}} |u_z|}}{2\gamma_{\mathbf{J}}} e^{-j\mathbf{k}_{\mathbf{J}\parallel} \cdot \mathbf{u}} \tag{B.62}$$

one can obtain

$$\int_\Omega G_p \mathbf{e}_{t\mathbf{J}}^* ds = \frac{1}{2\Omega} \int_\Omega \sum_{\mathbf{I}} \frac{e^{-\gamma_{\mathbf{I}} |u_z|}}{\gamma_{\mathbf{I}}} e^{j\mathbf{k}_{\mathbf{I}\parallel} \cdot \boldsymbol{\rho}'} e^{-j\mathbf{k}_{\mathbf{I}\parallel} \cdot \boldsymbol{\rho}} \mathbf{C}_{\mathbf{J}}^* e^{j\mathbf{k}_{\mathbf{J}\parallel} \cdot \boldsymbol{\rho}} ds = \frac{1}{2} \frac{e^{-\gamma_{\mathbf{J}} |u_\perp|}}{\gamma_{\mathbf{J}}} \mathbf{e}_{t\mathbf{J}}^* (\boldsymbol{\rho}') \tag{B.63}$$

Moreover,

$$\begin{aligned}
&\int_\Omega \nabla\nabla G_p \cdot \mathbf{e}^*_{t\mathbf{J}} ds \\
=&\frac{1}{2\Omega}\sum_{\mathbf{I}}(\mp\gamma_{\mathbf{I}}\hat{z} - j\mathbf{k}_{\mathbf{I}\parallel})(\mp\gamma_{\mathbf{I}}\hat{z} - j\mathbf{k}_{\mathbf{I}\parallel})\frac{e^{-\gamma_{\mathbf{I}}|u_z|}}{\gamma_{\mathbf{I}}}e^{j\mathbf{k}_{\mathbf{I}\parallel}\cdot\boldsymbol{\rho}'} \cdot \int_\Omega e^{-j\mathbf{k}_{\mathbf{I}\parallel}\cdot\boldsymbol{\rho}}\mathbf{C}^*_{\mathbf{J}}e^{j\mathbf{k}_{\mathbf{J}\parallel}\cdot\boldsymbol{\rho}}ds \\
=&\frac{e^{-\gamma_{\mathbf{J}}|u_z|}}{2\gamma_{\mathbf{J}}}(\mp\gamma_{\mathbf{J}}\hat{z} - j\mathbf{k}_{\mathbf{J}\parallel})(\mp\gamma_{\mathbf{J}}\hat{z} - j\mathbf{k}_{\mathbf{J}\parallel}) \cdot \mathbf{C}^*_{\mathbf{J}}e^{j\mathbf{k}_{\mathbf{J}\parallel}\cdot\boldsymbol{\rho}'} \\
=&\frac{e^{-\gamma_{\mathbf{J}}|u_z|}}{2\gamma_{\mathbf{J}}}(\mp\gamma_{\mathbf{J}}\hat{z} - j\mathbf{k}_{\mathbf{J}\parallel})(\mp\gamma_{\mathbf{J}}\hat{z} - j\mathbf{k}_{\mathbf{J}\parallel}) \cdot \mathbf{e}^*_{t\mathbf{J}}(\boldsymbol{\rho}')
\end{aligned} \tag{B.64}$$

Thus, for TMz case,

$$\begin{aligned}
&\int_\Omega (\bar{\mathbf{I}} + \frac{1}{\beta^2}\nabla\nabla)G_p \cdot \mathbf{e}^*_{t\mathbf{J}} ds \\
=&\frac{e^{-\gamma_{\mathbf{J}}|u_z|}}{2\gamma_{\mathbf{J}}}\left[\mathbf{e}^*_{t\mathbf{J}}(\boldsymbol{\rho}') + \frac{1}{\beta^2}(\mp\gamma_{\mathbf{J}}\hat{z} - j\mathbf{k}_{\mathbf{J}\parallel})(\mp\gamma_{\mathbf{J}}\hat{z} - j\mathbf{k}_{\mathbf{J}\parallel}) \cdot \mathbf{e}^*_{t\mathbf{J}}(\boldsymbol{\rho}')\right] \\
=&\frac{e^{-\gamma_{\mathbf{J}}|u_z|}}{2\gamma_{\mathbf{J}}\beta^2}\left[\beta^2\mathbf{e}^*_{t\mathbf{J}}(\boldsymbol{\rho}') + (\pm\gamma_{\mathbf{J}}\hat{z} + j\mathbf{k}_{\mathbf{J}\parallel})j\mathbf{k}_{\mathbf{J}\parallel} \cdot \mathbf{e}^*_{t\mathbf{J}}(\boldsymbol{\rho}')\right] \\
=&\frac{e^{-\gamma_{\mathbf{J}}|u_z|}}{2\gamma_{\mathbf{J}}\beta^2}\left[\beta^2\mathbf{e}^*_{t\mathbf{J}}(\boldsymbol{\rho}') + (\pm\gamma_{\mathbf{J}}\hat{z} + j\mathbf{k}_{\mathbf{J}\parallel})|\mathbf{k}_{\mathbf{J}\parallel}|\chi^*_{\mathbf{J}}\right] \\
=&\frac{e^{-\gamma_{\mathbf{J}}|u_z|}}{2\gamma_{\mathbf{J}}\beta^2}\left[(\beta^2 - |\mathbf{k}_{\mathbf{J}\parallel}|^2)\mathbf{e}^*_{t\mathbf{J}} \mp \gamma^2_{\mathbf{J}}\frac{|\mathbf{k}_{\mathbf{J}\parallel}|}{-\gamma_{\mathbf{J}}}\chi^*_{\mathbf{J}}\hat{z}\right] \\
=&-\frac{\gamma_{\mathbf{J}}e^{-\gamma_{\mathbf{J}}|u_z|}}{2\beta^2}(\mathbf{e}^*_{t\mathbf{J}} \pm \frac{|\mathbf{k}_{\mathbf{J}\parallel}|}{-\gamma_{\mathbf{J}}}\chi^*_{\mathbf{J}}\hat{z}) \\
=&-\frac{\gamma_{\mathbf{J}}e^{-\gamma_{\mathbf{J}}|u_z|}}{2\beta^2}(\mathbf{e}^*_{t\mathbf{J}} \pm e^*_{z\mathbf{J}}\hat{z})
\end{aligned} \tag{B.65}$$

For TEz case,

$$\begin{aligned}
&\int_\Omega (\bar{\mathbf{I}} + \frac{1}{\beta^2}\nabla\nabla)G_p \cdot \mathbf{e}^*_{t\mathbf{J}} ds \\
=&\frac{e^{-\gamma_{\mathbf{J}}|u_z|}}{2\gamma_{\mathbf{J}}}\left[\mathbf{e}^*_{t\mathbf{J}}(\boldsymbol{\rho}') + \frac{1}{\beta^2}(-\gamma_{\mathbf{J}}\hat{z} - j\mathbf{k}_{\mathbf{J}\parallel})(-\gamma_{\mathbf{J}}\hat{z} - j\mathbf{k}_{\mathbf{J}\parallel}) \cdot \mathbf{e}^*_{t\mathbf{J}}(\boldsymbol{\rho}')\right] \\
=&\frac{e^{-\gamma_{\mathbf{J}}|u_z|}}{2\gamma_{\mathbf{J}}}\mathbf{e}^*_{t\mathbf{J}}(\boldsymbol{\rho}') \\
=&\frac{e^{-\gamma_{\mathbf{J}}|u_z|}}{2\gamma_{\mathbf{J}}}\mathbf{e}^*_{\mathbf{J}}(\boldsymbol{\rho}')
\end{aligned} \tag{B.66}$$

Therefore, for both TEz and TMz cases, one can obtain

$$\int_\Omega \mathbf{E}^s \cdot \mathbf{e}^*_{t\mathbf{J}} ds = \int_S (-1)\frac{Z_{\mathbf{J}}}{2}e^{-\gamma_{\mathbf{J}}|u_z|}\mathbf{e}^*_{\mathbf{J}}(\boldsymbol{\rho}') \cdot \mathbf{J}(\mathbf{r}')ds' \tag{B.67}$$

since the electric current $\mathbf{J}$ has only the transverse component along the surface S_r or S_t. Substituting (B.67) into (B.55) and (B.59) yields (4.13) and (4.14).

In [33], the induced electric field is obtained by

$$\mathbf{E}^s = \int_S \overline{\mathbf{G}}_{EE}(\mathbf{r},\mathbf{r}')\cdot\mathbf{J}(\mathbf{r}')ds' \tag{B.68}$$

where

$$\overline{\mathbf{G}}_{EE}(\mathbf{r},\mathbf{r}') = \sum_{\mathbf{J}}(-1)\frac{Z_{\mathbf{J}}}{2}e^{-\gamma_{\mathbf{J}}|u_z|}\mathbf{e}_{t\mathbf{J}}(\boldsymbol{\rho})\mathbf{e}^*_{\mathbf{J}}(\boldsymbol{\rho}') \tag{B.69}$$

Actually, from (B.60), one has

$$\overline{\mathbf{G}}_{EE}(\mathbf{r},\mathbf{r}') = -j\omega\mu\left[(\bar{\mathbf{I}}+\frac{1}{\beta^2}\nabla\nabla)G_p\right]_t \tag{B.70}$$

Thus, using (B.62) gives

$$\begin{aligned}\overline{\mathbf{G}}_{EE}(\mathbf{r},\mathbf{r}') &= \sum_{\mathbf{J}}\frac{-j\omega\mu}{\Omega}\frac{e^{-\gamma_{\mathbf{J}}|u_z|}}{2\gamma_{\mathbf{J}}}e^{-j\mathbf{k}_{\mathbf{J}\|}\cdot\boldsymbol{\rho}-\boldsymbol{\rho}'}\left[\bar{\mathbf{I}}_t+\frac{1}{\beta^2}(-j\mathbf{k}_{\mathbf{J}\|})(\mp\gamma_{\mathbf{J}}\hat{\mathbf{z}}-\mathbf{j}\mathbf{k}_{\mathbf{J}\|})\right]\\ &= \sum_{\mathbf{J}}\frac{-j\omega\mu}{\Omega}\frac{e^{-\gamma_{\mathbf{J}}|u_z|}}{2\gamma_{\mathbf{J}}}e^{-j\mathbf{k}_{\mathbf{J}\|}\cdot\boldsymbol{\rho}-\boldsymbol{\rho}'}\\ &\quad\cdot\left[\frac{\mathbf{k}_{\mathbf{J}\|}}{|\mathbf{k}_{\mathbf{J}\|}|}\frac{\mathbf{k}_{\mathbf{J}\|}}{|\mathbf{k}_{\mathbf{J}\|}|}+\frac{\hat{z}\times|\mathbf{k}_{\mathbf{J}\|}|}{|\mathbf{k}_{\mathbf{J}\|}|}\frac{\hat{z}\times|\mathbf{k}_{\mathbf{J}\|}|}{|\mathbf{k}_{\mathbf{J}\|}|}-\frac{1}{\beta^2}j\mathbf{k}_{\mathbf{J}\|}(\mp\gamma_{\mathbf{J}}\hat{\mathbf{z}}-\mathbf{j}\mathbf{k}_{\mathbf{J}\|})\right]\end{aligned} \tag{B.71}$$

Then

$$\overline{\mathbf{G}}_{EE}(\mathbf{r},\mathbf{r}') = \overline{\mathbf{G}}_{EE,1}+\overline{\mathbf{G}}_{EE,2} \tag{B.72}$$

where

$$\begin{aligned}\overline{\mathbf{G}}_{EE,2} &= \sum_{\mathbf{J}}\frac{-j\omega\mu}{\Omega}\frac{e^{-\gamma_{\mathbf{J}}|u_z|}}{2\gamma_{\mathbf{J}}}e^{-j\mathbf{k}_{\mathbf{J}\|}\cdot\boldsymbol{\rho}-\boldsymbol{\rho}'}\frac{\hat{z}\times|\mathbf{k}_{\mathbf{J}\|}|}{|\mathbf{k}_{\mathbf{J}\|}|}\frac{\hat{z}\times|\mathbf{k}_{\mathbf{J}\|}|}{|\mathbf{k}_{\mathbf{J}\|}|}\\ &= -\sum_{\mathbf{J}}\frac{Z_{\mathbf{J}}}{2}e^{-\gamma_{\mathbf{J}}|u_z|}\mathbf{e}_{t\mathbf{J},\mathrm{TE}}(\boldsymbol{\rho})\mathbf{e}^*_{\mathbf{J},\mathrm{TE}}(\boldsymbol{\rho}')\end{aligned} \tag{B.73}$$

$$\begin{aligned}\overline{\mathbf{G}}_{EE,1} &= \sum_{\mathbf{J}}\frac{-j\omega\mu}{\Omega}\frac{e^{-\gamma_{\mathbf{J}}|u_z|}}{2\gamma_{\mathbf{J}}}e^{-j\mathbf{k}_{\mathbf{J}\|}\cdot(\boldsymbol{\rho}-\boldsymbol{\rho}')}\left[\frac{\mathbf{k}_{\mathbf{J}\|}}{|\mathbf{k}_{\mathbf{J}\|}|}\frac{\mathbf{k}_{\mathbf{J}\|}}{|\mathbf{k}_{\mathbf{J}\|}|}-\frac{1}{\beta^2}j\mathbf{k}_{\mathbf{J}\|}(\mp\gamma_{\mathbf{J}}\hat{\mathbf{z}}-\mathbf{j}\mathbf{k}_{\mathbf{J}\|})\right]\\ &= \sum_{\mathbf{J}}\frac{-j\omega\mu}{2}\frac{e^{-\gamma_{\mathbf{J}}|u_z|}}{\gamma_{\mathbf{J}}}\left[\mathbf{e}_{t\mathbf{J},\mathrm{TM}}(\boldsymbol{\rho})\mathbf{e}^*_{\mathbf{J},\mathrm{TM}}(\boldsymbol{\rho}')\left(1-\frac{|\mathbf{k}_{\mathbf{J}\|}|^{\mathbf{2}}}{\beta^2}\right)-\frac{j\mathbf{k}_{\mathbf{J}\|}}{\beta^2\Omega}(\mp\gamma_{\mathbf{J}})e^{-j\mathbf{k}_{\mathbf{J}\|}\cdot\boldsymbol{\rho}-\boldsymbol{\rho}'}\hat{z}\right]\\ &= \sum_{\mathbf{J}}(-1)\frac{Z_{\mathbf{J}}}{2}e^{-\gamma_{\mathbf{J}}|u_z|}\mathbf{e}_{t\mathbf{J},\mathrm{TM}}(\boldsymbol{\rho})\left[\mathbf{e}^*_{t\mathbf{J},\mathrm{TM}}(\boldsymbol{\rho}')\pm e^*_z\hat{z}\right]\end{aligned} \tag{B.74}$$

Since the electric current **J** has only transverse component, one may have

$$\overline{\mathbf{G}}_{EE,1} = -\sum_{\mathbf{J}} \frac{Z_{\mathbf{J}}}{2} e^{-\gamma_{\mathbf{J}}|u_z|} \mathbf{e}_{t\mathbf{J},\mathrm{TM}}(\boldsymbol{\rho}) \mathbf{e}^*_{\mathbf{J},\mathrm{TM}}(\boldsymbol{\rho}') \tag{B.75}$$

Thus, we have

$$\overline{\mathbf{G}}_{EE}(\mathbf{r},\mathbf{r}') = \sum_{\mathbf{J}} (-1) \frac{Z_{\mathbf{J}}}{2} e^{-\gamma_{\mathbf{J}}|u_z|} \mathbf{e}_{t\mathbf{J}}(\boldsymbol{\rho}) \mathbf{e}^*_{\mathbf{J}}(\boldsymbol{\rho}') \tag{B.76}$$

APPENDIX C DERIVATION OF ANALYTICAL FORMULAE FOR PROJECTION ERROR

C.1 Analytical projection error of triangular basis functions

For the triangular basis function $N_m(x)$ and $N_{m\pm 1}$ at $x_m = mh$ and $x_{m\pm 1} = (m \pm 1)h$,

$$\int N_m(x)N_m(x)dx = \int_{x_{m-1}}^{x_m} \left(\frac{x - x_{m-1}}{h}\right)^2 dx + \int_{x_m}^{x_{m+1}} \left(\frac{x_{m+1} - x}{h}\right)^2 dx = \frac{2h}{3} \tag{C.1}$$

$$\int N_m(x)N_{m-1}(x)dx = \int N_m(x)N_{m+1}(x)dx = \int_{x_m}^{x_{m+1}} \frac{x_{m+1} - x}{h}\frac{x - x_m}{h} dx = \frac{h}{6} \tag{C.2}$$

where h is the spacing between two neighboring nodes. And

$$\begin{aligned}\int N_m(x)\text{exp}(jkx)dx &= \int_{x_{m-1}}^{x_m} \frac{x - x_{m-1}}{h}\text{exp}(jkx)dx + \int_{x_m}^{x_{m+1}} \frac{x_{m+1} - x}{h}\text{exp}(jkx)dx \\ &= h\,\text{exp}(jmkh)\text{sinc}^2(kh/2)\end{aligned} \tag{C.3}$$

In (5.8),

$$\begin{aligned}I = \int_{x_{m-1}}^{x_m} \text{Err}^2(x)dx &= \int_{s=0}^{h} \left|1 - d_0\text{exp}[jk(h-s)]\frac{s}{h} - d_0\text{exp}(-jks)\frac{h-s}{h}\right|^2 ds \\ &= \int_{s=0}^{h} 1 + \left|d_0\text{exp}[jk(h-s)]\frac{s}{h} + d_0\text{exp}(-jks)\frac{h-s}{h}\right|^2 \\ &\qquad - 2\,\text{Re}\left(d_0\text{exp}[jk(h-s)]\frac{s}{h} + d_0\text{exp}(-jks)\frac{h-s}{h}\right) ds \\ &= \int_{s=0}^{h} 1 + d_0^2\left[(\frac{s}{h})^2 + (\frac{h-s}{h})^2\right] + 2\,\text{Re}\left(d_0^2\frac{s}{h}\frac{h-s}{h}\text{exp}(jkh)\right) \\ &\qquad - 2\,\text{Re}\left(d_0\text{exp}(jk(h-s))\frac{s}{h} + d_0\text{exp}(-jks)\frac{h-s}{h}\right) ds\end{aligned} \tag{C.4}$$

Here $\text{Re}()$ denotes taking the real part of a complex number. It is easy to get

$$\int_{s=0}^{h} \left(\frac{s}{h}\right)^2 ds = \int_{s=0}^{h} \left(\frac{h-s}{h}\right)^2 ds = h/3 \tag{C.5}$$

$$\int_{s=0}^{h} \frac{s}{h} \exp(-jk(s-h))ds = \frac{1}{h}\left[\frac{h}{-jk} - \frac{1-\exp(jkh)}{(jk)^2}\right] \tag{C.6}$$

$$\int_{s=0}^{h} \exp[-jk(s-h)]ds = \frac{1-\exp(jkh)}{-jk} \tag{C.7}$$

Thus,

$$\begin{aligned} I &= h\left[1+\frac{2d_0^2+d_0^2\cos(kh)}{3}\right] - 2\,\mathrm{Re}\left(\frac{d_0(1-e^{-jkh})}{h}\left(\frac{h}{-jk} - \frac{1-e^{jkh}}{(jk)^2}\right) + d_0\frac{e^{-jkh}-1}{-jk}\right) \\ &= h\left[1+\frac{2+\cos(kh)}{3}d_0^2\right] - 2\,\mathrm{Re}\left(\frac{d_0 e^{-jkh}(e^{jkh}-1)^2}{h(jk)^2}\right) \\ &= h\left[1+\frac{2+\cos(kh)}{3}d_0^2\right] - 2hd_0\mathrm{sinc}^2(kh/2) \\ &= h\left[1-\frac{3\mathrm{sinc}^4(kh/2)}{\cos(kh)+2}\right] \end{aligned} \tag{C.8}$$

Therefore, the RMS error is obtained

$$\mathrm{Err}_{\mathrm{RMS}} = \sqrt{1-\frac{3\mathrm{sinc}^4(kh/2)}{\cos(kh)+2}} \tag{C.9}$$

When N is large, we can get the asymptotical expression

$$\begin{aligned} \mathrm{Err}^2_{\mathrm{RMS}} &= \frac{\cos(2t)+2-3\mathrm{sinc}^4 t}{\cos(2t)+2} \\ &\approx \frac{1-4t^2/2+16t^4/24+2-3(1-t^2/6+t^4/120)^4}{1-4t^2/2+2} \\ &\approx \frac{3-4t^2/2+16t^4/24-3(1-t^2/3+2t^4/45)^2}{3} \\ &\approx \frac{3-4t^2/2+16t^4/24-3(1-2t^2/3+t^4/5)}{3} \\ &= \frac{t^4}{45} \end{aligned} \tag{C.10}$$

where $t = kh/2$. Thus,

$$\mathrm{Err}_{\mathrm{RMS\_ASM}} = \frac{(kh)^2}{12\sqrt{5}} \tag{C.11}$$

C.2 Analytical projection error of second-order basis functions in 1D case

For the mth linear element e with nodes of x_m and x_{m-1}, there are three basis functions of second order

$$N_M^e(\xi_1,\xi_2) = P_I^p(\xi_1)P_J^p(\xi_2) = \begin{cases} (1-\xi_1)(1-2\xi_1), & M=1\,(I=0 \text{ and } J=2) \\ 4\xi_1(1-\xi_1), & M=2\,(I=1 \text{ and } J=1) \\ \xi_1(2\xi_1-1), & M=3\,(I=2 \text{ and } J=0) \end{cases} \tag{C.12}$$

The coordinate transformation is applied

$$x = x_{m-1}\xi_1 + x_m\xi_2, \tag{C.13}$$

where $\xi_1+\xi_2=1$. The local matrix [85] $K^e = [K_{MN}^e]_{3\times 3}$, in which

$$K_{MN}^e = \int N_M^e N_N^e dx = h\int_{\xi_1=0}^{1} N_M^e N_N^e d\xi_1$$

is found to be

$$K^e = h\begin{bmatrix} \frac{2}{15} & \frac{1}{15} & -\frac{1}{30} \\ \frac{1}{15} & \frac{8}{15} & \frac{1}{15} \\ -\frac{1}{30} & \frac{2}{15} & \frac{1}{15} \end{bmatrix} \tag{C.14}$$

Assume the coefficients a_m and b_m of the basis corresponding to the node x_m and the central point of the ith element e. Using the Galerkin method with respect to b_m and a_m, we have two equations

$$\begin{aligned} \frac{1}{15}a_{m-1} + \frac{8}{15}b_m + \frac{1}{15}a_m &= B_1 \\ -\frac{1}{30}a_{m-1} + \frac{1}{15}b_m + \frac{4}{15}a_m + \frac{1}{15}b_{m+1} - \frac{1}{30}a_{m+1} &= B_2 \end{aligned} \tag{C.15}$$

where

$$\begin{aligned} B_1 &= \int_{x=x_{m-1}}^{x_m} \exp(jkx)N_2^e dx \\ &= 4h\exp(jmkh)\int_{\xi_1=0}^{1}\exp(-jkh\xi)\xi_1(1-\xi_1)d\xi_1 \\ &= h\exp\big((m-1/2)jkh\big)\,C_1 \\ C_1 &= \frac{2[\mathrm{sinc}(kh/2)-\cos(kh/2)]}{(kh/2)^2} \end{aligned} \tag{C.16}$$

$$
\begin{aligned}
B_2 &= \int_{x=x_{m-1}}^{x_m} \exp(jkx) N_3^e dx + \int_{x=x_m}^{x_{m+1}} \exp(jkx) N_1^e dx \\
&= h\exp(jmkh) \left[\int_{\xi_1=0}^{1} \exp(-jkh\xi_1)(1-\xi_1)(1-2\xi_1) d\xi_1 + \right. \\
&\qquad \left. \int_{\xi_1=0}^{1} \exp(jkh(1-\xi_1))\xi_1(2\xi_1-1) d\xi_1 \right] \\
&= h\exp(jmkh) \int_{\xi_1=0}^{1} \left[\exp(-jkh\xi_1) + \exp(jkh\xi_1)\right](1-\xi_1)(1-2\xi_1) d\xi_1 \\
&= h\exp(jmkh) \int_{\xi_1=0}^{1} 2\cos(kh\xi_1)(1-\xi_1)(1-2\xi_1) d\xi_1 \\
&= h\exp(jmkh) C_2 \\
C_2 &= \frac{2\left[\cos(kh) + 3 - 4\text{sinc}(kh)\right]}{(kh)^2}
\end{aligned}
\tag{C.17}
$$

It should be noted that the diagonal element in local matrix is doubled in (C.15) since each coefficient has a pair of basis functions on two linear elements. Assume $b_m = d_1 \exp[(m-1/2)jkh]$ and $a_m = d_2 \exp(jmkh)$. Substituting them into (C.15) yields

$$
\begin{aligned}
16d_1 + 4d_2\cos(kh/2) &= 30C_1 \\
4\cos(kh/2)d_1 + \left[8 - 2\cos(kh)\right] d_2 &= 30C_2
\end{aligned}
\tag{C.18}
$$

Thus,

$$
\begin{aligned}
d_1 &= \frac{3}{8 - 4\cos^2 t}\left\{\left[4 - \cos(2t)\right] C_1 - 2\cos t C_2\right\} \\
d_2 &= \frac{3}{8 - 4\cos^2 t}\left[-2\cos t C_1 + 8C_2\right]
\end{aligned}
\tag{C.19}
$$

where $t = kh/2$. Substitution of C_1 and C_2 in (C.16) and (C.17) into the above equation yields

$$
\begin{aligned}
d_1 &= \frac{3\left(5\text{sinc}\, t - 6\cos t + \cos^3 t\right)}{2t^2\left(2 - \cos^2 t\right)} \\
d_2 &= \frac{3\left(3\cos^2 t + 2 - 5\cos t\, \text{sinc}\, t\right)}{t^2\left(2 - \cos^2 t\right)}
\end{aligned}
\tag{C.20}
$$

The square of the error is

$$
\begin{aligned}
\text{Err}^2 &= \left|\exp(jkx) - (a_{i-1}N_1 + b_m N_2 + a_m N_3)\right|^2 \\
&= 1 + |a_{m-1}N_1 + b_m N_2 + a_m N_3|^2 - 2\text{Re}\left((a_{m-1}N_1 + b_m N_2 + a_m N_3)^* \exp(jkx)\right)
\end{aligned}
\tag{C.21}
$$

$$\begin{aligned}\mathrm{Err}^2 &= 1 + |a_{m-1}|^2 N_1^2 + |b_m|^2 N_2^2 + |a_m|^2 N_3^2 - 2\mathrm{Re}\left((a_{m-1}N_1 + b_m N_2 + a_m N_3)^* \exp(jkx) \right. \\ &\quad \left. + 2\mathrm{Re}\left(a_{m-1} b_m^* N_1 N_2 + a_m b_m^* N_2 N_3 + a_{m-1} a_m^* N_1 N_3 \right) \right)\end{aligned} \tag{C.22}$$

Using (C.14),(C.16), and (C.17), we have

$$\frac{\int_{x=x_{m-1}}^{x_m} \mathrm{Err}^2 dx}{h} = 1 + \frac{8}{15} d_1^2 + \frac{4}{15} d_2^2 - \frac{1}{15} d_2^2 \cos(2t) + \frac{4}{15} d_1 d_2 \cos t - 2(d_1 C_1 + d_2 C_2) \tag{C.23}$$

Thus, the RMS error is obtained by substituting d_1, d_2, C_1, and C_2 into the above equation

$$\mathrm{Err}_{\mathrm{RMS}} = \sqrt{\frac{\mathrm{E_n}}{\mathrm{E_d}}} \tag{C.24}$$

where

$$\begin{aligned}\mathrm{E_n} &= (6t^2 - 30)\cos^4 t - 30t \sin t \cos^3 t + (33t^2 + 15 + t^6)\cos^2 t \\ &\quad - 30t \sin(2t) - 2t^6 + 15 + 6t^2 \\ \mathrm{E_d} &= t^6(-2 + \cos^2 t)\end{aligned} \tag{C.25}$$

C.3 Analytical projection error of basis functions on rectangular elements

For the element shown in Fig. 5.4, the local coefficient matrix [85] $[K_{MN}^e]_{4\times4}$, in which $K_{MN}^e = \iint_{\Delta s} \mathbf{S}_M \cdot \mathbf{S}_N ds$, is given by

$$K^e = \frac{\Delta s}{6} \begin{bmatrix} 2 & 0 & 1 & 0 \\ 0 & 2 & 0 & 1 \\ 1 & 0 & 2 & 0 \\ 0 & 1 & 0 & 2 \end{bmatrix} \tag{C.26}$$

The local source matrix $[B_M^e]_{4\times1}$, in which $B_M^e = \iint_{\Delta s} \mathbf{S}_M \cdot \mathbf{J} ds$, is given by

$$B^e = \Delta s \exp\left(j(n-1)\beta_1 + j(m-1)\beta_2 \right) \begin{bmatrix} V_1 \frac{\exp(j\beta_2)-1}{j\beta_2} \, \frac{\exp(j\beta_1)-j\beta_1-1}{(j\beta_1)^2} \\ V_2 \frac{\exp(j\beta_1)-1}{j\beta_1} \, \frac{\exp(j\beta_2)-j\beta_2-1}{(j\beta_2)^2} \\ V_1 \frac{\exp(j\beta_2)-1}{j\beta_2} \, \frac{j2\beta_1 \exp(j2\beta_1)-\exp(j\beta_1)+1}{(j\beta_1)^2} \\ V_2 \frac{\exp(j\beta_1)-1}{j\beta_1} \, \frac{j\beta_2 \exp(j\beta_2)-\exp(j\beta_2)+1}{(j\beta_2)^2} \end{bmatrix} \tag{C.27}$$

It should be noted that each coefficient corresponds to a pair of basis functions and the local matrix need to be assembled to achieve the (5.23). In (5.26),

$$\begin{aligned}\mathrm{Err}^2 &= |\tilde{\mathbf{J}}-\mathbf{J}|^2 = (\tilde{\mathbf{J}}-\mathbf{J})\cdot(\tilde{\mathbf{J}}-\mathbf{J})^* \\ &= |\tilde{\mathbf{J}}|^2 + |\mathbf{J}|^2 - 2\mathrm{Re}\left(\tilde{\mathbf{J}}^* - \mathbf{J}\right) \\ &= |a_{m\,n-1}|^2\mathbf{S}_1\cdot\mathbf{S}_1 + |a_{m\,n}|^2\mathbf{S}_3\cdot\mathbf{S}_3 + |b_{m-1\,n}|^2\mathbf{S}_2\cdot\mathbf{S}_2 + |b_{m\,n}|^2\mathbf{S}_4\cdot\mathbf{S}_4 \\ &\quad + 2\mathrm{Re}\left(a^*_{m\,n-1}a_{m\,n}\mathbf{S}_1\cdot\mathbf{S}_3 + b^*_{m-1\,n}b_{m\,n}\mathbf{S}_2\cdot\mathbf{S}_4\right) + |\mathbf{J}|^2 \\ &\quad - 2\mathrm{Re}\left(a^*_{m\,n-1}\mathbf{S}_1\cdot\mathbf{J} + a^*_{m\,n}\mathbf{S}_3\cdot\mathbf{J} + b^*_{m-1\,n}\mathbf{S}_2\cdot\mathbf{J} + b^*_{m\,n}\mathbf{S}_4\cdot\mathbf{J}\right)\end{aligned} \tag{C.28}$$

Performing the integral of Err^2 over the rectangular element and applying (C.26) and (C.27) to it yields

$$\begin{aligned}\frac{\iint_{\Delta s}\mathrm{Err}^2 ds}{\Delta s} &= \frac{1}{3}\left[|a_{m\,n-1}|^2 + |a_{m\,n}|^2 + |b_{m-1\,n}|^2 + |b_{m\,n}|^2 + \mathrm{Re}\left(a^*_{m\,n-1}a_{m\,n} + b^*_{m-1\,n}b_{m\,n}\right)\right] \\ &\quad + |\hat{z}\times(\hat{k}\times\hat{p})|^2 - \frac{2}{\Delta s}\mathrm{Re}\left(a^*_{m\,n-1}B^e_1 + a^*_{m\,n}B^e_3 + b^*_{m-1\,n}B^e_2 + b^*_{m\,n}B^e_4\right)\end{aligned} \tag{C.29}$$

Since

$$a^*_{m\,n-1}B^e_1 = d^*_1V_1\frac{\exp(j\beta_2)-1}{j\beta_2}\,\frac{\exp(j\beta_1)-j\beta_1-1}{(j\beta_1)^2}\exp(j\beta_1)\Delta s \tag{C.30}$$

$$a^*_{m\,n}B^e_3 = d^*_1V_1\frac{\exp(j\beta_2)-1}{j\beta_2}\,\frac{j2\beta_1\exp(j2\beta_1)-\exp(j\beta_1)+1}{(j\beta_1)^2}\Delta s \tag{C.31}$$

$$b^*_{m-1\,n}B^e_2 = d^*_2V_2\frac{\exp(j\beta_1)-1}{j\beta_1}\,\frac{\exp(j\beta_2)-j\beta_2-1}{(j\beta_2)^2}\exp(j\beta_2)\Delta s \tag{C.32}$$

$$b^*_{m\,n}B^e_4 = d^*_2V_2\frac{\exp(j\beta_1)-1}{j\beta_1}\,\frac{j\beta_2\exp(j\beta_2)-\exp(j\beta_2)+1}{(j\beta_2)^2}\Delta s \tag{C.33}$$

we have

$$\begin{aligned}a^*_{m\,n-1}B^e_1 + a^*_{m\,n}B^e_3 &= d^*_1d_1\left[4+2\cos(\beta_1)\right]/6 = |d_1|^2\left[4+2\cos(\beta_1)\right]\Delta s/6 \\ b^*_{m-1\,n}B^e_2 + b^*_{m\,n}B^e_4 &= d^*_2d_2\left[4+2\cos(\beta_2)\right]/6 = |d_2|^2\left[4+2\cos(\beta_2)\right]\Delta s/6\end{aligned} \tag{C.34}$$

Thus, from (C.29), we have

$$\begin{aligned}\frac{\iint_{\Delta s}\mathrm{Err}^2 ds}{\Delta s} &= \frac{1}{3}\left[2(|d_1|^2+|d_2|^2) + |d_1|^2\cos(\beta_1) + |d_2|^2\cos(\beta_2)\right] + \left|\hat{z}\times(\hat{k}\times\hat{p})\right|^2 \\ &\quad - \frac{1}{3}\left\{|d_1|^2\left[4+2\cos(\beta_1)\right] + |d_2|^2\left[4+2\cos(\beta_2)\right]\right\} \\ &= \frac{1}{3}\left\{3|\hat{z}\times(\hat{k}\times\hat{p})|^2 - |d_1|^2\left[2+\cos(\beta_1)\right] - |d_2|^2\left[2+\cos(\beta_2)\right]\right\}\end{aligned} \tag{C.35}$$

Therefore, the RMS error is readily obtained

$$\mathrm{Err}^2_{RMS} = 1 - \left\{|d_1|^2[2+\cos(\beta_1)] + |d_2|^2[2+\cos(\beta_2)]\right\} \Big/ \left(3|\hat{z}\times(\hat{k}\times\hat{p})|^2\right) \tag{C.36}$$

In addition, we have

$$\begin{aligned}
|\hat{z}\times(\hat{k}\times\hat{p})|^2 &= 1 \\
V_1 &= -\cos\phi_i \\
V_2 &= \sin\phi_i \\
|d_1|^2 &= \frac{36\cos^2(\phi_i)}{[4+2\cos(\beta_1)]^2}\mathrm{sinc}^2(\beta_2/2)\mathrm{sinc}^4(\beta_1/2) \\
|d_2|^2 &= \frac{36\sin^2(\phi_i)}{[4+2\cos(\beta_2)]^2}\mathrm{sinc}^2(\beta_1/2)\mathrm{sinc}^4(\beta_2/2)
\end{aligned} \tag{C.37}$$

for θ-polarization and

$$\begin{aligned}
|\hat{z}\times(\hat{k}\times\hat{p})|^2 &= \cos^2\theta_i \\
V_1 &= \cos\theta_i\sin\phi_i \\
V_2 &= \cos\theta_i\cos\phi_i \\
|d_1|^2 &= \frac{36\cos^2(\theta_i)\sin^2(\phi_i)}{[4+2\cos(\beta_1)]^2}\mathrm{sinc}^2(\beta_2/2)\mathrm{sinc}^4(\beta_1/2) \\
|d_2|^2 &= \frac{36\cos^2(\theta_i)\cos^2(\phi_i)}{[4+2\cos(\beta_2)]^2}\mathrm{sinc}^2(\beta_1/2)\mathrm{sinc}^4(\beta_2/2)
\end{aligned} \tag{C.38}$$

for ϕ-polarization. Substitution of the above expressions into and simplification of (C.36) yields (5.29) and (5.30).

C.4 Analytical projection error of basis functions on one-directional mesh

The triangular element is shown in Figure C.1. The triangular element in xy-plane is transformed into a simplex triangular element in $\xi_1\xi_2$-plane by the coordinate transformation

$$\mathbf{r} = \mathbf{r}_1\xi_1 + \mathbf{r}_2\xi_2 + \mathbf{r}_3\xi_3 \tag{C.39}$$

where $\xi_1+\xi_2+\xi_3 = 1$. The curl-conforming basis functions are expressed by

$$\begin{aligned}
\mathbf{N}_1 &= (\xi_2\nabla\xi_3 - \xi_3\nabla\xi_2)l_1 \\
\mathbf{N}_2 &= (\xi_3\nabla\xi_1 - \xi_1\nabla\xi_3)l_2 \\
\mathbf{N}_3 &= (\xi_1\nabla\xi_2 - \xi_2\nabla\xi_1)l_3
\end{aligned} \tag{C.40}$$

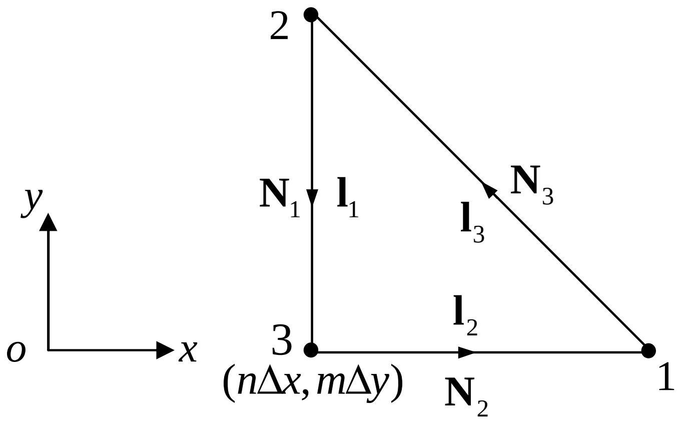

Figure C.1 The curl-conforming basis functions on triangular elements.

where $\nabla\xi_1 = \hat{n}\times\mathbf{l}_1/\mathcal{J}$, $\nabla\xi_2 = \hat{n}\times\mathbf{l}_2/\mathcal{J}$, $\hat{n} = \mathbf{l}_1\times\mathbf{l}_2/\mathcal{J}$, $\mathcal{J} = |\mathbf{l}_1\times\mathbf{l}_2|$, $\mathbf{l}_1 = \mathbf{r}_3 - \mathbf{r}_2$, $\mathbf{l}_2 = \mathbf{r}_1 - \mathbf{r}_3$, and $\mathbf{l}_3 = -(\mathbf{l}_1 + \mathbf{l}_2)$.

The divergence-conforming basis functions, which are known as the RWG basis functions in electromagnetics, are

$$\mathbf{S}_M = \hat{z}\times\mathbf{N}_M \ (M = 1, 2, 3) \tag{C.41}$$

For the one-directional mesh, $\Delta x = \Delta y = h$. The local coefficient matrix $[K^e_{MN}]_{3\times 3}$, in which $K^e_{MN} = \iint_{\Delta s}\mathbf{S}_M\cdot\mathbf{S}_N ds$, is given by

$$K^e = \frac{\mathcal{J}}{6}\begin{bmatrix} 2 & -1 & 0 \\ -1 & 2 & 0 \\ 0 & 0 & 2 \end{bmatrix} \tag{C.42}$$

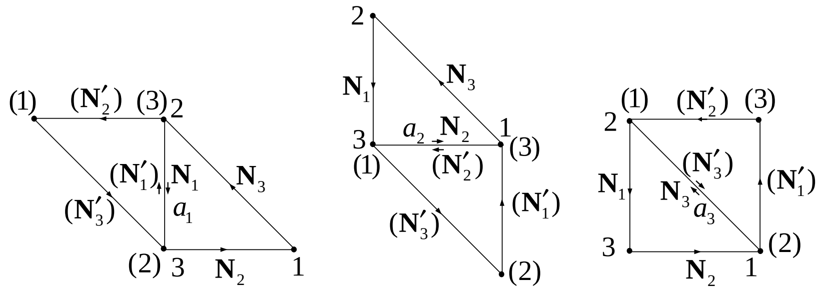

(a) Edge1 (b) Edge 2 (c) Edge 3

Figure C.2 The coefficient on each edge and corresponding triangular elements

As shown in Figure C.2, each coefficient corresponds to a pair of basis functions associated with two triangular elements. Thus, the diagonal element in the local matrix should be doubled when using the Galerkin method.

The interaction between the current and the divergence-conforming basis functions of a_1 is

$$\begin{aligned}\bar{I}_1 &= \iint_{\Delta s_1} \mathbf{S}_1 \cdot \mathbf{J} ds - \iint_{\Delta s_2} \mathbf{S}_1^{'} \cdot \mathbf{J} ds \\ &= \iint_{\Delta s_1} (\xi_2 \nabla \xi_3 - \xi_3 \nabla \xi_2) l_1 \cdot (\mathbf{J} \times \hat{n}) ds - \iint_{\Delta s_2} (\xi_2^{'} \nabla \xi_3^{'} - \xi_3^{'} \nabla \xi_2^{'}) l_1 \cdot (\mathbf{J} \times \hat{n}) ds\end{aligned} \tag{C.43}$$

Using $\nabla\xi_1 = -\nabla\xi_1^{'}$, $\nabla\xi_2 = -\nabla\xi_2^{'}$, and the coordinate transformation (C.39), we have

$$\begin{aligned}\bar{I}_1 = &\int\limits_{\xi_1=0}^{1} \int\limits_{\xi_2=0}^{1-\xi_1} (\xi_2 \nabla \xi_3 - \xi_3 \nabla \xi_2) l_1 \cdot (\hat{k} \times \hat{p}) \exp(j\beta_1 \xi_1 + j\beta_2 \xi_2) \exp(jn\beta_1 + jm\beta_2) l_1 \mathcal{J} d\xi_2 d\xi_1 \\ + &\int\limits_{\xi_1=0}^{1} \int\limits_{\xi_2=0}^{1-\xi_1} (\xi_2 \nabla \xi_3 - \xi_3 \nabla \xi_2) l_1 \cdot (\hat{k} \times \hat{p}) \exp\left(-j(\beta_1 \xi_1 + \beta_2 \xi_2) + j\beta_2\right) \exp(jn\beta_1 + jm\beta_2) l_1 \mathcal{J} d\xi_2 d\xi_1\end{aligned} \tag{C.44}$$

where $\beta_1 = kh \sin\theta_i \cos\phi_i$ and $\beta_2 = kh \sin\theta_i \sin\phi_i$.

Let

$$\begin{aligned}V_1 &= h\ \nabla\xi_1 \cdot (\hat{k} \times \hat{p}) \\ V_2 &= h\ \nabla\xi_2 \cdot (\hat{k} \times \hat{p}).\end{aligned} \tag{C.45}$$

Thus,

$$\bar{I}_1 = \mathcal{J}\ e^{jn\beta_1 + jm\beta_2} \left(E_1 + E_1^{*} e^{j\beta_2} \right) \tag{C.46}$$

where

$$\begin{aligned}E_1 &= -V_1 I_{11}(j\beta_1, j\beta_2) - V_2 I_{12}(j\beta_1, j\beta_2) \\ I_{11}(j\beta_1, j\beta_2) &= \int\limits_{\xi_1=0}^{1} \int\limits_{\xi_2=0}^{1-\xi_1} \xi_2 \exp(j\beta_1 \xi_1 + j\beta_2 \xi_2) d\xi_2 d\xi_1 \\ &= \frac{e^{x_1 - x_2} - (x_1 - x_2) - 1}{(x_1 - x_2)^2} \frac{e^{x_2}}{x_2} - \frac{1}{x_2^2} \left[e^{x_2} \frac{e^{x_1 - x_2} - 1}{x_1 - x_2} - \frac{e^{x_1} - 1}{x_1} \right]\end{aligned}$$

$$\begin{aligned} I_{12}(j\beta_1, j\beta_2) &= \int\limits_{\xi_1=0}^{1} \int\limits_{\xi_2=0}^{1-\xi_1} (1-\xi_1)\mathrm{exp}(j\beta_1\xi_1 + j\beta_2\xi_2)d\xi_2 d\xi_1 \\ &= \frac{e^{x_1-x_2} - (x_1-x_2) - 1}{(x_1-x_2)^2}\frac{e^{x_2}}{x_2} - \frac{1}{x_1x_2}\left[1 - \frac{e^{x_1}-1}{x_1}\right] \end{aligned}$$

Similarly,

$$\begin{aligned} \bar{I}_2 &= \iint_{\Delta s_1} \mathbf{S}_2 \cdot \mathbf{J} ds - \iint_{\Delta s_2} \mathbf{S}_2^{'} \cdot \mathbf{J} ds \\ &= \mathcal{J}\ e^{jn\beta_1 + jm\beta_2}\left(E_2 + E_2^* e^{j\beta_1}\right) \end{aligned} \tag{C.47}$$

$$\begin{aligned} \bar{I}_3 &= \iint_{\Delta s_1} \mathbf{S}_3 \cdot \mathbf{J} ds - \iint_{\Delta s_2} \mathbf{S}_3^{'} \cdot \mathbf{J} ds \\ &= \mathcal{J}\ e^{jn\beta_1 + jm\beta_2}\left[E_3 + E_3^* e^{j(\beta_1 + \beta 2)}\right] \end{aligned} \tag{C.48}$$

where

$$\begin{aligned} E_2 &= V_1 I_{21}(j\beta_1, j\beta_2) + V_2 I_{22}(j\beta_1, j\beta_2) \\ E_3 &= \sqrt{2}\left[-V_1 I_{11}(j\beta_1, j\beta_2) + V_2 I_{22}(j\beta_1, j\beta_2)\right] \end{aligned}$$

$$\begin{aligned} I_{21}(j\beta_1, j\beta_2) &= \int\limits_{\xi_1=0}^{1} \int\limits_{\xi_2=0}^{1-\xi_1} (1-\xi_2)\ \mathrm{exp}(j\beta_1\xi_1 + j\beta_2\xi_2)d\xi_2 d\xi_1 \\ &= I_{12}(j\beta_2, j\beta_1) \\ I_{22}(j\beta_1, j\beta_2) &= \int\limits_{\xi_1=0}^{1} \int\limits_{\xi_2=0}^{1-\xi_1} \xi_1 \mathrm{exp}(j\beta_1\xi_1 + j\beta_2\xi_2)d\xi_2 d\xi_1 \\ &= I_{11}(j\beta_2, j\beta_1) \end{aligned}$$

Assume $a_1 = d_1 e^{jn\beta_1 + jm\beta_2}$, $a_2 = d_2 e^{jn\beta_1 + jm\beta_2}$, and $a_3 = d_3 e^{jn\beta_1 + jm\beta_2}$. Using Galerkin method, we will obtain

$$\begin{aligned} \mathcal{J}\left[\frac{2}{3}\ d_1 e^{jn\beta_1 + jm\beta_2} - \frac{1}{6}\ d_2 e^{jn\beta_1 + jm\beta_2} - \frac{1}{6} d_2 e^{jn\beta_1 + jm\beta_2} e^{-j\beta_1 + j\beta_2}\right] &= \bar{I}_1 \\ \mathcal{J}\left[\frac{2}{3}\ d_2 e^{jn\beta_1 + jm\beta_2} - \frac{1}{6}\ d_2 e^{jn\beta_1 + jm\beta_2} - \frac{1}{6} d_2 e^{jn\beta_1 + jm\beta_2} e^{j\beta_1 - j\beta_2}\right] &= \bar{I}_2 \\ \frac{2}{3}\mathcal{J}\ d_3 e^{jn\beta_1 + jm\beta_2} &= \bar{I}_3 \end{aligned} \tag{C.49}$$

From the above equation, we have

$$\begin{aligned}
d_1 &= \frac{9}{4-\cos^2(\frac{\beta_1-\beta_2}{2})}\left[\frac{2}{3}I_1 + \frac{1}{6}\left(1+e^{-j\beta_1+j\beta_2}\right)I_2\right] \\
d_2 &= \frac{9}{4-\cos^2(\frac{\beta_1-\beta_2}{2})}\left[\frac{2}{3}I_2 + \frac{1}{6}\left(1+e^{j\beta_1-j\beta_2}\right)I_1\right] \\
d_3 &= \frac{2}{3}I_3
\end{aligned} \tag{C.50}$$

where $I_M = \bar{I}_M\left[\exp(jn\beta_1 + jm\beta_2)\mathcal{J}\right]^{-1}$ $(M = 1, 2, 3)$. The square of the error is

$$\begin{aligned}
\mathrm{Err}^2 &= \left|\sum_{M=1}^{3} a_M \mathbf{S}_M - \mathbf{J}\right|^2 \\
&= \left(\sum_{M=1}^{3} a_M \mathbf{S}_M - \mathbf{J}\right)\cdot\left(\sum_{M=1}^{3} a_M^* \mathbf{S}_M - \mathbf{J}^*\right) \\
&= \sum_{M=1}^{3}\left(|a_M|^2|\mathbf{S}_M|^2\right) + 2\mathrm{Re}\left(a_1a_3^*\mathbf{S}_1\cdot\mathbf{S}_3 + a_1a_2^*\mathbf{S}_1\cdot\mathbf{S}_2 + a_2a_3^*\mathbf{S}_2\cdot\mathbf{S}_3\right) \\
&\quad + |\mathbf{J}|^2 - 2\mathrm{Re}\left(\sum_{M=1}^{3} a_M^*\mathbf{S}_M\cdot\mathbf{J}\right)
\end{aligned} \tag{C.51}$$

Performing the integral of Err^2 over the triangular element yields

$$\frac{\iint_{\Delta s}\mathrm{Err}^2 ds}{\mathcal{J}} = \frac{1}{3}\sum_{M=1}^{3}|a_M|^2 - \frac{1}{3}\mathrm{Re}\left(a_1a_2^*\right) + \frac{1}{2}|\hat{z}\times(\hat{k}\times\hat{p})|^2 - 2\mathrm{Re}\left(\sum_{M=1}^{3} a_M^* E_M e^{jn\beta_1+jm\beta_2}\right) \tag{C.52}$$

The square of RMS error is readily obtained

$$\begin{aligned}
{\mathrm{Err}_{\mathrm{RMS}}}^2 &= \frac{\iint_{\Delta s}\mathrm{Err}^2 ds}{\iint_{\Delta s}|\hat{z}\times(\hat{k}\times\hat{p})|^2 ds} \\
&= 1 + \left\{\frac{2}{3}\sum_{M=1}^{3}|a_M|^2 - \frac{2}{3}\mathrm{Re}\left(a_1a_2^*\right) - 4\mathrm{Re}\left(\sum_{M=1}^{3} a_M^* E_M e^{jn\beta_1+jm\beta_2}\right)\right\}\Big/\ |\hat{z}\times(\hat{k}\times\hat{p})|^2
\end{aligned} \tag{C.53}$$

Using the relationship between a_M and d_M, we have

$${\mathrm{Err}_{\mathrm{RMS}}}^2 = 1 + \left\{\frac{2}{3}\sum_{M=1}^{3}|d_M|^2 - \frac{2}{3}\mathrm{Re}\left(d_1d_2^*\right) - 4\mathrm{Re}\left(\sum_{M=1}^{3} d_M^* E_M\right)\right\}\Big/\ |\hat{z}\times(\hat{k}\times\hat{p})|^2 \tag{C.54}$$

It is found

$$\sum_{M=1}^{3}|d_M|^2-\frac{2}{3}\mathrm{Re}\left(d_1d_2^*\right)=3\mathrm{Re}\left(\sum_{M=1}^{3}d_M^*E_M\right) \tag{C.55}$$

Thus,

$$\mathrm{Err_{RMS}}^2=1-\frac{2}{3}\left[\sum_{M=1}^{3}|d_M|^2-\mathrm{Re}(d_1d_2^*)\right]\bigg/|\hat{z}\times(\hat{k}\times\hat{p})|^2 \tag{C.56}$$

In addition,

$$\begin{aligned}
|\hat{z}\times(\hat{k}\times\hat{p})|^2 &= \begin{cases} 1, & \theta-\text{pol.}\\ \cos^2\theta_i, & \phi-\text{pol.}\end{cases}\\
V_1 &= \begin{cases} \sin\phi_i, & \theta\text{-pol.}\\ \cos\theta_i\cos\phi_i, & \phi\text{-pol.}\end{cases}\\
V_2 &= \begin{cases} -\cos\phi_i, & \theta\text{-pol.}\\ \cos\theta_i\sin\phi_i, & \phi\text{-pol.}\end{cases}
\end{aligned} \tag{C.57}$$

Using (C.56), (C.57) and the relationship between d_M and I_M $(M=1,2,3)$, we will get

$$\mathrm{Err}^2=1-\frac{6}{4-\cos^2(\beta_1-\beta_2)}\left[|I_1|^2+|I_2|^2+\mathrm{Re}\left(I_1^*I_2\exp(-j\beta_1+j\beta_2)\right)\right]-\frac{3}{2}|I_3|^2 \tag{C.58}$$

and for ϕ-polarization,

$$\mathrm{Err}^2=1-\left\{\frac{6}{4-\cos^2(\beta_1-\beta_2)}\left[|I_1|^2+|I_2|^2+\mathrm{Re}\left(I_1^*I_2\exp(-j\beta_1+j\beta_2)\right)\right]-\frac{3}{2}|I_3|^2\right\}\bigg/\cos^2\theta_i \tag{C.59}$$

Using $I_1^*\exp(j\beta_2)=I_1$, $I_2\exp(-j\beta_1)=I_2^*$, and $\mathrm{Re}(I_1I_2^*)=\left(|I_1+I_2|^2-|I_1|^2-|I_2|^2\right)\big/2$, we can obtain (5.35) and (5.36).

Bibliography

[1] E. Yablonovitch, “Inhibited spontaneous emission in solid-state physics and electronics,” *Phys. Rev. Lett.*, vol. 58, pp. 2059-2062, May 1987.

[2] E. Yablonovitch, T. J. Gmitter, and K. M. Leung, “Photonic band structure: The face-centered-cubic case employing nonspherical atoms,” *Phys. Rev. Lett.*, vol. 67, pp. 2295-2298, May 1991.

[3] R. E. Collin, *Field Theory of Guided Waves*, 2nd ed. New York: Wiley-Interscience, 1991.

[4] J. B. Pendry, A. J. Holden, W. J. Stewart, and I. Youngs, “Extremely low frequency plasmons in metallic mesostructures,” *Phys. Rev. Lett.*, vol. 76, pp. 4773-4776, June 1996.

[5] J. B. Pendry, A. J. Holden, D. J. Robbins, and W. J. Stewart, “Magnetism from conductors and enhanced nonlinear phenomena,” *IEEE Trans. Microwave Theory Tech.*, vol. 47, no. 11, pp. 2075-2084, Nov. 1999.

[6] D. R. Smith, W. J. Padilla, D. C. Vier, S. C. Nemat-Nasser, and S. Schultz, “Composite medium with simultaneously negative permeability and permittivity,” *Phys. Rev. Lett.*, vol. 84, pp. 4184-4187, May 2000.

[7] D. R. Smith, J. B. Pendry, and M. C. K. Wiltshire, “Metamaterials and negative refractive index,” *Science*, vol. 305, pp. 788-792, Aug. 2004.

[8] T. K. Wu, *Frequency Selective Surface and Grid Array*, New York: John Wiley, 1995.

[9] R. Mittra, C. H. Chan, and T. Cwik, “Techniques for analyzing frequency selective surfaces-a review,” *Proc. IEEE*, vol.76, no. 12, pp. 1593-1615, Dec. 1988.

[10] D. Sievenpiper, L. Zhang, R. F. J. Broas, N. G. Alexopolous, and E. Yablonovitch, "High-impedance electromagnetic surfaces with a forbidden frequency band," *IEEE Trans. Microwave Theory Tech.*, vol. 47, no. 11, pp. 2059-2074, Sept. 1999.

[11] H.-Y. D. Yang and J. Wang, "Surface waves of printed antennas on planar artificial periodic dielectric structures," *IEEE Trans. Antennas Propag.*, vol. 49, no. 3, pp. 444-450, Mar. 2001.

[12] K. Agi, M. Mojahedi, B. Minhas, E. Schamiloglu, and K. J. Malloy, "The effects of an electromagnetic crystal substrate on a microstrip patch antenna," *IEEE Trans. Antennas Propag.*, vol. 50, no. 4, pp. 451-456, April 2002.

[13] A. Pirhadi, M. Hakkak, F. Keshmiri, and R. K. Baee, "Design of compact dual band high directive electromagnetic bandgap (EBG) resonator antenna using artificial magnetic conductor," *IEEE Trans. Antennas Propag.*, vol. 55, no. 6, pp. 1682-1690, June 2007.

[14] K. M. Ho, C. T. Chan, and C. M. Soukoulis,"Existence of a photonic gap in periodic dielectric structures," *Phys. Rev. Lett.*, vol. 65, pp. 3152-3155, Dec. 1990.

[15] H. S. Sozuer, J.W. Haus, and R. Inguva, "Photonic bands: Convergence problems with the plane-wave method," *Phys. Rev. B, Condens. Matter*, vol. 45, pp. 13 962-13 972, June 1992.

[16] C. T. Chan, Q. L. Yu, and K. M. Ho, "Order-N spectral method for electromagnetic waves," *Phys. Rev. B, Condens Matter*, vol. 51, pp. 16 635-16 642, 1995.

[17] J. B. Pendry and A. MacKinnon, "Calculation of photon dispersion relations," *Phys. Rev. Lett.*, vol. 69, pp. 2772-2775, 1992.

[18] J. B. Pendry, "Calculating photonic band structure," *J. Phys.: Condens. Matter 8*, pp. 1085-1108, 1996.

[19] M. G. Silveirinha and C. A. Fernandes, "Efficient calculation of the band structure of artificial materials with cylindrical metallic inclusions," *IEEE Trans. Microwave Theory Tech.*, vol. 51, no. 5, pp. 1460-1466, May 2003.

[20] M. G. Silveirinha and C. A. Fernandes, “A hybrid method for the efficient calculation of the band structure of 3-D metallic crystals,” *IEEE Trans. Microwave Theory Tech.*, vol. 52, no. 3, pp. 889-902, Mar. 2004.

[21] H.-Y. D. Yang, “Finite difference analysis of 2-D photonic crystals,” *IEEE Trans. Microwave Theory Tech.*, vol. 42, no. 12, pp. 2688-2695, Dec. 1996.

[22] C. C. Chen, “Transmission through a conducting screen perforated periodically with apertures,” *IEEE Trans. Microwave Theory Tech.*, vol. 18, no. 9, pp. 627-632, Sept. 1970.

[23] C. C. Chen, “Scattering by a two-dimensional periodic array of conducting plates,” *IEEE Trans. Antennas Propag.*, vol. 18, no. 5, pp. 660- 665, Sept. 1970.

[24] C. C. Chen, “Diffraction of electromagnetic waves by a conducting screen perforated periodically with cirular holes,” *IEEE Trans. Microwave Theory Tech.*, vol. 19, no. 5, pp. 475-481, May 1971.

[25] I. Bardi, R. Remski, D. Perry, and Z. Cendes, “Plane wave scattering from frequency-selective surfaces by the finite-element method,” *IEEE Trans. Magn.*, vol. 38, no. 2, pp. 641-644, Mar. 2002.

[26] G. Pelosi, A. Cocchi, and A. Monorchio, “A hybrid FEM-based procedure for the scattering from photonic crystals illuminated by a Gaussian beam,” *IEEE Trans. Antennas Propag.*, vol. 48, no. 6, pp. 973-980, June 2000.

[27] M. Bozzi, L. Perregrini, J. Weinzierl, and C. Winnewisser, “Efficient analysis of quasi-optical filters by a hybrid MoM/BI-RME method,” *IEEE Trans. Antennas Propag.*, vol. 49, no. 7, pp. 1054-1064, July 2001.

[28] S. D. Gedney, J. F. Lee, and R. Mittra, “A combined FEM/MoM approach to analyze the plane wave diffraction by arbitrary gratings,” *IEEE Trans. Microwave Theory Tech.*, vol. 40, no. 2, pp. 363-370, Feb. 1992.

[29] T. F. Eibert, J. L. Volakis, D. R. Wilton, and D. R. Jackson, “Hybrid FE/BI modeling of 3-D doubly periodic structures utilizing triangular prismatic elements and an MPIE formulation accelereted by the Ewald Transformation,” *IEEE Trans. Antennas Propag.*, vol. 47, no. 5, pp. 843-850, May 1999.

[30] R. Pous and D. M. Pozar, “A frequency-selective surface using aperture-coupled microstrip patches,” *IEEE Trans. Antennas Propag.*, vol. 39, no. 12, pp. 1763-1769, Dec. 1991.

[31] C. Wan and J. A. Encinar, “Efficient computation of generalized scattering matrix for analyzing multilayered periodic structures,” *IEEE Trans. Antennas Propag.*, vol. 43, no. 11, pp. 1233-1242, Nov. 1995.

[32] A. W. Mathis and A. F. Peterson, “Efficient electromagnetic analysis of a doubly infinite array of rectangular apertures,” *IEEE Trans. Antennas Propag.*, vol. 46, no. 1, pp. 46-54, Jan. 1998.

[33] I. Stevanović, Pedro Crespo-Valero, K. Blagović, F. Bongard, and J. R. Mosig, “Integral-equation analysis of 3-D metallic objects arranged in 2-D lattices using the Ewald transformation,” *IEEE Trans. Microwave Theory Tech.*, vol. 54, no. 10, pp. 3688-3697, Oct. 2006.

[34] X. Dardenne and C. Craeye, “Method of moments simulation of infinitely periodic structures combining metal with connected dielectric objects,” *IEEE Trans. Antennas Propag.*, vol. 56, no. 8, pp. 2372-2380, Aug. 2008.

[35] T. Kushta and K. Yasumoto, “Electromagnetic scattering from periodic arrays of two circular cylinders per unit cell,” *Progress in Electromagnetics Research*, vol. PIER 29, pp. 69-85, 2000.

[36] K. Yasumoto, H. Toyama, and T. Kushta, “Accurate analysis of two-dimensional electromagentic scattering from multilayered periodic arrays of circular cylinders using lattics sums technique,” *IEEE Trans. Antennas Propag.*, vol. 52, no. 10, pp. 2603-2611, Oct. 2004.

[37] N. Kinayman and M. I. Aksun, “Comparative study of acceleration techniques for integrals and-series in electromagnetic problems,” *Radio Sci.*, vol. 30, no. 6, pp. 1713-1722, 1995.

[38] K. E. Jordan, G. R. Richter, and P. Sheng, "An efficient numerical evaluation of the Green's function for the Helmholtz operator on periodic structures problems," *J. Comput. Phys.*, vol. 63, no. 6, pp. 222-235, 1986.

[39] M. J. Park and S. Nam, "Efficient calculation of the Green's function for multilayered planar periodic structures periodic structures," *IEEE Trans. Antennas Propag.*, vol. 46, no. 10, pp. 1582-1583, Oct. 1998.

[40] M. G. Silveirinha and C. A. Fernandes, "A new acceleration technique with exponential convergence rate to evaluate periodic Green functions," *IEEE Trans. Antennas Propag.*, vol. 53, no. 1, pp. 347-355, Jan. 2005.

[41] J. L. Blanchard, E. H. Newman, and M. Peters,"Integral equation analysis of artificial media," *IEEE Trans. Antennas Propag.*, vol. 42, pp. 727-731, May 1994.

[42] D. R. Smith, S. Schultz, P. Marko, and C. M. Soukoulis, "Determination of effective permittivity and permeability of metamaterials from reflection and transmission coefficients," *Phys. Rev. B*, vol. 65, p. 195104, 2002.

[43] M. G. Silveirinha, "Metamaterial homogenization approach with application to the characterization of microstructured composites with negative parameters," *Phys. Rev. B*, vol. 75, p. 115104, 2007.

[44] L. C. Trintinalia and H. Ling, "Integral equation modeling of multilayered doubly-periodic lossy structures using periodic boundary condition and a connection scheme," *IEEE Trans. Antennas Propag.*, vol. 52, no. 9, pp. 2253-2261, Sept. 2004.

[45] M.-K. Li and W. C. Chew, "Multiscale simulation of complex structures using equivalence principle algorithm with high-order field point sampling scheme," *IEEE Trans. Antennas Propag.*, vol. 56, no. 8, pp. 2389-2397, Aug. 2008.

[46] M.-K. Li and W. C. Chew, "Wave-field interaction with complex structures using equivalence principle algorithm," *IEEE Trans. Antennas Propag.*, vol. 55, no. 1, pp. 130-138, Jan. 2007.

[47] S. M. Rao, D. R. Wilton, and A. W. Glission, ”Electromagnetic scattering by surfaces of arbitrary shape,” *IEEE Trans. Antennas Propag.*, vol. 30, no. 3, pp. 409-418, May 1982.

[48] R. F. Harrington, *Time-Harmonic Electromagnetic Fields*, New York: McGraw-Hill, 1961.

[49] R. E. Collin, *Field Theory of Guided Waves*, 2nd ed. New York: Wiley-Interscience, 1991, Ch. 1, pp. 1-54.

[50] E. T. Copson, “An integral equation method for solving plane diffraction problems,” *Proc. Roy. Soc (London). Ser. A*, vol. 186, no. 1, pp. 100-118, 1946.

[51] T. Cwik, “Scattering from general periodic screens,” Ph.D. Dissertation, University of Illinois, Urbana, IL, 1986.

[52] J. M. Song, C. C. Lu, and W. C. Chew, “MLFMA for electromagnetic scattering from large complex objects,” *IEEE Trans. Antennas Propag.*, vol. 45, no. 10, pp. 1488-1493, Oct. 1997.

[53] W. R. Scott, “Error due to spatial discretization and numerical precision in the finite-element method,” *IEEE Trans. Antennas Propag.*, vol. 42, no. 11, pp. 1565-1570, Nov. 1994.

[54] G. S. Warren and W. R. Scott, “Numerical dispersion of higher order nodal elements in the finite-element method,” *IEEE Trans. Antennas Propag.*, vol. 44, no. 3, pp. 317-320, March 1996.

[55] A. Taflove and S. C. Hagness, *Computational Electrodynamics: the Finite-Difference Time-Domain Method*, 3rd ed. Boston: Artech House, 2005.

[56] K. F. Warnick and W. C. Chew, “Error analysis of the moment method,” *IEEE Antennas Propag. Mag.*, vol. 46, no. 6, pp. 38-53, Dec. 2004.

[57] C. P. Davis and K. F. Warnick, “Error analysis of 2-D MoM for MFIE/EFIE/CFIE based on the circuit cylinder,” *IEEE Trans. Antennas Propag.*, vol. 53, no. 1, pp. 321-331, March 1996.

[58] A. F. Peterson and M. M. Bibby, “Error trends in higher-order discretizations of the EFIE and MFIE,” *IEEE APS Int. Symp.*, pp. 52-55, vol. 3A, 2005.

[59] F. G. Bogdanov and R. G. Jobava, “Estimating accuracy of MoM solutions on arbitrary triangulated 3-D geometries based on examination of boundary conditions performance and accurate derivation of scattered fields,” *J. of Electromagn. Waves and Appl.*, vol. 18, no. 7, pp. 879-897, July 2004.

[60] A. F. Peterson, D. R. Wilton, and R. E. Jorgenson, “Variational nature of Galerkin and non-Galerkin moment method solutions,” *IEEE Trans. Antennas Propag.*, vol. 44, no. 4, pp. 500-503, April 1996.

[61] B. M. Kolundzija, “Accurate solution of square scatterer as benchmark for validation of electromagnetic modeling of plate structures,” *IEEE Trans. Antennas Propag.*, vol. 46, no. 7, pp. 1009-1014, July 1998.

[62] R. D. Graglia, D. R.Wilton, and A. F. Peterson, “Higher order interpolatory vector bases for computational electromagnetics,” *IEEE Trans. Antennas Propag.*, vol. 45, no. 3, pp. 329-342, March 1997.

[63] T. K. Sarkar, A.R. Djordjevic, and E. Arvas, “On the choice of expansion and weighting functions in the numerical solution of operator equations,” *IEEE Trans. Antennas Propag.*, vol. 33, no. 9, pp. 988-996, Sept. 1985.

[64] J. C. Nedelec, “Mixed finite elements in R^3,” *Numer. Mathem.*, vol. 35, pp. 315-341, 1980.

[65] M. Yang and J. M. Song, “Error in projection of plane waves using the RWG basis functions,” *IEEE APS Int. Symp.*, pp. 2873- 2876, June 2006.

[66] Fu-Gang Hu, Jiming Song, and Ming Yang, “Error in projection of plane waves using various basis functions,” *IEEE Antennas Propag. Mag.*, Vol. 51, No. 2, pp. 86-98, April 2009.

[67] A. F. Peterson, S. L . Ray, and R. Mittra, *Computational Methods for Electromagnetics*, Oxford : Oxford University Press, 1998.

[68] L. Tsang, J. A. Kong, K.-H. Ding, and C. O. Ao, *Scattering of Electromagnetic Waves. Numerical Simulations*, New York : Wiley, 2001.

[69] S.-C. Lee, M. N. Vouvakis, and J.-F. Lee, “A non-overlapping domain decomposition method with non-matching grids for modeling large finite antenna arrays,” *J. Comput. Phys.*, vol. 203, pp. 1-21, Feb. 2005.

[70] Y.-J. Li and J.-M. Jin, “A new dual-primal domain decomposition approach for finite element simulation of 3-D large-scale electromagnetic problems,” *IEEE Trans. Antennas Propagat.*, vol. 55, no. 10, pp. 2803-2810, Oct. 2007.

[71] B. Stupfel and M. Mognot, “A domain decomposition method for the vector wave equation,” *IEEE Trans. Antennas Propagat.*, vol. 48, no. 5, pp. 653-660, May 2000.

[72] Y. Lu and C. Y. Shen, “A domain decomposition finite-difference method for parallel numerical implementation of time-dependent Maxwell’s equations,” *IEEE Trans. Antennas Propagat.*, vol. 45, no. 3, pp. 556-562, Mar. 1997.

[73] W. C. Chew and C. C. Lu, “The use of Huygens’ equivalence principle for solving the volume integral equation of scattering,” *IEEE Trans. Antennas Propagat.*, vol. 41, no. 7, pp. 897-904, July 1993.

[74] S. Chakraborty and V. Jandhyala, “A surface equivalence-based method to enable rapid design and layout interations of coupled electromagnetic components in integrated packages,” in *Proc. IEEE 13th Topical Meeting on Electrical Performance of Electronic Packaging*, pp. 45-48, Portland, OR, 2004.

[75] T.-M. Wang and H. Ling, “Electromagnetic scattering from three-dimensional cavities via a connection scheme,” *IEEE Trans. Antennas Propagat.*, vol. 39, no. 10, pp. 1505-1513, Oct. 1991.

[76] J. R. Mautz and R. F. Harrington, “H-field, E-field, and combined-field solutions for conducting body of revolution,” *Arch. Elektr. Ubertragung*, vol. 32, pp. 157-164, 1978.

[77] C. A. Balanis, *Advanced Engineering Electromagnetics*. New York: Wiley, 1989, Ch. 12, pp. 670-742.

[78] W. C. Chew, J. M. Jin, E. Michielssen, and J. Song, *Fast and Efficient Algorithm in Computational Electromagnetics*. Boston : Artech House, 2001, Ch. 3, pp. 77-118.

[79] R. D. Graglia,“On the numerical integration of the linear shape functions times the 3-D Green’s function or its gradient on a plane triangle,” *IEEE Trans. Antennas Propag.*, vol. 41, no. 10, pp. 1448-1455, Oct. 1993.

[80] M. G. Duffy,“Quadrature over a pyramind or cube of integrands with a singularity at a vertex,” *SIAM J. Numer. Anal.*, vol. 19, no. 6, pp. 1260-1262, Dec. 1982.

[81] D. R. Wilton, S. M. Rao, A. W. Glission, D. H. Schaubert, O. M. Al-Bundak, and C. M. Bulter,“Potential integrals for uniform and linear source distributions on polygonal and polyhedral domains,” *IEEE Trans. Antennas Propag.*, vol. 32, no. 3, pp. 276-281, Mar. 1984.

[82] J. R. Mosig, ”Integral-eqation technique,” in *Numerical Techniques for Microwave and Millimeter-wave Passive Structures,* T. Itoh, Ed. New York: Wiley, 1989, Ch. 3, pp. 133-213.

[83] Fu-Gang Hu and Jiming Song, “Integral-equation analysis of scattering from doubly periodic array of 3-D conducting objects,” *IEEE Trans. on Antennas Propag.*, revision, Dec. 2009.

[84] F. G. Hu and J. Song, ”Integral Equation Analysis of Scattering from Multilayered Periodic Array Using Equivalence Principle and Connection Scheme,” *IEEE Trans. Antennas Propag.*, vol. 58, no. 3, pp. 848-856, Mar. 2010.

[85] J. M. Jin, *The Finite Element Method in Electromagnetics*, 2nd ed. New York: Wiley, 2002.

VITA

Fu-Gang Hu was born in Jiangxi, P. R. China, in October 1977. He received B. Eng. and M. Eng. degrees from Xidian University, Xi'an, P. R. China, in 1999 and 2002, respectively.

He was an Associate Scientist with Temasek Laboratories, National University of Singapore, Singapore, from 2002 to 2007. Since 2007, he has been a Research Assistant at the Department of Electrical and Computer Engineering at Iowa State University. His current research interests include electromagnetic modeling using numerical techniques. He received the IEEE Antennas and Propagation Society Doctoral Research Award for 2009-2010.

PUBLICATIONS

1. Journal papers[1]

1. **Fu-Gang Hu and Jiming Song, “Integral equation analysis of scattering from multilayered periodic array using equivalence principle and connection scheme,” *IEEE Trans. on Antennas and Propag.*, vol. 58, no. 3, pp. 848-856, Mar. 2010.**
2. **Fu-Gang Hu and Jiming Song, “Integral-equation analysis of scattering from doubly periodic array of 3-D conducting objects”, *IEEE Trans. on Antennas and Propag.*, revision, 2010.**
3. **Fu-Gang Hu, Jiming Song, and Ming Yang, “Error in projection of plane waves using various basis functions,” *IEEE Antennas and Propagation Magazine*, vol. 51, no. 2, pp. 86-98, April 2009.**
4. Fu-Gang Hu and Chao-Fu Wang, “Preconditioned formulation of FE-BI equations with domain decomposition method for calculation of electromagnetic scattering from cavities,” *IEEE Trans. on Antennas and Propag.*, vol. 57, no. 8, pp. 2506-2511, Aug. 2009.
5. Fu-Gang Hu, Chao-Fu Wang, and Yeow Beng Gan, “Efficient calculation of interior scattering from large three-dimensional PEC cavities,” *IEEE Trans. Antennas Propag.*, vol. 55, no. 1, pp. 167-177, Jan. 2007.
6. Fu-Gang Hu, Chao-Fu Wang, Yuan Xu, and Yeow-Beng Gan, “Modal method analysis of multilayered coated circular waveguide using a modified characteristic equation,” *Progress In Electromagnetics Research*, PIER 45, pp. 243-262, 2004.

---

[1] The journal papers related to this thesis are typed in bold.

2. Conference papers (selected)

1. Fu-Gang Hu and Jiming Song, “Relationship of scattering from the PEC screen with infinite periodicity and its complementary structure,” *IEEE APS Int. Symp.*, accepted, 2010.
2. Fu-Gang Hu and Jiming Song, “Special basis and testing functions for integral-equation formulation for doubly periodic array of 3-D objects,” *IEEE APS/URSI Int. Symp.*, accepted, 2010.
3. Fu-Gang Hu and Jiming Song, “Integral equation analysis of 2-D scattering from multilayered periodic array using equivalence principle and connection scheme,” *IEEE APS Int. Symp.*, June 2009.
4. Fu-Gang Hu and Jiming Song, “Error in projection of plane waves using various basis functions,” *IEEE APS Int. Symp.*, July 2008.
5. Fu-Gang Hu and Chao-Fu Wang, “Preconditioner for modeling EM scattering from cavities using FE-BI equations with domain decomposition method,” *IEEE APS Int. Symp.*, July 2008.